

# CONTROLLING AND DETECTING LIGHT FOR ON-CHIP OPTICAL INTERCONNECTS

A Dissertation

Presented to the Faculty of the Graduate School  
of Cornell University

in Partial Fulfillment of the Requirements for the Degree of  
Doctor of Philosophy

by

Long Chen

May 2009

© 2009 Long Chen  
ALL RIGHTS RESERVED

# CONTROLLING AND DETECTING LIGHT FOR ON-CHIP OPTICAL INTERCONNECTS

Long Chen, Ph.D.

Cornell University 2009

The tremendous growth in computer processing power as a result of the microelectronics scaling demands corresponding increase in communications bandwidth that is approaching the limits of traditional electrical interconnects. Optical links, traditionally limited to only long-haul communications, are therefore replacing electrical cables at increasingly small distances, down to only a few tens of centimeters already. In the near future, optical interconnects on the chip level for inter- and intra-chip communications, with length scales of few centimeters to few millimeters, are projected to be imperative. For this goal, silicon photonics has been rapidly emerging for the vision of building integrated photonic circuits on the same chip as the microelectronics for on- and off-chip communications.

This dissertation is part of the on-going effort in developing a fully integrated silicon photonic circuit. It contains works on two parts of such a circuit. The first part is the demonstration of resonators with bandwidth dynamically reconfigurable over a very broad range, targeted for functionalities such as reconfigurable filters and tunable optical delays, etc. The second part is the demonstration of the fastest germanium photodetectors integrated with silicon photonic circuits through a novel process compatible with the microelectronics, and of an integrated WDM detection system that can potentially provide over tera-bit per second bandwidth with a small footprint on chip.

## BIOGRAPHICAL SKETCH

Long Chen was born and raised in a small town near the Yangzi River in central China. He obtained his Bachelor's degree in Electrical Engineering from Zhejiang University in Hangzhou, China in 2003, and then joined Cornell University in Ithaca, NY in 2004 to pursue his graduate study. Under the supervision of Prof. Michal Lipson, he worked on a variety of projects including plasmonics, nanocavities, and integrated silicon photonic circuits including photodetectors, modulators, and wavelength-division multiplexing for on-chip interconnect applications.

This dissertation is dedicated to my parents.

## ACKNOWLEDGEMENTS

The five years of my Ph.D study in Cornell has been a wonderful and enriching experience. Besides the knowledge I gained on the academic side, I came to know many great people without whom I would not be able to complete this dissertation.

I am mostly indebted to my advisor professor Michal Lipson for her guidance and support throughout the years. Her far-reaching vision of the research fields and openness for very different directions are mostly appreciated. I enjoyed the luxurious freedom in exploring several topics interesting to me. Meeting with her has never been worrisome for me even in occasions of experimental frustrations and setbacks. Instead her patience, trust and encouragement are often the best recipe.

I would also like to thank professor Clifford Pollock and Alexander Gaeta for being in my committee and giving me great suggestions on my thesis project. I also thank other great teachers in Cornell, in particular Fahan Rana, Frank Wise, Sandip Tiwari, their insightful lectures were a real pleasure in the classroom. I sincerely wish I had taken more classes during my study in Cornell.

Special thanks goes to the entire Nanophotonics group in Cornell. They are a wonderful group of people as both colleagues and friends to whom I can not be more grateful. My first thanks goes to Dr. Jagat Shakya for leading me into the nano-world and offering me great help in my initial stage of graduate work. More important than any techniques, his persistence is the one thing I have been trying to mimic in and outside of the cleanroom. I have enjoyed working with Nicolas Sherwood-Droz, Bernardo Kyotoku, Kyle Preston, Arthur Nitkowski, Debo Olaosebikan, Dr. Jacob Robinson, Dr. Po Dong and Dr. Jaime Cardenas on various projects. I have also enjoyed discussions with Dr. Gustavo Wieder-

heck on many topics about sciences and beyond: his broad viewpoint and precise logic often bring quite some pleasure. I am also constantly getting help from Alexander (sasha) Gondarenko, Dr. Carl Poitras, Dr. Bradley Schmidt, Sasikanth (sasi) Manipatruni, Dr. Amy Turner, Jacob Levy, Hugo Lira, Lian-Wee Luo, Muhammad Adnan, Lucas Gabrielli, Danilo Spadoti, and Biswajeet Guha. I can not forget the many occasions they cheered me up in one way or another. Despite five years of harsh winter, the escape from Ithaca is not easy at all because of them all.

I would also like to thank the staff members in the Cornell Nanoscale Science and Technology Facility (CNF), particularly Michael Skvarla, Daron Westly, Rob Ilic, Dan Woodie and many others. Their help has been extremely valuable.

Last but not least, I wish to thank my parents for their constant love and support during my graduate study. I wish to dedicate this dissertation to them and make them proud.

## TABLE OF CONTENTS

Biographical Sketch . . . . .	iii
Dedication . . . . .	iv
Acknowledgements . . . . .	v
Table of Contents . . . . .	vii
List of Figures . . . . .	ix
<b>1 INTRODUCTION</b>	<b>1</b>
1.1 Optical interconnects in computer communications . . . . .	1
1.2 Silicon photonics for on-chip interconnects . . . . .	3
1.3 Focus and organization of this dissertation . . . . .	6
<b>2 COMPACT BANDWIDTH RECONFIGURABLE OPTICAL RESONATORS</b>	<b>9</b>
2.1 Basics of resonators and resonance tuning . . . . .	10
2.2 Design of resonators with interferometric couplers . . . . .	15
2.3 Fabrication of the resonator with integrated heaters . . . . .	21
2.4 Measurement and results . . . . .	24
2.5 Discussion . . . . .	31
<b>3 HIGH EFFICIENCY INTEGRATED GERMANIUM DETECTORS FROM LOW TEMPERATURE PROCESSES</b>	<b>34</b>
3.1 Introduction . . . . .	35
3.1.1 Requirements for on-chip photodetectors . . . . .	35
3.1.2 Basics of semiconductor photodetectors . . . . .	37
3.1.3 Progresses and challenges . . . . .	46
3.1.4 GeOI-SOI from smart-cut at low temperature . . . . .	49
3.2 Design of integrated detectors on GeOI-SOI . . . . .	52
3.3 Device fabrication . . . . .	57
3.4 Measurement and results . . . . .	61
3.5 Discussion . . . . .	64
3.5.1 Further reduction in dark current . . . . .	65
3.5.2 Speed and bias . . . . .	67
<b>4 INTEGRATED SILICON WAVELENGTH DIVISION DEMULTIPLEXER WITH 40 GHZ GERMANIUM PHOTODETECTORS</b>	<b>70</b>
4.1 Design, fabrication, and characterizations of the ultrafast detectors	71
4.1.1 Improved detector design for high speed . . . . .	71
4.1.2 Fabrication and DC test . . . . .	74
4.1.3 Characterization of impulse response . . . . .	76
4.1.4 Characterization of 40 Gbps data detection . . . . .	80
4.1.5 Discussion . . . . .	82
4.2 Design and characterizations of integrated WDM detection systems	84

4.2.1	Basics of WDM detection systems . . . . .	84
4.2.2	WDM demultiplexer based on cascaded ring resonators .	86
4.2.3	Fabrication and measurements . . . . .	90
4.2.4	Discussion . . . . .	93

## LIST OF FIGURES

1.1	Schematic of an integrated photonic circuit for optical interconnect.	5
2.1	Schematic of an optical resonator and its optical response. <b>a.</b> Schematic of a generic optical resonator with loss $\alpha$ and couplings to the outside $\kappa, \kappa'$ . <b>b.</b> Optical response of the resonator, characterized by a Lorentz function centered at wavelength $\lambda_r$ and with a bandwidth $\delta\lambda$ .	10
2.2	Tuning the resonance bandwidth with the resonator loss. The bandwidth change is accompanied by the severe deterioration of the extinction ratio.	13
2.3	Tuning the resonance bandwidth with the input and output couplings. The bandwidth can be changed without deterioration of the extinction ratio if both couplings can be tuned simultaneously and coordinately to satisfy the critical coupling condition.	14
2.4	Tuning the optical coupling through physical geometry change in the coupling region. <b>a.</b> Example of evanescent coupling between a waveguide and a ring resonator. <b>b.</b> Exponential dependence of the optical coupling on the separation between the waveguide and the ring resonators as a result of its evanescent nature.	15
2.5	Traditional and the new design of add-drop ring resonators. <b>a.</b> A ring resonator with the traditional straight couplers. <b>b.</b> A ring resonator with new interferometric couplers.	16
2.6	Tuning the effective coupling and resonance bandwidth with the phase difference in the interferometric coupler. <b>a.</b> The effective power coupling as a function of the phase difference. <b>b.</b> The resulted resonance bandwidth as a function of the phase difference when both couplers are tuned simultaneously and coordinately.	19
2.7	Images of the fabricated devices with integrated microheaters to control the resonance bandwidth. <b>a.</b> An optical microscope image showing both the silicon resonator and the nickel heaters on top of the coupling waveguides. <b>b.</b> An SEM image showing the microheaters only. The silicon resonator is buried underneath the planarized surface and invisible under SEM.	22
2.8	Fabrication process of the ring resonator with interferometric couplers and integrated microheaters. <b>a.</b> Electron-beam lithography to define the silicon waveguides and resonators. <b>b.</b> Transferring the pattern from the resist to the silicon device layer using etching. <b>c.</b> Deposition and planarization of the $\text{SiO}_2$ cladding. <b>d.</b> Patterning of the nickel microheaters through lithography, evaporation and lift-off.	24

2.9	Optical response of the resonator with interferometric couplers prior to any thermal tuning. <b>a.</b> The transmission of the through port as a function of wavelength. <b>b.</b> The effective power coupling of the interferometric coupler as a function of wavelength. The oscillation behavior in the effective coupling leads to strong oscillations in the bandwidth and extinction ratio of the resonances. . . . .	26
2.10	Changes of the optical response as one starts tuning only the input interferometric coupler with heater 1. <b>a.</b> A sketch of the effective input coupling as a function of heater power with four characteristic states labeled as (I) to (IV): state (I), initial state prior to any tuning; state (II), state of completely destructive interference and minimum coupling; state (III), state of critical coupling; state (IV), state of completely constructive interference and maximum coupling. <b>b.</b> The transmission spectra corresponding to the four states. The scale bar for state (I), (II) and (IV) is 3 dB, and for state (III) is 6 dB. . . . .	28
2.11	Tuning the optical bandwidth while maintaining a large extinction ratio by adjusting the heater power for both interferometric couplers. Here (a) corresponds to the state without any tuning, and (b-d) are states with different heater power levels as specified in the legend. The horizontal dashed line marks the -3 dB level at which the bandwidth is measured. . . . .	30
3.1	The electronic transitions in semiconductor photodetectors associated with the absorption of photons, including inter-band transitions generating both electrons and holes, and transitions between the band and impurity levels inside the band gap. . . .	38
3.2	Transport of photo-generated carriers in the semiconductor. <b>a.</b> Drift process in the <i>depleted</i> region: the carriers experience directional motion driven by the electrostatic field. <b>b.</b> Diffusion process in the <i>non-depleted</i> region: the carriers experience thermal motions driven by the gradient of carrier concentrations. . .	39
3.3	Simplified equivalent circuit for detector applications. A typical detector can be treated as a combination of a current source $I_s$ , a junction capacitor $C_d$ , and a series resistor $R_s$ . <b>a.</b> Detector terminated with a load resistor ( $R_l$ ). <b>b.</b> Detector terminated with a transimpedance amplifier with a feedback resistor $R_f$ and a stabilizing capacitor $C_f$ . . . . .	44

3.4	Challenges in integrating germanium onto silicon. <b>a.</b> Schematic of epitaxy growth of germanium on silicon. The very large mismatch in lattice constants (4.2%) between germanium and silicon induces dislocation defects. For improved crystalline quality a relatively high temperature process above 700°C is required, which is incompatible with the back-end integration scheme. <b>b.</b> A top-view SEM image of an exemplar poly-crystalline germanium film obtained by room temperature evaporation and subsequent thermal anneal. Though small grains of crystal can be formed, the quality is relatively poor and degrades all aspects of the detector performances. . . . .	47
3.5	Integration of a thin layer of crystalline germanium onto silicon. <b>a.</b> Schematic of the wafer bonding and ion-assisted layer cutting technique. <b>b.</b> Cross-sectional SEM image of GeOI-SOI wafer, with the transferred crystalline germanium film on an insulating layer (SiO <sub>2</sub> ) on a silicon-on-insulator (SOI) substrate. . . . .	51
3.6	Design of integrated germanium photodetector on a silicon waveguide. <b>a.</b> 3D schematics. <b>b.</b> the device cross section. . . . .	53
3.7	Optical and electrical modeling of the integrated germanium detector. <b>a.</b> Optical mode profiles for quasi-TE polarization of the input silicon waveguide and the two modes excited in the photodetector region. <b>b.</b> Distribution of the electrostatic field in the germanium region when an external bias is applied between the two electrodes. The field is intentionally saturated near the corners to reveal the details. . . . .	54
3.8	Energy band graph and carriers collection of the metal-germanium-metal detector under a bias. . . . .	56
3.9	Fabrication process for the integrated Ge detector on silicon waveguides. <b>a-c.</b> Prior processes on the Ge wafer, including SiO <sub>2</sub> deposition, hydrogen implantation, and SiO <sub>2</sub> removal with HF. The red dotted line indicates implantation depth. <b>d-f.</b> Prior processes on the SOI wafer, including patterning of Si waveguides, SiO <sub>2</sub> deposition, and SiO <sub>2</sub> CMP planarization. <b>g-i.</b> Formation of GeOI-SOI, including wafer bonding, layer splitting, and Ge CMP planarization. <b>j-l.</b> Formation of the detectors, including patterning of the Ge layer, SiO <sub>2</sub> deposition, via etch and electrodes deposition. . . . .	58
3.10	Device images during the fabrication processes. <b>a.</b> SEM top view image of the silicon waveguide without cladding. <b>b.</b> SEM top view image of the Ge pad with tapers on top of the silicon waveguide. <b>c.</b> Optical image of the fabricated Ge photodetector after deposition of via electrodes. . . . .	60
3.11	Setup for characterizing the DC response of the integrated germanium detector. . . . .	62

3.12	The dark current and photocurrent response of the detector as a function of bias voltage applied across the planar electrodes. . .	63
3.13	The spectrum of the detector photocurrent as a function of wavelength. . . . .	64
3.14	Origin of the dark current in germanium MSM detectors and approach for reduction. <b>a.</b> Schematic of the Fermi level pinning near the valence band edge due to surface states and the formation of hole injection current a result of thermionic emissions. <b>b.</b> Application of a barrier enhancement layer to create a heterojunction with a large barrier for holes to block the hole injection current. . . . .	66
3.15	Problem of carrier diffusion in un-depleted regions in germanium. <b>a.</b> Regions with low electrostatic field labeled on a top view SEM image of the germanium pattern. The arrows illustrate optical diffraction at the electrode entrance. <b>b.</b> Distribution of electrostatic field in the detector cross-section showing the weak field region underneath the electrodes. . . . .	69
4.1	Comparison of the previous and the new detector design. <b>a-b.</b> Cross-sectional schematic of the old and the new designs. <b>c-d</b> Top view SEM images of the detector interfaces for the old and the new designs. . . . .	73
4.2	Optical and electrical properties of the new detector design. <b>a.</b> Optical energy distribution of the fundamental TE mode in the detector region. <b>b.</b> Distribution of the electrostatic field in the detector with an external bias of 1 V. The color map and cones correspond to the strength and directions of the field, respectively.	74
4.3	Comparison of the bias dependence of the photocurrent in both devices. <b>a.</b> The improved design <b>b.</b> The previous design. . . . .	76
4.4	Measurement setup for characterizing the impulse response of the integrated germanium detector. . . . .	77
4.5	Directly recorded temporal response of the germanium detector to a picosecond optical pulse. . . . .	78
4.6	Frequency response of the detector from fast Fourier transform of its impulse response. . . . .	79
4.7	Setup for generating 40 Gbps NRZ optical signal to characterize the detector response at high data rate. PG - pattern generator; FD - frequency doubler; Mux - time-domain multiplexer; Mod - optical intensity modulator. The right inset shows an eye diagram of the generated 40 Gbps signal measured with a commercial ultrafast detector. . . . .	81
4.8	Detector response to an intensity-modulated NRZ optical signal at 40 Gbps. . . . .	82

4.9	Designs of detectors to completely eliminate any non-depleted regions in germanium. <b>a.</b> A PIN-based detector with heavy doping near the narrow edges of germanium. <b>b.</b> A MSM-based detector with electrodes forming at the sidewalls of germanium. <b>c.</b> The distribution of electrostatic field in germanium for the design shown in <b>b.</b> . . . . .	84
4.10	Schematic of a simplified WDM detection system. . . . .	85
4.11	Schematic of an integrated WDM detection system based on cascaded silicon ring resonators and germanium photodetectors. . .	87
4.12	Illustration of optical crosstalk between neighboring channels in cascaded ring resonators. . . . .	89
4.13	Integrated detection system composed of silicon microring resonator-based wavelength division demultiplexer and the germanium detectors. <b>a.</b> Optical image of the device. <b>b.</b> Zoom-in of one microring resonator. . . . .	91
4.14	DC Spectra of the WDM detection system at the through port and the four drop ports measured with integrated detectors. . . .	92
4.15	Eye diagram of demultiplexed NRZ data at the 4th channel at 15 Gbps. . . . .	92
4.16	Optical vernier effect to expand the free spectral range. <b>a.</b> Schematic of two coupled ring resonators. <b>b.</b> Transmission spectra of the coupled resonators at the through port and drop port. Inset: wide and flat passband of the resonance. . . . .	95

# CHAPTER 1

## INTRODUCTION

### 1.1 Optical interconnects in computer communications

The continuing scaling of transistors in microelectronics has enabled a tremendous growth in computer processing power. For example, over the past decade, the speed of the state-of-the-art supercomputers has increased by almost three orders of magnitude, and now is capable of processing over one peta-flops ( $10^{15}$  floating point operations per second)<sup>†</sup>. Following the current speed of progress, one exa-flops ( $10^{18}$ ) is projected to be reached in 2019. This of course requires a dramatic increase in the communication bandwidth among different units within the supercomputers. Even the speed of individual processors has been rapidly approaching the tera-flops ( $10^{12}$ ) regime<sup>‡</sup> and demands large increases in bandwidth.

However, the traditional interconnects using electrical wires for on- and off-chip communications can not keep pace with such growth, and are becoming the bottle-neck of the system [1, 2]. The major limitations include the bandwidth, the power consumption and the latency in the interconnect system. To overcome these limitations, the alternative approach of using optics to partially replace some of the electrical wires is widely pursued [3–5]. In fact, such replacement has been adopted in some supercomputers on the system level for intra-rack and rack-to-rack communications [6]. Optical interconnects on

---

<sup>†</sup>As of November 2008, the current record is hold by IBM Roadrunner at Los Alamos National Laboratory in New Mexico, USA, with a peak speed of 1.46 peta-flops.

<sup>‡</sup>A Cell processor by IBM, Toshiba and Sony, for example, contains 9 cores and runs at 256 giga-flops ( $10^9$ ).

the board level for module-to-module communications are under development now and might be deployed within a few years [7–9]. In the near future, optical interconnects even on the chip level for inter- and intra-chip communications are projected to be imperative as the chip I/O enters the tera-bit per second (Tbps) regime [10].

The bandwidth in electrical interconnect is mostly limited by the signal attenuation in the electrical wires [1]. The absorption of the metal and the dielectric leakage loss both increase sharply as the signal frequency increases<sup>†</sup> [11, 12]. As a result, multiple repeater stages and complicated equalization circuits are required to maintain acceptable signal integrity, which leads to higher power consumption. Although this problem can be partially alleviated by deploying more signal paths of lower frequencies, however, the number of physical paths available is limited because of the physical real estate<sup>‡</sup> and electromagnetic crosstalks among them.

Interconnects in the optical domain, in contrary, can provide much larger bandwidth without such severe sacrifice of power. As the optical carrier frequency typically used in telecommunication is around 200 tera-hertz (THz) and the optical links often have very broad transparency windows, bandwidth over tens of THz is readily available for signal modulation. The attenuation through the optical links has essentially no dependence on the signal bandwidth it carries. Although the bandwidth of a single optical signal is practically limited to a few tens of giga-hertz (GHz) by the signal conversions between the elec-

---

<sup>†</sup>The absorption of electromagnetic waves in the metal is related to the skin effect, where at high frequencies the electrical current is carried only in a thin layer near the surface of the conductors and thus leads to larger resistive loss. The absorption can be calculated to scale with the square root of the signal frequency. The dielectric leakage loss scales linearly with the signal frequency.

<sup>‡</sup>The number of pins for typical chip I/O is over 3000 already, from the *International Technology Roadmap for Semiconductors (ITRS) 2008* updates.

trical and optical domains (electrooptical modulators and photodetectors), this is already much higher than typical electrical links. Furthermore, the bandwidth of optical interconnects can be greatly expanded by sending multiple signals through the same optical link simultaneously and independently, each at slightly different wavelengths. This is in sharp contrast to the electrical interconnects where severe electromagnetic interference occurs. With such wavelength-division multiplexing (WDM) scheme, the aggregated bandwidth (which equals the bandwidth of each signal times the number of signal channels) as large as a few THz can be achieved. Over 1 Tbps data transmission has been demonstrated with either a single optical fiber or a single silicon waveguide<sup>†</sup> [13, 14]. Such great potential in bandwidth provides strong incentives to using optics instead for the bandwidth-hungry interconnect applications.

## 1.2 Silicon photonics for on-chip interconnects

Inter- and intra-chip optical interconnects require complete planar photonic circuits integrated together with the microelectronics. For this goal silicon photonics is a very promising platform which can not only produce compact, low power, multi-functional photonic circuits but also allow such photonic circuits to be built on the same chip as the microelectronics.

The large contrast in the refractive indices in the silicon platform allows very compact and low power photonic systems. This is an important aspect for massive deployment of such systems for on-chip applications where the real-estate and power consumption are serious concerns. With a index contrast of over

---

<sup>†</sup>In fact the present bandwidth record for a single fiber communication is as high as 24 Tbps reported by researchers in Bell Laboratories [13].

40% (between 3.45 of silicon and 1.46 of SiO<sub>2</sub>), the optical mode can be strongly confined to sub-micrometer dimensions and allows bends as tight as the optical wavelength itself [15]. The typical dimensions of the state-of-the-art silicon photonic components, including modulators, switches, detectors etc., are in the range of a few tens of micrometers [16–19]. This is more than one order of magnitude smaller than the components based on glass (silica on silicon) which is widely used in telecommunication networks [20]. Accompanying the dramatic scaling in size, the power consumption of the silicon photonic devices is also greatly reduced [20, 21].

Silicon photonics uses very similar materials and processes as the silicon microelectronics and has the potential to be integrated on the same chip as the microelectronics. This poses a great advantage compared with interconnect schemes using externally packaged photonic components, and can lead to more compact systems with reduced cost and complexity. The strategy for full integration of both photonic and electronic circuits is under active exploration now. One particularly promising scheme is the 3-dimensional back-end integration scheme, where the photonic layer is stacked on top of the electronic layer after the metalization steps for the transistors [6, 22]. Although this is still far down the road, some preliminary and encouraging progresses have been reported, including demonstration of passive and active photonic devices using deposited silicon materials [23, 24]. On the other hand, integration of active silicon photonic components with accompanying silicon electrical driving circuits have been commercially adopted already [25].

Figure 1.1 shows a schematic of silicon photonics circuits envisioned for on-chip optical interconnects. The basic scheme is as follows: the data carried by

electrical signals<sup>†</sup> are first imprinted onto laser beams at different wavelengths using electrooptical modulators. These optical signals are then allocated to different ports depending on their destinations using switching and routing networks. The signals targeted for the same destination are then multiplexed in the wavelength domain to share the same optical link. On the receiver end, the incoming bundle of optical signals are first demultiplexed by their wavelengths, and then routed to different ports where the signals are converted back to electrical signals using photodetectors.

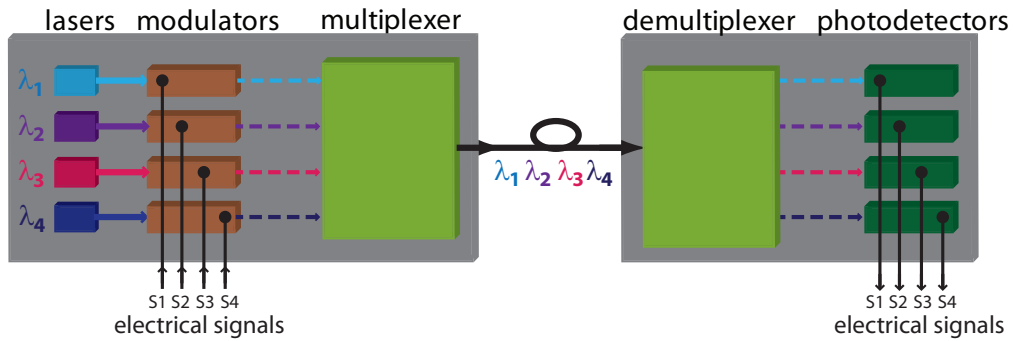


**Figure 1.1.** Schematic of an integrated photonic circuit for optical interconnect.

A great amount of progress has been made in developing components for such photonic circuits over the last a few years. Hybrid lasers incorporating III-V quantum wells onto silicon has been demonstrated already [26]. Alternative gain media such as erbium and germanium are also under active development and many of these work can be found in book [27]. Modulators using either free carrier effect in silicon or electro-absorption effect in silicon-germanium have been achieved with the highest speed of up to 40 Gbps [16, 17, 28–30, 32]. Modulators based on III-V hybrid structures on silicon have also been demonstrated [33]. Photodetectors with various materials such as III-V semiconductor [34],

<sup>†</sup>The data is first time-multiplexed from the data rate of the electrical links (few GHz or less) to the data rate of the optical links (few tens of GHz).

germanium [19, 35, 36], silicide [37], or self-implanted silicon [38, 39] have been reported as well. Switching and routing network with different configurations have also been demonstrated [18, 21, 40–42]. Other progresses include the realization of optical buffer and delay [43, 44], and polarization diversity [45], and the reduction of waveguide loss [46–48] etc.

### **1.3 Focus and organization of this dissertation**

This dissertation is part of the on-going effort in developing a fully integrated silicon photonic circuit that can be applied to the interconnect applications as envisioned in Figure 1.1. As titled as “Controlling and detecting light for on-chip optical interconnects”, it contains work on two parts of such a circuit.

The first part of this dissertation is related to the general aspect of optical resonators that are the basis of a great variety of devices such as modulators, filters, switches, routers and optical delays, etc. The problem this work solves is to dynamically tune the optical bandwidth of the resonators over a broad range using simple mechanisms. This not only allows a versatile photonic circuit reconfigurable to accommodate different signal bandwidths, but also enables functionalities such as tunable optical delays and dispersion compensations.

The second part of this dissertation is on integrated photodetectors. The contribution this work presents is the development of high performance germanium detectors integrated with silicon photonic circuits from a unique low-temperature process compatible with the CMOS back-end integration scheme. We demonstrate germanium detectors with very high efficiency, low dark current, ultra-small capacitance, and a directly measured response time of only

8.8 pico-second, the fastest germanium detector to the best of our knowledge. With these detectors we also demonstrate a highly scalable integrated WDM detection system that can potentially provide over Tbps bandwidth with a small footprint on chip.

These works are discussed in the next three chapters organized as follows.

Chapter 2 covers the work on bandwidth-tunable resonators [49]. Using interferometric couplers and thermo-optical effect, we demonstrate a wide bandwidth tuning range from 0.1 nm to 0.7 nm with  $> 23$  dB extinction ratio and  $< 0.001$  mm<sup>2</sup> footprint. In this chapter we first discuss the motivation and challenge of tuning the resonance bandwidth, and the design of resonators with interferometric couplers to enable such tuning. We then present the analysis, fabrication, and testing of these resonators. At the end we discuss the potential of further expanding the tuning range to from 0.01 nm to a few nanometers.

Chapter 3 covers the first half of the work on high performance germanium detector integrated onto silicon developed with low temperature processes [36]. Using wafer bonding and ion-assisted layer cutting technique, we demonstrate integrated detectors with over 90% quantum efficiency, very low dark current  $\sim 100$  nA, and ultra-small capacitance  $\sim 2$  fF. In this chapter we first discuss the requirements, progresses and challenges of developing integrated detectors for interconnect applications, and the smart-cut integration scheme we use to overcome these challenges. We then present the design, fabrication, and testing of the detectors with this scheme. At the end we also discuss the problems and further improvement in device performances such as speed, bias requirement, and dark current.

Chapter 4 covers the second half of the work on germanium detectors, including the demonstration of ultra-fast operation and their integration with WDM demultiplexers [50]. In the first section we present the improved detector design to resolve the problems observed in the previous design in Chapter 3 and also the revised fabrication techniques to allow monolithic processing. With these new detectors, we present measurements of very short response time (8.8 pico-second) and 40 Gbps operation. At the end we also discuss approaches for even faster germanium detectors. In the second section, we present the basics of WDM detection system and the design of cascaded ring resonators integrated with our fast germanium detectors, and demonstrate experimentally a four-channel high speed WDM detection system. At the end we also analyze their capability for further scaling to provide Tbps bandwidth over a small area on chip.

## CHAPTER 2

### COMPACT BANDWIDTH RECONFIGURABLE OPTICAL RESONATORS

Photonic networks often require the use of optical resonators to control light, including generating, sensing, detecting, filtering, modulating, switching, delaying, dispersion compensation etc. [16, 43, 51–57]. One of the key requirements in such processes is the ability to tune the optical responses of the resonators, including both the wavelength and the bandwidth of their resonances. Tuning the resonance wavelength is a relatively easy task and can be accomplished by changing the refractive index of the resonators with the assist of various mechanisms such thermo-optical, electro-optical and all-optical effects [16, 21, 58]. Tuning the resonant bandwidth, however, is much more challenging and is achieved only with rather complicated systems [59].

In this chapter we demonstrate a novel resonator design in which the bandwidth can be tuned by the same simple approaches of tuning the resonance wavelength, i.e., changing the refractive index of the resonator. Using interferometric couplers and thermo-optical effect, we demonstrate a wide bandwidth tuning range from 0.1 nm to 0.7 nm, while maintaining an extinction ratio higher than 23 dB. With improved design and fabrication, an even larger tuning range from 0.01 nm to a few nanometers can be in principle achieved. With a footprint of less than  $0.001 \text{ mm}^2$ , this device is highly suitable for reconfigurable filtering and routing and tunable optical delay and dispersion compensation for on-chip optical interconnects.

## 2.1 Basics of resonators and resonance tuning

Optical resonators confine light both spatially and temporally. Consider a generic optical resonator as illustrated with the box in Figure 2.1.a. Such a box can be of various geometries, such as spheres, disks, microtoroid, rings, Fabry-Perot plates and photonic crystal cavities etc. [60–64]. Light is confined in the box by mechanisms such as index guiding and reflection. For any real system, it must experience some amount of loss (labeled  $\alpha$ ) that is associated with optical scattering and absorption within the box. To interact with the outside environment, it must also have coupling paths to the outside as input and/or output (labeled  $\kappa$  and  $\kappa'$ ). As a result of the *wave* nature of the light, the spatial confinement creates interference of the optical field inside the box that depends on the optical wavelength, which leads to resonances in the optical response of the box.

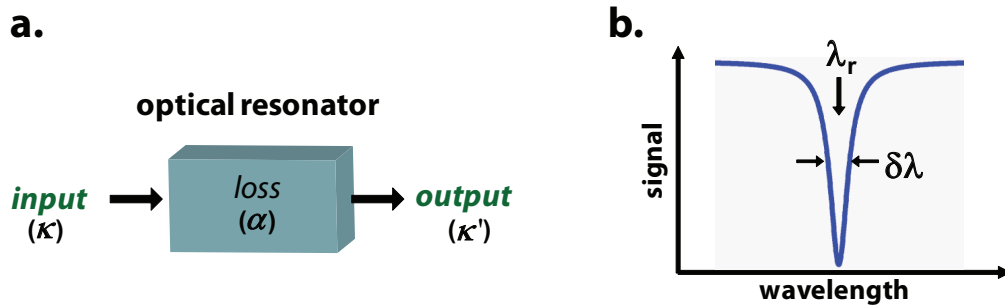


**Figure 2.1.** Schematic of an optical resonator and its optical response. **a.** Schematic of a generic optical resonator with loss  $\alpha$  and couplings to the outside  $\kappa, \kappa'$ . **b.** Optical response of the resonator, characterized by a Lorentz function centered at wavelength  $\lambda_r$ , and with a bandwidth  $\delta\lambda$ .

The optical resonance in the wavelength (or frequency) domain, as illus-

trated in Figure 2.1.b, can be usually described with a Lorentz-shaped function<sup>†</sup>:

$$f(\lambda) \propto 1 - \frac{1}{1 + \left(\frac{\lambda - \lambda_r}{\delta\lambda/2}\right)^2} \quad (2.1)$$

where  $\lambda_r$  is the resonance wavelength, and  $\delta\lambda$  is the resonance bandwidth (the full width at half maximum, FWHM).

Tuning the resonance wavelength is the basis for resonator-based modulators and switches etc. The resonance wavelength ( $\lambda_r$ ) is related to the optical phase accumulation through propagation in the resonator. It usually depends on the physical dimensions of the resonator ( $L$ ) and the refractive index of the medium inside ( $n$ ), and can be generally written as

$$\lambda_r = \frac{n \cdot L}{m}, \quad (2.2)$$

where  $m$  is an integer for the order of the resonance. To tune this resonance wavelength, one can change either the index ( $n$ ) of the optical wave in the resonator or the physical length of the resonator ( $L$ ). The latter is commonly used in Fabry-Perot resonators by moving one of the two mirrors, and also in thin film filters by tilting the filter relative to the optical beam. For integrated photonics, it is also relatively simple to change the refractive index. Resonance wavelength tuning with either thermo-optical effect, electro-optical effect or all-optical effect have been demonstrated on silicon [16, 21, 58]. For the electro-optical modulator application for example, a PIN diode is incorporated with the silicon waveguide forming a ring resonator to inject and extract free carriers (electrons and holes) which modifies the refractive index of the silicon. This shifts the resonance wavelength relative to the optical input wavelength and thus modulates

---

<sup>†</sup>Depending on the cavity geometry and the quantity (transmission, reflection, or field enhancement inside the resonator etc.) one is measuring, the response can be written in different but related forms where the important parameters such as the resonance wavelength and bandwidth remain the same.

the transmission, which effectively converts the signal from the electrical domain to the optical domain.

Tuning the resonant bandwidth, however, has been a much more challenging task. Instead of the phase accumulation, the bandwidth is related to the optical decay rate and therefore difficult to change. Consider the resonator sketched in Figure 2.1.a. The decay rate of the optical energy stored in the resonator is the sum of the power loss ( $\alpha$ ) inside the resonator and its coupling to the outside environment ( $\kappa$  and  $\kappa'$ ). Similar to the case of a damped oscillator, the linewidth of the resonance ( $\delta\lambda$ ) scales proportional to the decay rate as

$$\delta\lambda \propto \alpha + \kappa + \kappa'. \quad (2.3)$$

If somehow one can change the loss inside the resonator ( $\alpha$ ), then the bandwidth can be changed. In fact, this can be achieved in silicon through the free carrier absorption effect by injecting or extracting carriers<sup>†</sup>. However, tuning the bandwidth with loss degrades another important aspect of resonances, i.e., the resonance extinction ratio ( $ER$ ), which measures the inverse of minimum signal level at the resonant wavelength compared to off-resonance signals. The extinction ratio depends on the quantitative relation of the internal loss and the external input / output coupling, and can be written as

$$ER \propto \frac{\kappa + \kappa' + \alpha}{|\kappa - \kappa' - \alpha|}, \quad (2.4)$$

i.e., the ratio of the *total* decay rate (the numerator) to the *net* feeding into the resonator (the denominator). The situation of zero net feeding where

$$\kappa = \kappa' + \alpha, \quad (2.5)$$

---

<sup>†</sup>The free carriers change both the real and imaginary part of the refractive index of silicon. The real part is related to the phase change and it is used in tuning the resonance wavelength. The accompanying imaginary part corresponds to the optical absorption of the free carrier. See page 20 for more details.

is then called "critical coupling condition", where the amount of the input equals the sum of the output and resonator loss, and maximal extinction ratio is achieved [65]. The more the coupling/loss relation deviates away from this critical level, the lower the extinction ratio. To illustrate this problem graphically, Figure 2.2 shows the change in the optical resonance as one gradually increases the loss starting from the critical coupled case. One can see that although the resonance bandwidth – indicated by the arrows – increases as the loss term increases, the extinction ratio degrades rapidly as well. Such serious degradation renders such tuning scheme impractical for most applications.

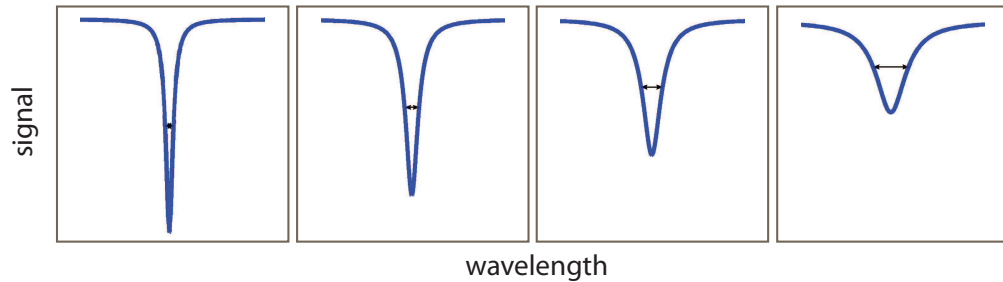


**Figure 2.2.** Tuning the resonance bandwidth with the resonator loss. The bandwidth change is accompanied by the severe deterioration of the extinction ratio.

As evident from Eqn. 2.3 and 2.5, if one can somehow change the two coupling coefficients ( $\kappa$  and  $\kappa'$ ) simultaneously and coordinately in such a way that the critical coupling condition remains valid, then one can change the bandwidth and at the same time maintain a large extinction ratio. Figure 2.3 shows the result of such tuning. The extinction ratio does not degrade as the bandwidth increases, which is in sharp contrast with the case of tuning the loss as shown in Figure 2.2.

To change the coupling, the most intuitive approach is to change the physical geometry in the coupling region. In integrated photonics the optical coupling

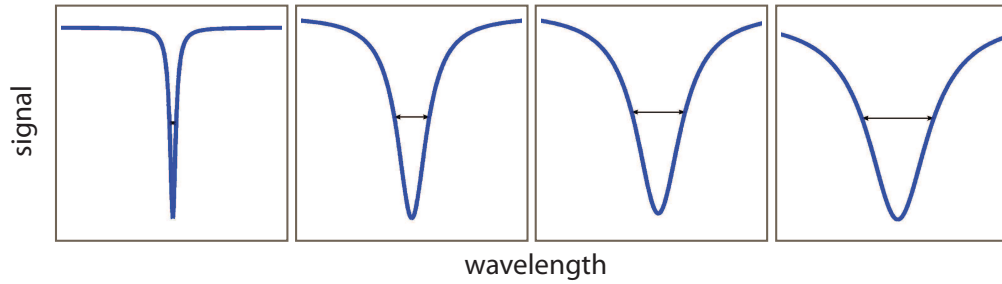


**Figure 2.3.** Tuning the resonance bandwidth with the input and output couplings. The bandwidth can be changed without deterioration of the extinction ratio if both couplings can be tuned simultaneously and coordinately to satisfy the critical coupling condition.

usually relies on evanescent coupling between the mode in a waveguide and the mode in the resonator. Figure 2.4.a shows such an example with a typical ring resonator. As a result of its evanescent nature, the amount of optical coupling depends exponentially on the separation between the waveguide and the resonator, as depicted in Figure 2.4.b. Therefore, if one can physically move the waveguide closer or further relative to the resonator, the amount of coupling can be changed, and so can the bandwidth. This indeed has been demonstrated by J. Yao et al. using MEMS tunable couplers, where two coupling waveguides suspended above a disk resonator are pulled to or pushed away from the disk using electrostatic forces [66]. Despite being a delicate and successful design, the use of double-layered silicon and suspended structure is not very robust and easily integratable with a general purpose photonic circuit.

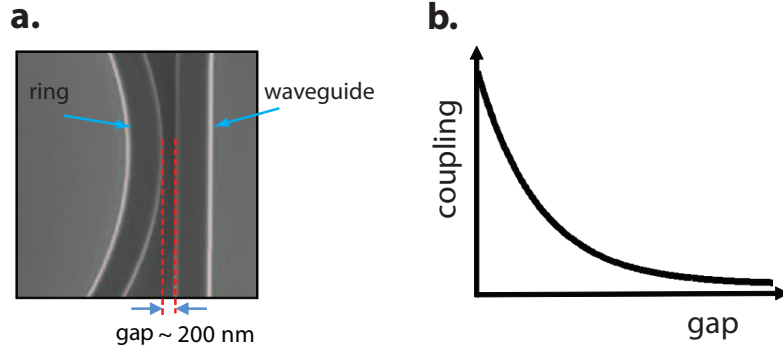


**Figure 2.4.** Tuning the optical coupling through physical geometry change in the coupling region. **a.** Example of evanescent coupling between a waveguide and a ring resonator. **b.** Exponential dependence of the optical coupling on the separation between the waveguide and the ring resonators as a result of its evanescent nature.

## 2.2 Design of resonators with interferometric couplers

An alternative approach of tuning the optical coupling is to use interferometric couplers, with which one can translate the requirement in the power change to the requirement in the phase change [65, 67, 68]. The later, as we pointed out earlier, can be readily achieved using one of several mechanisms. Here as an example we design a ring resonator with interferometric couplers to demonstrate the tuning of the resonance bandwidth with phase change. Figure 2.5.a shows a traditional add drop ring resonator widely used for optical switching applications. The optical response of such a resonator can be rigorously analyzed with coupled mode theory and the readers can consult the appendix A and references therein. Here we directly write down some of the results without derivation. The resonance bandwidth of such a resonator can be written as

$$\delta\lambda = \frac{\lambda_r^2}{4\pi^2 n_g R} \ln[1/G], \quad (2.6)$$

where  $n_g$  is the group index,  $G$  is the decay factor of the optical power circulating inside the resonator after each round-trip, and can be written as  $G \approx (1 - \alpha) \cdot (1 - \kappa) \cdot (1 - \kappa')$ . For resonators with relatively narrow bandwidth, the coefficients  $\alpha, \kappa, \kappa' \ll 1$ , and the decay factor can be approximated to the first order as  $G \approx 1 - (\alpha + \kappa + \kappa')$ . Accordingly the bandwidth can be written as

$$\delta\lambda \approx \frac{\lambda_r^2}{4\pi^2 n_g R} (\alpha + \kappa + \kappa') . \quad (2.7)$$

This agrees with the simplified result shown in Eqn. 2.3. The implication of this result can be understood more intuitively from

$$\frac{1}{Q} \equiv \left( \frac{\delta\lambda}{\lambda_r} \right) = \frac{1}{2\pi} \left( \frac{T}{\tau} \right) (\alpha + \kappa + \kappa') , \quad (2.8)$$

where  $Q$  is the quality factor,  $T$  is the period of the optical oscillation,  $\tau = \frac{2\pi R n_g}{c}$  is the time per round-trip propagation inside the ring with  $c$  being the speed of light. Therefore, the term  $\left( \frac{T}{\tau} \right) (\alpha + \kappa + \kappa')$  in the right hand of Eqn. 2.8 can be interpreted as the amount of energy loss per cycle of optical oscillation. Equation .2.8 is thus agreeing with the explicit definition of the quality factor  $Q$ .

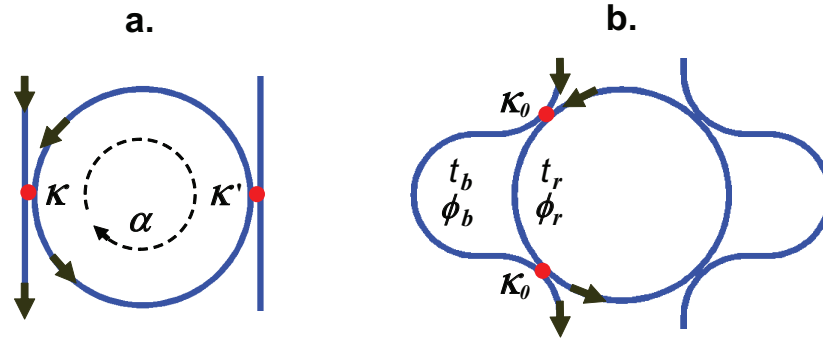


**Figure 2.5.** Traditional and the new design of add-drop ring resonators. **a.** A ring resonator with the traditional straight couplers. **b.** A ring resonator with new interferometric couplers.

Now we reform the two coupling waveguides into interferometric couplers and achieve tuning of the power coupling coefficients through tuning of the

phase. The schematic of the new design is shown in Figure 2.5.b. The two coupling waveguides are curved in such a way that each waveguide couples to the resonator twice. This effectively forms two Mach-Zehnder interferometers, with one set of arms being the coupling waveguides and the other set of arms being part of the ring resonator. Assume that the power coupling at each point is  $\kappa_0$ , and that the transmission and phase accumulation of the bus arm and ring arm are  $t_b, t_r$  (both very close to 1) and  $\phi_b, \phi_r$ , respectively. The effective power coupling coefficient from the input waveguide to the resonator (from port 1 to port 4) therefore is the sum of two terms: one term for the light that stays at the bus arm after the first coupling and cross to the ring at the second coupling (field written as  $\sqrt{1 - \kappa_0} \cdot \sqrt{t_b} e^{i\phi_b} \cdot (-i\sqrt{\kappa_0})$ ), and the other term for the light that goes cross to ring arm after the first coupling and stays at ring arm after the second coupling (field written as  $(-i\sqrt{\kappa_0}) \cdot \sqrt{t_r} e^{i\phi_r} \cdot (-\sqrt{1 - \kappa_0})$ ). The total power coupling then can be simply written as<sup>†</sup>

$$\kappa = \kappa_0 \cdot (1 - \kappa_0) \cdot [t_b + t_r - 2\sqrt{t_b t_r} \cos(\phi_b - \phi_r)]. \quad (2.9)$$

Therefore, the effective power coupling is a strong function of the phase difference between the two coupling arms ( $\Delta\phi = \phi_b - \phi_r$ ). As we change the relative phase difference from 0 to  $\pi$ , the effective coupling changes over a large range from the minimum of  $\kappa_0 \cdot (1 - \kappa_0) \cdot (\sqrt{t_b} - \sqrt{t_r})^2$  to the maximum of  $\kappa_0 \cdot (1 - \kappa_0) \cdot (\sqrt{t_b} + \sqrt{t_r})^2$ . Recalling  $t_b, t_r \approx 1$ , and  $\kappa_0 \ll 1$ , we can simplify this range to from 0 and  $\sim 4\kappa_0$ . This result is plotted in Figure 2.6.a.

The bandwidth tuning can be achieved by tuning both the input and output couplers to satisfy the critical coupling condition. Therefore, the minimum bandwidth is achieved when the output coupling is tuned to 0, and the input

---

<sup>†</sup>Since both terms experience one cross coupling each, any phase change occurring in the cross coupling term (associated with  $\kappa$ ) can be neglected as only the phase difference between the two terms matters.

coupling is tuned to match the resonator loss (with  $\kappa = \alpha, \kappa' = 0$ ). The maximum bandwidth is achieved when the input coupling is tuned to its maximum and the output coupling is tuned to match the input coupling and loss ( $\kappa \sim 4\kappa_0$  and  $\kappa' = \kappa - \alpha$ ). Within this range the bandwidth can be tune continuously. To see how large a tuning range we can practically achieve, we plot in Figure 2.6.b the bandwidth as a function of the phase difference in a semi-log scale for different coupling level  $\kappa_0$ . Parameters typical for silicon resonators are used here:  $\lambda_r = 1.55 \text{ } \mu\text{m}$ ,  $n_g = 4.2$ ,  $R = 10 \text{ } \mu\text{m}$ , and an attenuation constant of 2.5 dB/cm (this corresponds to  $\alpha = 0.004$ ,  $t_b = 0.998$ ,  $t_r = 0.999$ ). One can see that the bandwidth increases continuously with the phase difference, and a very large range from 0.01 nm to a few nanometers can be achieved with strong individual coupling between the waveguides and ring resonator.

To experimentally demonstrate this novel scheme of bandwidth tuning, we design the resonators on silicon-on-insulator (SOI) platform. The silicon waveguide and ring are 520 nm wide, with bending radii of 5.78  $\mu\text{m}$  and 10  $\mu\text{m}$  respectively. These waveguide dimensions are slightly multimode at 1550 nm, with the effective indices for the fundamental and higher order quasi-TE (transverse electric) modes being 2.55 and 1.57, respectively. However only the fundamental mode is excited. The gap between the waveguide and ring is 50 nm to achieve strong coupling for the tightly confined mode. The power coupling at each coupling region ( $\kappa_0$ ) is calculated to be 5.3% at 1550 nm <sup>†</sup>. This corre-

---

<sup>†</sup>The power coupling is calculated with coupled mode theory as follows. First we calculate the effective indices of the symmetrical and asymmetrical modes of two straight waveguides as a function of their separation. The splitting of the effective indices originates from the optical overlap between their independent modes of the two waveguides and thus is proportional to the mode coupling. Next, an integral is performed to calculate the accumulated coupling between the curved waveguide arm and the ring, taking into account that their separation varies throughout the coupling region. Note that since the optical mode is so tightly confined in the silicon waveguide, we do not take into account the change in the mode profile as an effect of bending for the bending radius used here.

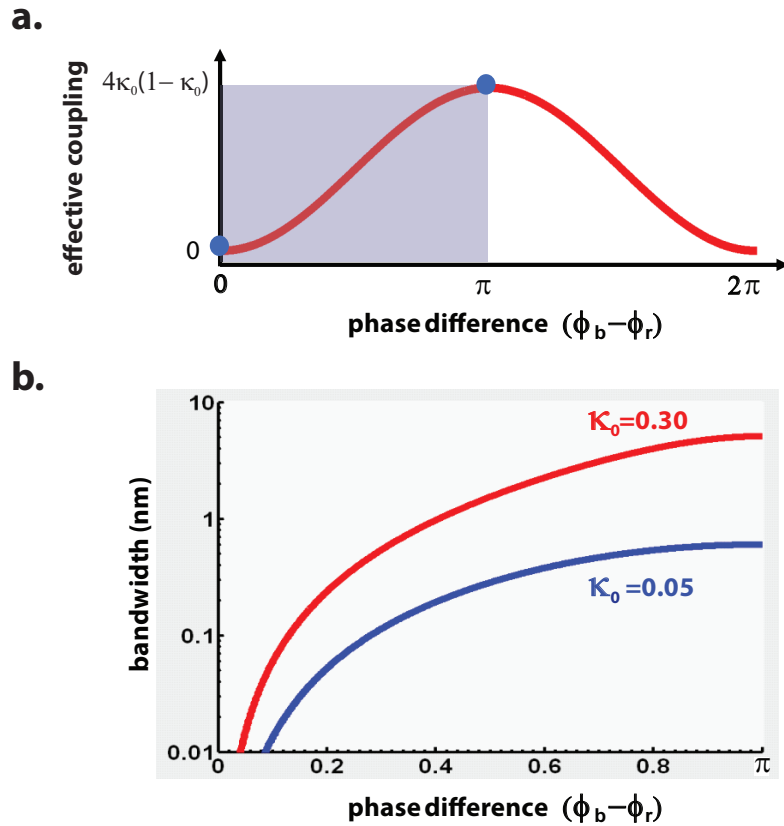


**Figure 2.6.** Tuning the effective coupling and resonance bandwidth with the phase difference in the interferometric coupler. **a.** The effective power coupling as a function of the phase difference. **b.** The resulted resonance bandwidth as a function of the phase difference when both couplers are tuned simultaneously and coordinately.

sponds to a maximal bandwidth  $\delta\lambda$  of approximately 0.65 nm based on Eqn. 2.7. The whole device has a foot print of only  $0.001 \text{ mm}^2$ , which is five orders of magnitude smaller than a previous device on silica-on-silicon with similar functionality, and thus allows dense integration for on-chip applications.

We choose to use the thermo-optical tuning with integrated microheaters to induce the index change and bandwidth tuning. While other tuning mechanism such as free carrier effect of silicon through electrical injection or optical absorp-

tion can be used with faster response, the thermo-optical effect is preferred due to its simplicity and the strong thermo-optical effect of silicon that leads to large obtainable index change. At the wavelength of 1550 nm and room temperature the thermo-optical coefficient is known to be approximately [69]

$$\frac{\Delta n}{\Delta T} = 1.84 \times 10^{-4}. \quad (2.10)$$

Therefore, one can obtain a change in the refractive index as large as 0.03 with about 150°C change in local temperature which is achievable with integrated microheaters. This corresponds to a length of approximately 25  $\mu\text{m}$  only for a  $\pi$  phase shift, allowing very compact devices. The response time of the thermo-optical devices depends on thermal diffusion and is typically in the few microsecond to sub-microsecond regime. Such speed is sufficient for most network applications where only non-frequent bandwidth reconfiguration of the photonic circuits is required. Alternatively, changing the index through free carrier effect can be much faster, in the nanosecond regime or better. However, the drawback is that the excessive carriers not only lead to a change in the real part of the refractive index but also induce a change in the imaginary part as a result of free carrier absorption. The changes in the real part of the refractive index ( $\Delta n$ ) and the absorption coefficient ( $\Delta\alpha$ , in  $\text{cm}^{-1}$ ) can be written as [70, 71]

$$\Delta n = -8.8 \times 10^{-22} \Delta N - 8.5 \times 10^{-18} (\Delta P)^{0.8}, \quad (2.11a)$$

$$\Delta\alpha = 8.5 \times 10^{-18} \Delta N + 6.0 \times 10^{-18} \Delta P, \quad (2.11b)$$

respectively, where  $\Delta N$  and  $\Delta P$  are the concentrations of the excessive free electrons and holes, in  $\text{cm}^{-3}$ . For excessive carrier concentrations of  $10^{19} \text{ cm}^{-3}$  for both electrons and holes, for example, the induced index change is 0.022, requiring a slightly larger length for  $\pi$  phase shift. The additional free carrier absorption, however, is as large as  $145 \text{ cm}^{-1}$  or 630 dB/cm, which corresponds

to an attenuation of more than 2 dB accompanying the  $\pi$  phase shift. The attenuation can be slightly reduced with lower injection level and longer device. However, even for a injection level as low as  $10^{16} \text{ cm}^{-3}$ , the extra attenuation is still around 0.8 dB for a  $\pi$  phase shift (with a required length of more than one centimeter). This severely limits the applications where large phase tuning is desired without significant extra attenuation.

One concern for using the thermo-optical effect in integrated photonic networks is the thermal diffusion and cross-talk between neighboring devices. We analyze the thermal property of our device with FEMLAB simulations. Since the microheaters can be integrated directly above the silicon waveguide with a thin  $\text{SiO}_2$  intermediate layer and provide very localized thermal energy, the temperature of the silicon waveguide can be changed very efficiently without significant diffusion of the heat. Even for a local temperature change of up to  $100^\circ\text{C}$  in the silicon waveguide, the surrounding temperature drops to room temperature about  $15 \mu\text{m}$  away from the heating source. This allows for massive integration of such devices on-chip free of thermal cross-talk. Even better thermal isolation can be achieved by etching deep trenches between the devices to reduce in-plane heat diffusion through  $\text{SiO}_2$  and the underneath silicon substrate.

### **2.3 Fabrication of the resonator with integrated heaters**

We fabricate the silicon ring resonator with integrated nickel microheaters. Figure 2.7.a shows an optical image of the fabricated device, showing both the silicon resonator and the nickel heaters on top of the coupling waveguides to in-

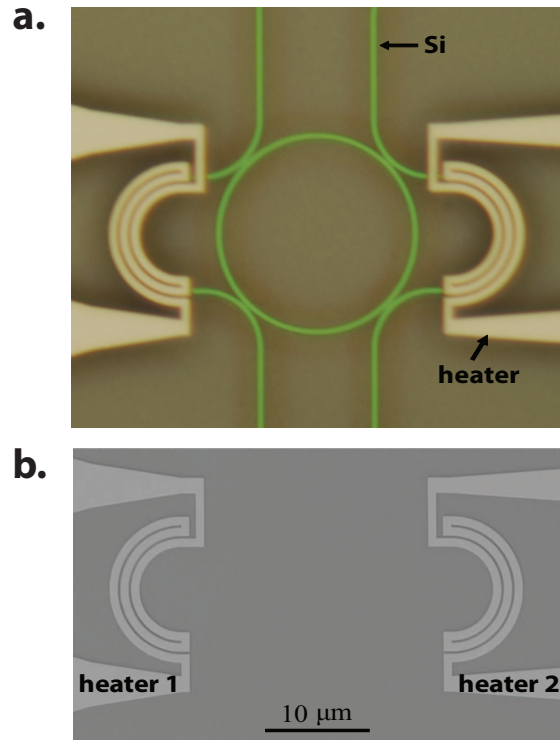


**Figure 2.7.** Images of the fabricated devices with integrated microheaters to control the resonance bandwidth. **a.** An optical microscope image showing both the silicon resonator and the nickel heaters on top of the coupling waveguides. **b.** An SEM image showing the microheaters only. The silicon resonator is buried underneath the planarized surface and invisible under SEM.

duce the thermo-optical tuning. Figure 2.7.b shows an SEM image of the heaters, where the silicon resonator is buried underneath the planarized  $\text{SiO}_2$  surface and invisible under SEM. The fabrication process of the device is sketched in Figure 2.8. We start with a 4-inch SOI wafer with  $3 \mu\text{m}$  of buried oxide and  $240 \text{ nm}$  of top silicon. After spin-coating the wafer with negative-tone electron-beam resist (hydrogen silsesquioxane, HSQ), we expose the pattern of the waveguides and rings with electron-beam lithography. After develop in MIF 300, the pattern is transferred to the silicon device layer using an inductively coupled plasma reactive ion etching tool with  $\text{Cl}_2$  based chemistry. The

wafer is then cladded with SiO<sub>2</sub> via plasma-enhanced chemical vapor deposition. To allow subsequent patterning of localized heaters on top of the coupling waveguides, and uniform gap between the waveguide and the heaters, the wafer is then planarized with chemical mechanical polishing to obtain smooth surface topology. The final thickness of the SiO<sub>2</sub> film is approximately 1 μm. This thickness is chosen to ensure that the metal heater is in close proximity to the silicon waveguide for efficient tuning of its temperature, and at the same time the optical mode of the waveguide has no overlap with the metal on top to avoid any additional scattering/absorption loss. After this step, another aligned electron-beam lithograph step is performed to define the localized microheaters in positive-tone resist (double-layered PMMA for a undercut profile), followed by evaporation and lift-off of the heater metals, which consist of 5 nm titanium as an adhesion layer and 100 nm nickel. The microheaters are folded several times to increase the resistance. Finally, photolithography, evaporation of 5 nm titanium and 150 nm gold, and lift-off are performed to define the electrical wires and contact pads connected to the microheaters. The total resistance of each heater is measured to be approximately 160 Ω at room temperature<sup>†</sup>. The sample are then diced and the facets are polished mechanically for optical testing.

---

<sup>†</sup>The resistivity of nickel is quite sensitive to temperature and is widely used in thermometers [72]. Therefore, the heater resistance increases as the supply voltage or current increases, which in fact can be used to estimate the temperature change of the nickel heater with a given amount electrical power.

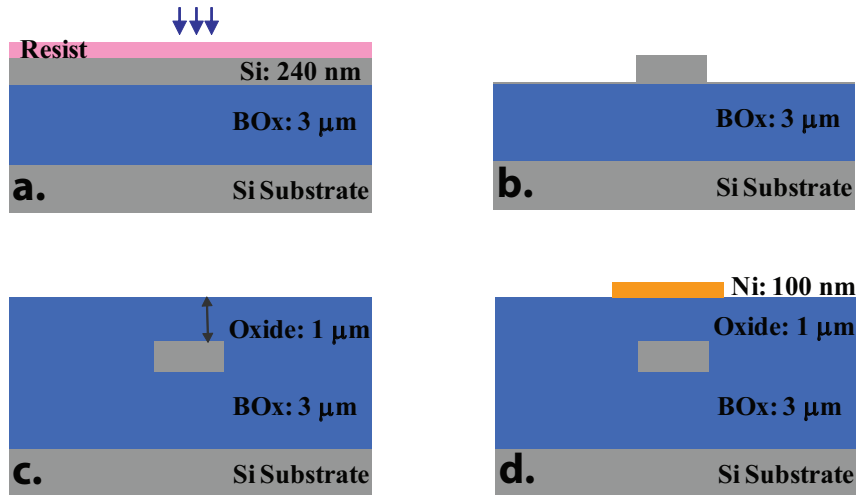


**Figure 2.8.** Fabrication process of the ring resonator with interferometric couplers and integrated microheaters. **a.** Electron-beam lithography to define the silicon waveguides and resonators. **b.** Transferring the pattern from the resist to the silicon device layer using etching. **c.** Deposition and planarization of the SiO<sub>2</sub> cladding. **d.** Patterning of the nickel microheaters through lithography, evaporation and lift-off.

## 2.4 Measurement and results

The optical response of the device is measured as follows. Light from a wavelength-tunable continuous wave laser is coupled to an optical fiber and a fiber polarization controller to obtain TE polarization. The polarized signal is then launched into the silicon waveguide, with a tapered lens tip at the end of the fiber and a nanotaper [73] at the input facet of the silicon waveguide to maximize the coupling efficiency. The transmission through the device is then coupled to free space with another nanotaper at the output facet of the waveguide. The signal is then collected with an objective lens and recorded with a photodetector. To apply thermal tuning, the two microheaters are each con-

nected to an electrical power supply through a double-tipped (ground-signal) electrical probe. The amount of electrical power supplied to each heater is individually tuned with the voltage to obtain desirable optical response.

We first measure the optical response without application of any thermo-optical tuning. Figure 2.9.a shows the through-port transmission of the device normalized to a reference waveguide. Relatively strong Fabry-Perot oscillations for off-resonance wavelengths are observed, and are most probably attributed to reflections at stitching defects induced in the lithography step. Multiple ring resonances are observed with a free spectral range (FSR) of  $\sim 9$  nm. A distinctive feature in this spectrum is that unlike that of typical ring resonators, the resonances exhibit very different bandwidths and extinction ratios (or minimum transmission level at resonance wavelengths). An inspection of the spectrum over a larger spectral range reveals that both the bandwidths and extinction ratios are oscillating with the wavelength. These oscillations originate from the interferometric couplers we use, where the effective power coupling is dependent on the wavelength, an inherent nature of interferometers. This can be better understood if we explicitly write the phase difference in Eqn.2.9 as  $\Delta\phi(\lambda) = 2\pi n_e(\lambda)(L_b - L_r)/\lambda$ , where  $n_e(\lambda)$  is the effective index of the waveguide mode, and  $L_b$  and  $L_r$  are the physical lengths of the two interfering arms. Combining this with Eqn.2.9, and taking  $L_b - L_r = 15.68$   $\mu\text{m}$  for this device, we sketch the effective coupling  $\kappa$  as a function of  $\lambda$  in Figure 2.9.b. This apparently exhibits an oscillating behavior correlated with the oscillations observed in the resonance bandwidth and extinction ratio shown in Figure 2.9.a. Note that the input and output couplers have the same design, without any tuning they have the same effective coupling coefficient ( $\kappa = \kappa'$ ), and thus all resonances are initially in the "under-coupled" regime. Therefore, the bandwidth, based on Eqn.

2.7, is proportional to  $2\kappa + \alpha$ . And the minimum on-resonance transmission, based on Eqn. 2.4, is proportional to  $\frac{\alpha}{2\kappa + \alpha}$ . Neglecting any weak dependence of  $\alpha$  on the wavelength, we can easily conclude that the larger the coupling  $\kappa$ , the broader the resonance, and at the same time, the smaller the minimum transmission or the higher the extinction ratio. When the effective coupling  $\kappa$  is very small, the resonance is severely "under-coupled" with a very small extinction ratio. In fact, at the resonance marked by the arrow in Figure 2.9.a, the effective coupling is very close to its minimum, and the resonance has so small an extinction ratio that it is almost buried in the Fabry-Perot oscillations.

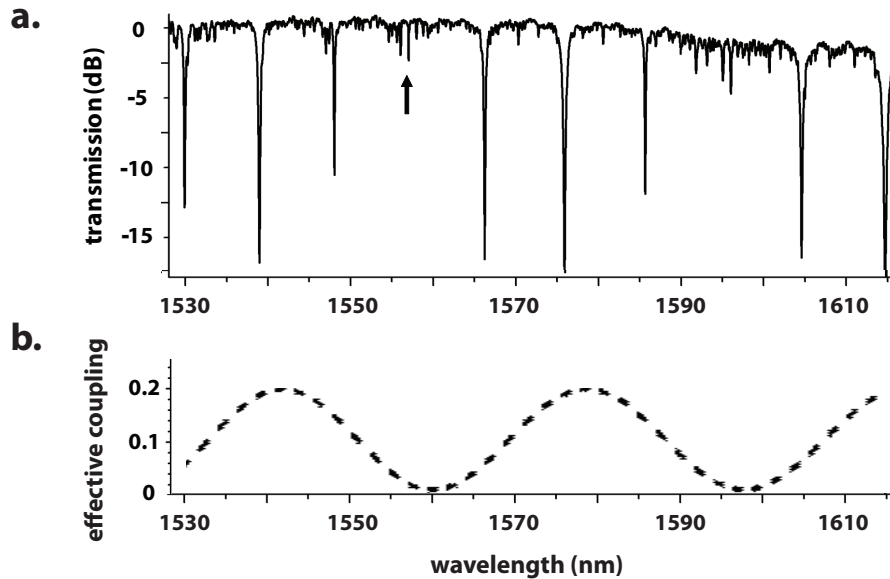


**Figure 2.9.** Optical response of the resonator with interferometric couplers prior to any thermal tuning. **a.** The transmission of the through port as a function of wavelength. **b.** The effective power coupling of the interferometric coupler as a function of wavelength. The oscillation behavior in the effective coupling leads to strong oscillations in the bandwidth and extinction ratio of the resonances.

We then start tuning only one of the two interferometric couplers (the input coupling  $\kappa$ , heater 1) and measure its effect on the optical response of the

resonator. The output coupling  $\kappa'$  is maintained as the same as originally fabricated. The device used here has  $L_b - L_r = 15.53 \mu\text{m}$  and we measure the resonance near 1586 nm. For this particular case, the interferometric coupler is initially in the *destructive* interference regime, i.e., the effective coupling is small. Figure 2.10.a sketches the change of the effective coupling as a function of the heater power. The oscillation here is apparently related to the  $\cos(\Delta\theta)$  term in Eqn. 2.9. The dashed line marks the level for "critical coupling", which corresponds to the sum of the loss and the output coupling. The regions below and above the line correspond to the "under-coupled" and "over-coupled" regimes, respectively. When no heater power is applied, as pointed out before, the resonance (state (I)) is initially "under-coupled" as a result of the symmetrical coupler design. As the heater power increases, the refractive index and the phase in the coupling arm increases, which lead to more destructive interference and even smaller coupling until the minimum coupling state is reached (state (II)). In this case,  $\Delta\phi = 0$  and the interferometric coupler exhibits completely destructive interference. After passing through this minimum state, the effective coupling gradually recovers with further increase in the heater power. It first moves across the "critical coupling" level (state (III)) and finally reaches its maximum value (state (IV)). In this case,  $\Delta\phi = \pi$  and the interferometric coupler exhibits completely constructive interference instead. The change in local temperature is estimated to be over 150°C based on the amount of phase change induced.

Such tuning on the input coupling not only affects the resonance bandwidth but also leads to dramatic change in the extinction ratio. Figure 2.10.b shows the measured transmission spectra corresponding to the four states (I-IV) labeled in Figure 2.10.a. The electrical power consumed by the heater at each state is also

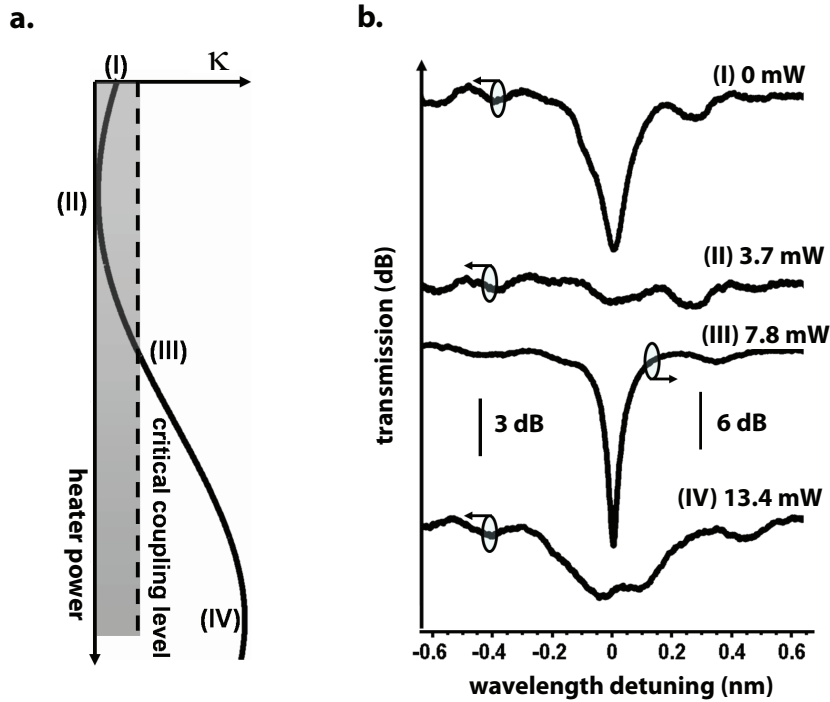


**Figure 2.10.** Changes of the optical response as one starts tuning only the input interferometric coupler with heater 1. **a.** A sketch of the effective input coupling as a function of heater power with four characteristic states labeled as (I) to (IV): state (I), initial state prior to any tuning; state (II), state of completely destructive interference and minimum coupling; state (III), state of critical coupling; state (IV), state of completely constructive interference and maximum coupling. **b.** The transmission spectra corresponding to the four states. The scale bar for state (I), (II) and (IV) is 3 dB, and for state (III) is 6 dB.

shown in the legend. The scale bar for state (I), (II) and (IV) is shown on the left as 3 dB, and that for state (III) is shown on the right as 6 dB. As one can see, at state (I), the resonance has a medium extinction ratio, agreeing with the slightly under-coupled situation. As the input coupling is tuned to its minimum (II), the resonance almost completely disappears. In this case, the resonator is effectively isolated away from the input waveguide due to the completely destructive in-

interference, even though the two coupling points have a strong coupling of  $\sim 5\%$  each. At state (III), the resonance re-appears and shows a large extinction ratio of  $\sim 16$  dB, an indication of being close to the critical coupling condition. State (II) and state (III) form a pair where the resonance itself can be completely switched on and off, which can be used for switching applications<sup>†</sup>. At state (IV) with the maximum coupling, the resonance is severely over-coupled and the resonance becomes very broad and shallow. The fine structures mostly noticeable in state (II) are Fabry-Perot oscillations caused by stitching points on the waveguide.

Tuning both coupling coefficients allows one to vary only the bandwidth while maintaining a high extinction ratio. Figure 2.11 shows the transmission spectra under different heater powers for the same device as Figure 2.9. The path difference of the interferometer is  $L_b - L_r = 15.68 \mu\text{m}$  and we demonstrate the tuning effect near the resonance at 1557 nm as marked by the arrow in Figure 2.9. All the heater powers are adjusted manually while monitoring the transmission spectrum. The horizontal dashed line marks the -3 dB level at which the bandwidth is measured. The spectrum (a) corresponds to the case prior to any tuning, and one can observe a very small extinction ratio as the resonance is severely under-coupled (in the full spectrum shown in Figure 2.9 this resonance is almost buried in the Fabry-Perot oscillations). In order to tune the resonance into the narrowest bandwidth and high extinction ratio, as pointed out before, one needs to tune the output coupling to its minimum ( $\kappa' \sim 0$ ) and the input coupling to match the cavity loss ( $\kappa \sim \alpha$ ). This is achieved at heating powers

---

<sup>†</sup>This is different with typically resonator-based switches where the switching operation is induced by shifting the resonance wavelength relative to the signal wavelength. Here the resonance itself is switched on and off, and therefore does not affect any other signals with wavelengths close to the switched signal. This unique feature is employed to construct spectrally hitless switches [67].

of 5.4 mW (heater 1) and 2.0 mW (heater 2), and the corresponding optical response is shown as spectrum (b) in Figure 2.11. The resonance has a bandwidth of  $\sim 0.1$  nm and an extinction ratio higher than 23 dB. Even higher extinction ratio can be achieved with finer tuning of the heater powers. Once we have this state, we can now continuously increase the resonance bandwidth by adjusting the heating powers simultaneously. As long as both heaters are tuned accordingly to satisfy the critical coupling condition, the large extinction ratio will be maintained. For example, a bandwidth of 0.4 nm is obtained at heating powers of 9.9 mW and 9.3 mW (spectrum (c) in the graph). At heating powers of 14.4 mW and 12.0 mW (spectrum (d)), the bandwidth reaches the maximum of  $\sim 0.7$  nm, which agrees with the expected 0.65 nm.

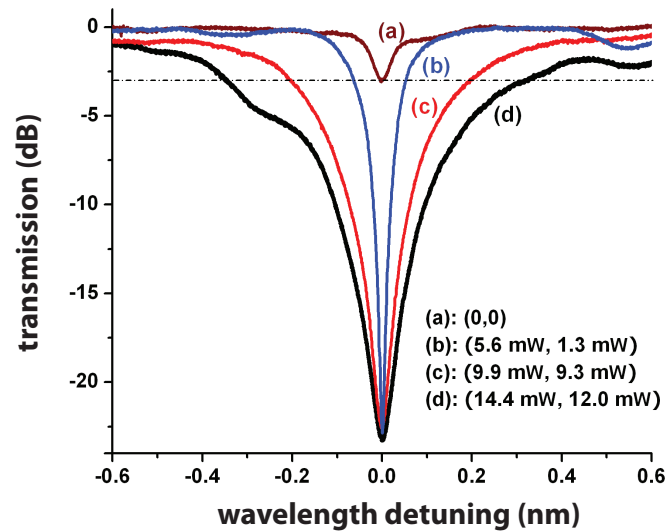


**Figure 2.11.** Tuning the optical bandwidth while maintaining a large extinction ratio by adjusting the heater power for both interferometric couplers. Here (a) corresponds to the state without any tuning, and (b-d) are states with different heater power levels as specified in the legend. The horizontal dashed line marks the -3 dB level at which the bandwidth is measured.

## 2.5 Discussion

The observed minimal bandwidth (0.1 nm) is much larger than the expected (0.01 nm) for two reasons. The first one is that the waveguide loss in this device is much larger ( $\geq 5$  dB/cm) than the 2.5 dB/cm assumed. The excessive loss is attributed to fabrication imperfections, mostly sidewall roughness introduced during the lithography and etching steps. With improved fabrication techniques such as pattern preprocessing and resist reflow, the waveguide loss can be reduced to around 1 ~ 2 dB/cm [46–48, 74, 75]. The other reason is the coupling loss in the four coupling regions. As we use an extremely narrow gap (50 nm) between the coupling waveguides and the ring, the mode perturbation is so strong that it leads to additional mode conversion (scattering) loss [76]. This issue can be avoided by working with quasi-TM (transverse magnetic) polarization, where the mode is less strongly confined and similar coupling level can be achieved with a much larger gap (on the order of 200 nm). Alternatively, one can improve the coupling with a longer coupling region and a larger gap.

The demonstrated maximum bandwidth and electrical power consumption can be both improved with stronger coupling at the four coupling regions. The maximum amount of effective coupling depends on the initial coupling level  $\kappa_0$  (in the weak coupling regime this can be approximated as  $4\kappa_0$ . See Eqn. 2.9). Therefore, a stronger initial coupling can result in larger effective coupling and thus larger bandwidth (compare for example the two curves with different  $\kappa_0$  in Figure 2.6). One can adopt one of the two approaches discussed above to increase the coupling and the maximum bandwidth. The electrical power required for tuning can be reduced by optimizing the waveguide and heater geometries for more localized and efficient temperature change. More interest-

ingly, it also can be reduced with larger  $\kappa_0$ . For a given range of bandwidth tuning, a given range of coupling change is required. And the required tuning range of the phase difference is smaller with a larger  $\kappa_0$ , which implies lower electrical power consumption. This can be confirmed by comparing the two curves shown in Figure 2.6. By incorporating these changes, one can potentially obtain a bandwidth tuning range from 0.01 nm to a few nanometers with even lower electrical power.

The center wavelength of the resonance has a small amount of red-shift ( $< 0.3$  nm) as the bandwidth is tuned with increasing heater power. This is because of two reasons: the first one is that as a small portion of the light circulating in the resonator actually passes through the coupling arms as well, the very large path length change in the coupling arm also affects the total optical path length the light in average experiences and thus the resonance wavelength. Another equivalent way of interpreting this is that the effective coupling coefficient should be a complex number, carrying not only the amplitude but also the phase of the coupled wave. As the coupler changes, this phase term also changes and leads to a change in the total accumulated phase. The other reason is the thermal cross-talk between the coupling waveguide and the waveguide forming the ring, which at the closest place are separated by only 50 nm at the coupling points. The temperature rise in the coupling arm should also lead to small temperature change in the ring. However, such shift in the resonance wavelength should not be a serious concern since it can be easily stabilized with an additional heater on top of the ring, offsetting the ring temperature by a few degrees only.

In conclusion, using a novel resonator design with interferometric coupler

and integrated microheaters, we demonstrate resonators with a bandwidth continuously tunable from 0.1 nm to 0.7 nm, an extinction ratio higher than 23 dB, and a footprint less than 0.001 mm<sup>2</sup>. With improved coupling design and fabrication processing, an ultra broad tuning range from 0.01 nm to a few nm can be obtained. Such functionality and compactness can be very useful for applications such as reconfigurable filters, switches, tunable optical delays and dispersion compensations in on-chip optical interconnects.

## CHAPTER 3

### HIGH EFFICIENCY INTEGRATED GERMANIUM DETECTORS FROM LOW TEMPERATURE PROCESSES

Photodetectors are the ending nodes of a photonic circuit. As one of the two key interfaces between the electrical circuit and the photonic circuit<sup>†</sup>, their performances are crucial for on-chip optical interconnect applications. Unlike most other silicon-based photonic components such as modulators and switches where the material - silicon - is readily available [16–18, 29], photodetectors generally require integration of another material onto silicon to absorb light and generate electrical signals. Therefore not only we need to develop detectors of very good performances to ensure the optical interconnect is overall more advantageous than the electrical one, but their integration with other silicon photonic components and their processing compatibility with the electronics are serious concerns.

In this chapter we demonstrate the first integrated germanium photodetector using wafer bonding and ion-assisted layer splitting technique [36]. We transfer a thin layer of crystalline germanium onto a silicon photonic layer, and demonstrate germanium detectors integrated on sub-micrometer silicon waveguides with low dark current ( $\sim 100$  nA), very good efficiency ( $> 90\%$ ), very small capacitance ( $\sim 2$  fF). These characteristics together should allow detecting low power optical signals with small electrical power consumption, which is important for on-chip applications. More importantly, the devices are fabricated with a unique low temperature process that is compatible with the CMOS back-end integration scheme. Its capability for large wafer scale fabrication and its po-

---

<sup>†</sup>The other interface is electrooptical modulators converting signals from the electrical domain to optical domain.

tential for monolithic integration with other silicon photonic components are particularly appealing for on-chip optical interconnect applications.

## **3.1 Introduction**

### **3.1.1 Requirements for on-chip photodetectors**

For on-chip optical interconnect applications, as pointed out earlier, there are two sets of requirements for photodetectors. Firstly, they should exhibit high performances in aspects including efficiency, bandwidth, power consumption etc. This is crucial in ensuring that the proposed optical interconnect system can be overall more advantageous than the electrical interconnects. Detailed discussion on these characterizations can be found in the next section.

Secondly, the detectors should be integrable with not only other functionalities of a photonic circuit but also the CMOS electronics. Full analysis on this issue requires systematic evaluation of various aspects of the interconnect strategy and thus is beyond the scope of this dissertation. Here instead we focus on two particular aspects regarding the system integration, namely the waveguide-integrated configuration and the compatibility in processing temperature.

Waveguide-integrated detectors possess two advantages. It first allows simple scheme of optical coupling between other planar photonic components and the detectors. This gives a large freedom to circuit design and allows potentially monolithic integration of the entire photonic circuit, which can significantly reduce the process complexity and enable more compact systems. On the contrary, non-waveguide-integrated detectors usually require beam deflec-

tion components and are often integrated at the packaging level, resulting in larger size and higher cost. The waveguide-integrated configuration also decouples the characteristics in bandwidth and efficiency, which are often linked against each other in non-waveguide-integrated detectors. It allows fast carrier collection over small transverse dimension (cross-section) of the detector for large bandwidth while the longitudinal dimension (length along the beam propagation direction) of the detector can be sufficiently long to ensure high efficiency.

Compatibility of processing temperature of the detectors with the CMOS electronics is one of the most critical concerns. For the back-end integration scheme where the photonics is laid on top of the electronics after metallization steps for transistors – one of the most widely discussed schemes – the temperature of any subsequent processes should not exceed 450°C. Therefore, the photonic circuits need to be built within such a strict constraint.

Semiconductors photodetectors are the best candidate for on-chip detectors [77–79]. Commonly used materials include silicon, germanium and InGaAsP etc. The basic principle is the internal photoelectric effect, where the optical absorption generates electron-hole pairs whose internal transport forms macroscopic electrical current. Because of their high efficiency of converting photons to electrons and holes and the large mobility of these carriers, they can have close to ideal efficiency with response time as short as a few picoseconds. Compared with other detectors such as photoemission detectors and thermal detectors, they are faster, more efficient, and easier to integrate with semiconductor-based electronics and photonics.

### 3.1.2 Basics of semiconductor photodetectors

Semiconductor photodetectors rely on strong optical absorption and efficient generation of free electrons and holes, as illustrated in Figure 3.1. This is usually associated with inter-band transitions of electrons from the valence band (nearly full of electrons) to the conduction band (nearly empty of electrons) [78]. The cutoff wavelength thus is determined by the minimum energy difference between the two bands (i.e., the band gap) as a result of energy conservation:  $\lambda_c = h \cdot c / E_g$ , here  $h$  is the planck constant,  $c$  is the speed of light in vacuum, and  $E_g$  is the band gap energy. In these transitions, the total momentum should be conserved as well. In germanium for example, the smallest energy band gap at room temperature is an *indirect* gap<sup>†</sup> of 0.66 eV, corresponding to a cutoff wavelength of 1.88  $\mu\text{m}$ . The smallest *direct* band gap, however, is of 0.80 eV and corresponds to a wavelength of 1.55  $\mu\text{m}$ . Since the momentum of photons are almost negligible compared to that of electrons, the transitions across the indirect band gap require the assist of phonons to provide the momentum mismatch and thus have much lower probabilities (three-particle processes) than the transitions across direct band gap (two-particle processes). Therefore at wavelength above 1.55  $\mu\text{m}$ , only the less-probable indirect transitions occur and the absorption coefficient drops rapidly. Besides such inter-band transitions, as shown in Figure 3.1, transitions between the band and impurity levels inside the gap can also be used for detection. One particular example is self-implanted silicon with defect levels created inside the gap to absorb light beyond silicon's original cutoff wavelength of inter-band transitions [38, 39].

The collection of the photo-generated carriers relies on internal carrier trans-

---

<sup>†</sup>The conduction band minimum and the valence band maximum are offset in the momentum ( $k$ ) space, i.e., electrons at these two states have different values of momentum.

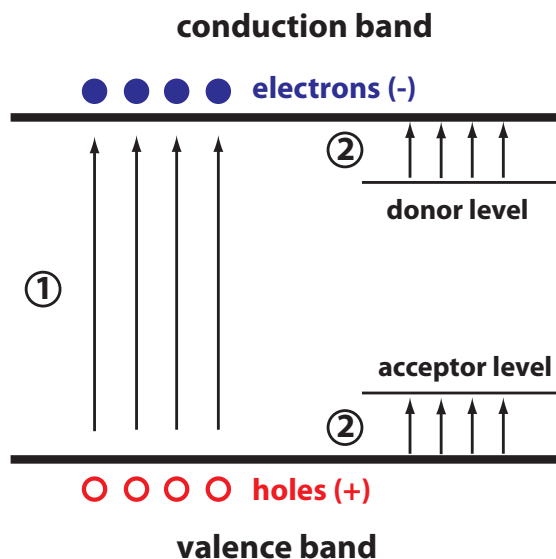


**Figure 3.1.** The electronic transitions in semiconductor photodetectors associated with the absorption of photons, including inter-band transitions generating both electrons and holes, and transitions between the band and impurity levels inside the band gap.

ports, including the intrinsic drift and diffusion processes inherent to semiconductors. Several commonly used structures for carrier collection include p-n junction, p-i-n junction and metal-semiconductor-metal (MSM) configuration. The drift process is referred to the uni-directional motions of each type of carriers with the presence of electrostatic field from either built-in potential (in the cases of p-n or p-i-n junctions) or external bias (in the case of MSM). In the potential picture, as illustrated in Figure 3.2.a, the energy bands in the semiconductor are no longer flat but tilted and position dependent as a result of the potential change under the electrostatic field. The photo-generated electrons in the conduction band flow down the slope (lower potential energy for electrons) while the holes in the valence band flow up the slope (lower potential energy for holes). In the particle picture, electrons (negatively charged) and holes (positively charged) experience Coulomb forces with opposite directions

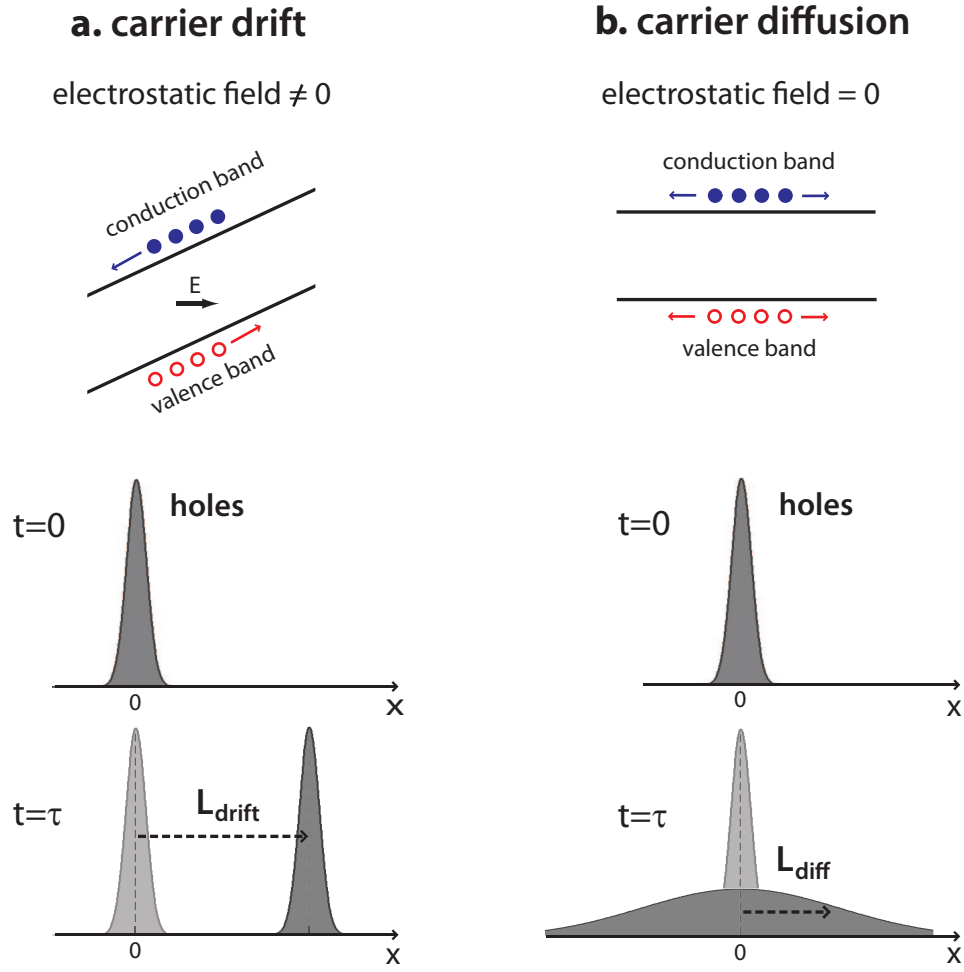


**Figure 3.2.** Transport of photo-generated carriers in the semiconductor. **a.** Drift process in the *depleted* region: the carriers experience directional motion driven by the electrostatic field. **b.** Diffusion process in the *non-depleted* region: the carriers experience thermal motions driven by the gradient of carrier concentrations.

and moves correspondingly. This spatially separates the carriers and removes them from the regions where they are generated. Such regions are thus called *depleted* regions where no free carriers present. This motion is illustrated in Figure 3.2.a with a bundle of holes. The diffusion process, on the contrary, is a non-uni-directional carrier transport induced by thermal random motions of

carriers driven by the gradient of carrier concentrations. In the potential picture, as illustrated in Figure 3.2.b, the energy bands are spatially uniform (flat). For carriers generated in the center, therefore, all positions have the same potential energy and are equally favorable, and the random motions thus spread out the electrons and holes along both directions. In an infinite crystal this leads to eventually homogeneous carrier distribution, which is also illustrated in Figure 3.2.b with a bundle of holes. Similar to the case above, such regions without electrostatic field are called *un-depleted* regions. In the case of detectors with finite dimensions, the removal of carriers near the edges (by either extraction or recombination) can maintain such a gradient till all the carriers generated near the center are gradually driven out. Note that in a symmetric structure pure diffusion alone can not be used to collect the carriers and form a macroscopic current since the electrons (or holes) have the same probability of flowing along two opposite directions. Either geometric or potential asymmetry has to be used to obtain such a current.

For on-chip applications there are several key aspects of the detector performances, including efficiency, dark current, bandwidth, noise, power consumption etc.

- **Efficiency or responsivity.**

The (quantum) efficiency and responsivity both measure the magnitude of a detector's electrical response to an optical illumination. They depend on the efficiency of converting photons to free carriers and the efficiency in collecting these carriers. The quantum efficiency ( $\eta$ ) is defined as the ratio of the number of photo-generated electron-hole pairs collected to the number of incoming photons. The responsivity ( $R_{ph}$ ) is defined as the amount of photocurrent per

unit power of optical illumination, in ampere per watt (A/W). Apparently they are related as

$$R_{ph} = \eta \cdot q \cdot \frac{\lambda}{hc} = \eta \cdot \frac{\lambda \text{ (in unit of } \mu\text{m)}}{1.24}, \quad (3.1)$$

where  $q$  is the unit charge of electrons or holes,  $\lambda$  is the wavelength of the optical illumination, and  $h$  and  $c$  are the planck constant and the speed of light in vacuum, respectively.

- **Dark current.**

Dark current is the current flowing through the detector in the absence of any optical illumination. For the signal to noise ratio concern, as discussed in the next section, a larger dark current requires higher optical power for the same level of reliable detection. It usually comes from two sources: one is from the bulk material, such as thermally generated carriers, impurities and crystalline defects; the other important source is linked to the surfaces properties, such as the dangling bonds at the semiconductor surfaces and the quality of the metal-semiconductor contact interfaces. Therefore, it is desirable to have defect-free crystals, good surface passivation and high quality electrical contacts.

- **Bandwidth or speed.**

The bandwidth or speed measures how fast a detector responds to an optical signal. It is typically determined by three time constants: the intrinsic carrier transport time under drift and diffusion respectively, and the extrinsic time response related to the detector capacitance.

**a. Drift time ( $t_{drift}$ ):** the time required for the carriers generated in the *depleted* region to be collected through uni-directional motions under electrostatic field (see Figure 3.2.a). In equilibrium it can be approximately treated

as a linear motion with a constant velocity which is dependent on the field strength. And the drift time can be estimated from the distances the carriers need to travel and the velocities of the carriers<sup>†</sup>. In weak field regime the velocity is linearly proportional to the electrostatic field with the linear coefficient defined as the carrier mobility. A larger velocity and smaller drift time can be obtained as the electrostatic field increases (from a stronger bias, for example). Under sufficiently strong electrostatic field, the linear relation breaks down and the carrier velocity becomes saturated due to the interactions of these energetic carriers with optical phonons [78]. The minimum drift time can be estimated as  $t_{drift} \sim L_{drift}/V_{sat}$ , where  $L_{drift}$  is the average distance the carriers travel, and  $V_{sat}$  is the saturated carrier velocity<sup>‡</sup>. For example in germanium,  $V_{sat}$  is about  $6 \times 10^6$  cm/s for both electrons and holes [81], and the minimum drift time for a drift length of 1  $\mu\text{m}$  is approximately 16 ps.

**b. Diffusion time ( $t_{diff}$ ):** the time required for carriers generated in *non-depleted* region to be collected through thermal random motion driven by the gradient of carrier concentrations. As pointed out earlier, the diffusion process alone is insufficient in collecting the photocurrents, and the drift process have to be employed to variable extent. Despite the large thermal velocities, the diffusion process is usually much slower than the drift process in *directional* transport because of the randomness in thermal motion. For carriers

---

<sup>†</sup>For transport over very short distances (on the order of few hundred nanometers or less), non-equilibrium transport becomes important and the carrier dynamics need to be taken into account [80].

<sup>‡</sup>In semiconductors such as GaAs and InP whose band structures have multiple closely spaced band minima (maxima), the carrier velocities exhibit more complex dependence on the electrical field than the simple saturation phenomenon discussed above which applies to silicon and germanium. In these materials, the energetic carriers can undergo transitions from one valley to another. As these valleys have different effective masses, the same limit of carrier energy (the optical phonon energy) corresponds to different limit in carrier velocities. As a result of this, before its eventual saturation, the carrier velocity exhibits a distinct peak (electrons in one valley) which can be significantly larger than the final saturated value (electrons in another valley).

to spread to a distance  $L_{diff}$  (diffusion length) away from their origin, the average time is  $t_{diff} \sim L_{diff}^2/D_{e,h}$ , where  $D_{e,h}$  are the diffusion coefficients for electrons and holes respectively and are related to their mobilities as well. In germanium, for example, with diffusion coefficients of 100 and 50  $\text{cm}^2\text{s}^{-1}$  for electrons and holes, the diffusion time for a length of 1  $\mu\text{m}$  are 50 ps and 100 ps, respectively. These are several times longer than the drift time calculated above. To obtain very fast carrier transport it is thus important to reduce the reliance on diffusion as much as possible.

**c. Resistive-Capacitive delay ( $t_{RC}$ ):** the time required for the external circuit to provide necessary charges to balance the internal carrier transport, i.e., to charge or de-charge the detector capacitor  $C$  through a resistor  $R$ . Figure 3.3.a shows a simplified equivalent circuit for a typical detector, where it is treated as a combination of a current source  $I_s$ , a junction capacitor  $C_d$ , a shunt resistor  $R_d$ , and a series resistor  $R_s$ , and  $R_l$  is the load resistance. From simple circuit theory we can derive that for an impulse signal at  $I_s$  the output voltage signal varies as  $e^{-t/t_{RC}}$  where the time constant  $t_{RC} = [R_d/(R_l + R_s)]C$  is called RC time or RC delay. In many practical cases  $R_d$  is very large and  $R_s$  is small, so the RC delay can be simply written as  $t_{RC} = R_l C$ . This RC delay poses an extrinsic limit on the detector bandwidth, written as  $f_{RC} = 1/2\pi t_{RC}$ . To prevent such RC delay from limiting the detector bandwidth, it is therefore crucial to design detectors with small enough capacitance. Furthermore, a smaller capacitance will allow a larger load resistance and thus a stronger voltage output without limiting the detector bandwidth. This leads to a higher sensitivity and a lower power consumption, both of which are important for on-chip interconnect applications.

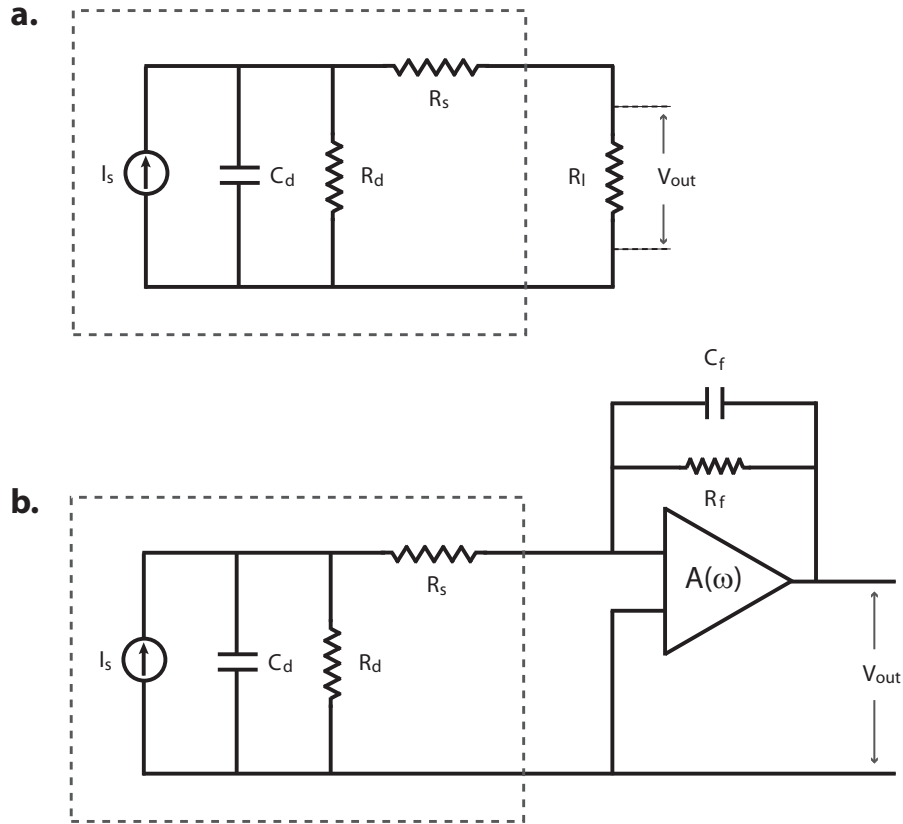


**Figure 3.3.** Simplified equivalent circuit for detector applications. A typical detector can be treated as a combination of a current source  $I_s$ , a junction capacitor  $C_d$ , and a series resistor  $R_s$ . **a.** Detector terminated with a load resistor ( $R_l$ ). **b.** Detector terminated with a transimpedance amplifier with a feedback resistor  $R_f$  and a stabilizing capacitor  $C_f$ .

- **Noise.**

Detector noise is the random fluctuation in the current or voltage output that often limits the minimum signal one can reliably detect. The noise intrinsic to a photodetector can be written as [77]

$$i_n = \sqrt{4kTf/R + 2q(I_{dark} + I_{photo})f}. \quad (3.2)$$

The first term is associated with Johnson or thermal noise of a resistor  $R$ , with  $k$  as the Boltzmann constant,  $T$  as the absolute temperature,  $f$  as the 3-dB

bandwidth. The second term is associated with the quantum shot noise from the discrete nature of the electrons and holes, with  $q$  as the unit charge of an electron or hole, and  $I_{dark}$  and  $I_{photo}$  as the dark and photo-generated current. As a comparison, for example, at room temperature, assuming a current of 1 mA and a resistance of 50  $\Omega$ , the two terms have about the same magnitude. With sufficiently strong optical input the shot noise dominates, leading to a signal to noise ratio of  $\sqrt{N_{ph}}$  where  $N_{ph}$  is the mean number of photons detected per bit. For the case of low signal level and low dark current, which is the case desirable for integrated photonic circuits, the thermal noise dominates and a load resistance as large as possible will lead to minimized noise. This again requires a small enough detector capacitance to avoid limiting its bandwidth.

- **Power consumption.**

Power consumption is another major characterization of detectors, especially for on-chip applications which require massive implementation of them. This includes the optical power, the electrical power provided by the bias circuit, and more significantly the power consumption of the electrical amplifying circuits. The optical power is related to the detector efficiency, dark current and noise, and is usually in the few to sub- milliwatt regime. The electrical power from the bias circuit scales with the amount of total current ( $I_{dark} + I_{photo}$ ) and the bias voltage, and can be also in the few or sub-milliwatt regime. The dominant power consumption is often coming from the electrical amplifying circuit, which includes a transimpedance amplifier (TIA) and several other stages of amplifiers, and can consume a few tens of milliwatts or more [82]. The simplified circuit having the load resistor replaced by a TIA is illustrated in Figure 3.3.b. As a result of the active compensation of the amplifier, the RC-

delay can be much smaller than the case of a simple load resistor. However, in general, a smaller detector capacitance  $C_d$  still allows a smaller  $C_f$  and larger  $R_f$ , relaxing the requirement on the amplifier gain and thus leading to lower power consumption.

### 3.1.3 Progresses and challenges

There has been a great amount work on integrated photodetectors on silicon for the aim of optical interconnect applications. The most extensively studied are inter-band transition detectors with germanium [19, 35, 36, 83, 84] or III-V compound semiconductors (AlGaInAs for example) [34] on silicon due to their strong optical absorptions at the telecom wavelengths. Detectors based on other materials have also been reported, such as silicide [37] and self-implanted silicon [38, 39]. Despite their relative simplicity in processing, their performances are generally inferior to that of the inter-band transition detectors.

Germanium is perceived as the best candidate for integrated detectors for silicon photonics, because of its relatively lower cost and compatibility of parallel processing with silicon compared to III-V semiconductors. The parallel processing can potentially allow monolithic integration which can dramatically reduce the cost and complexity. Germanium or silicon-germanium alloy ( $\text{Si}_x\text{Ge}_{1-x}$ ) has been widely used in the CMOS transistors to create strained silicon for improved carrier mobility [85]. However, obtaining high quality germanium on silicon is still a challenge. This is because of the very large lattice mismatch between silicon and germanium (silicon - 5.431 Å; germanium - 5.646 Å; relative difference  $\sim 4.2\%$ ), which induces a large density of dislocation defects dur-

ing the epitaxial growth [86]. This phenomenon is illustrated in Figure 3.4.a. The density of defects can be reduced with specialized growth and post-growth anneal techniques [87], and very good detector performances have been demonstrated [19, 35, 84]. However, it in general still requires a relatively high temperature process typically above 700°C, which is not compatible with the back-end integration scheme which has a strict temperature limit of 450°C.

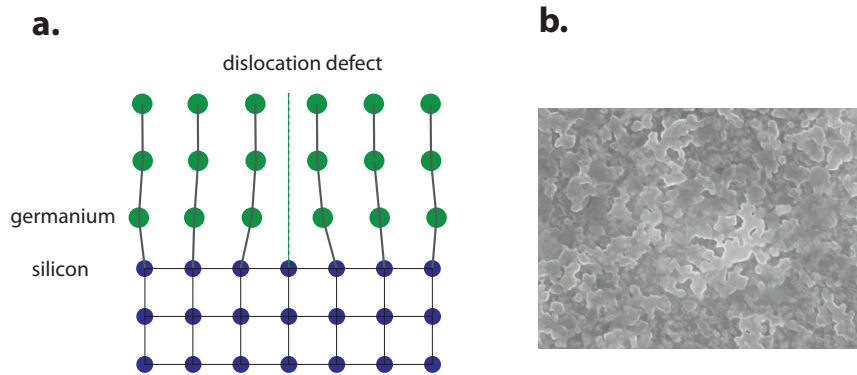


**Figure 3.4.** Challenges in integrating germanium onto silicon. **a.** Schematic of epitaxy growth of germanium on silicon. The very large mismatch in lattice constants (4.2%) between germanium and silicon induces dislocation defects. For improved crystalline quality a relatively high temperature process above 700°C is required, which is incompatible with the back-end integration scheme. **b.** A top-view SEM image of an exemplar poly-crystalline germanium film obtained by room temperature evaporation and subsequent thermal anneal. Though small grains of crystal can be formed, the quality is relatively poor and degrades all aspects of the detector performances.

An alternative way of integrating germanium onto silicon is using poly-crystalline germanium obtained at lower temperature. For example, amorphous germanium can be evaporated onto substrate at room or elevated temperature, and then annealed into poly-crystalline at temperature below 450°C [88]. However, the crystal quality obtained in this way is much poorer, which will severely

degrade all aspects of performances such as efficiency, dark current and speed. Maximum efficiency of only  $\sim 15\%$  has been reported [88]. Figure 3.4.b shows a top-view SEM image of a poly-crystalline germanium film from room temperature electron-beam evaporation and subsequent anneal. One potential approach of obtaining better crystal quality is using laser anneal, where the absorption of a short intense laser beam quickly rises the surface temperature of germanium above its melting point and initiates liquid phase epitaxy (see for example [89]). Grains of micrometer sizes have been reported, and the process is likely to be compatible with the back-end integration scheme provided that careful thermal management can be achieved. However, more extensive characterizations of this technique are needed and are beyond the scope of this dissertation.

On the other hand, III-V multiple quantum well structures have been integrated onto silicon using wafer bonding technique [90]. The quantum wells are first epitaxially grown on a III-V substrate with a sacrificial layer and then bonded to a processed silicon wafer. The III-V substrate and sacrificial layer are then removed, leaving the quantum wells on silicon for subsequent processing. Devices such as lasers, optical amplifiers, modulators [26, 33], and detectors with very good efficiency and dark current have been reported [34]. The drawbacks of this approach, however, include that it can not be performed at large wafer scale (limited to die size) and the relatively high cost associated with the epitaxial growth.

Following the above discussion, the objective of this dissertation on the detectors is to integrate high quality, single crystalline, waveguide-integrated germanium detectors onto silicon photonic circuits at large wafer scale, and from a relatively low temperature process compatible with the CMOS back-end in-

tegration scheme. High quality bulk germanium wafers of large diameters are readily available commercially. And wafer bonding is a viable approach for integrating very different materials at relatively low temperatures. However, the real challenge is how to integrate only a thin layer of germanium of sub-micrometer thickness onto silicon, instead of a bulk germanium with a few hundreds microns. In the case of III-V hybrid structure, the substrate and sacrificial layer is removed after wafer bonding, leaving only the thin active layers on silicon. In principle, similar approach can be adapted to germanium, i.e., epitaxial growth of germanium layer on a lattice-matched sacrificial layer on an appropriate substrate (GaAs for example, with a lattice constant of 5.653 Å that is only 0.1% larger than germanium). However, this approach eliminates the claimed advantages of germanium compared with III-V in both cost and wafer size.

### **3.1.4 GeOI-SOI from smart-cut at low temperature**

To overcome the above challenge, we use a wafer bonding followed by an ion-assisted layer cutting technique (also called smart-cut) to slice a very thin layer of germanium from its bulk crystalline substrate and transfer it to a silicon substrate (see [91] and references therein). With this approach, we are able to obtain what we call GeOI-SOI wafers, i.e., a layer of high quality crystalline germanium (Ge) on a thin insulating layer ( $\text{SiO}_2$ ) on a standard silicon-on-insulator (SOI) substrate. As shown in this and the next chapter, with such GeOI-SOI wafers we demonstrate waveguide-integrated detectors with high efficiency, low dark current, ultra-low capacitance, and very fast response. We also demonstrate a WDM detection system with monolithically integrated silicon demultiplexer and germanium detectors.

The very basic principle of this technique is sketched in Figure 3.5.a. A bulk germanium wafer is first implanted with hydrogen ions and then bonded to a SOI wafer coated with a layer of  $\text{SiO}_2$  at room temperature. After anneal at medium temperature to strengthen the bonding interface, the two wafers are separated at a depth inside the germanium wafer where the implanted dopants has considerably weakened the crystal. As a result a thin layer of crystalline germanium is transferred from the bulk wafer onto the SOI wafer. For details about the physical mechanism and fabrication techniques, the readers can refer to reference [36, 90] and references therein. Using this technique, one can obtain high quality germanium films free of dislocation defects that are inherent to epitaxially grown germanium. Figure 3.5.b shows a cross-sectional SEM image of the GeOI-SOI wafer, with approximately 250 nm of germanium, 40 nm of intermediate  $\text{SiO}_2$ , 230 nm of silicon, and 3  $\mu\text{m}$  of  $\text{SiO}_2$ . With such a wafer, a photonic circuits incorporating passive optical components, active silicon modulators and germanium detectors can be fabricated monolithically using standard CMOS processes.

One particular aspect regarding germanium integrated on silicon is the strain in the germanium film. Large tensile strain up to 0.20% in germanium epitaxially grown on silicon has been observed, which shrinks the direct band gap of germanium by about 30 meV and thus shifts the corresponding wavelength from around 1540 nm to 1605 nm [92, 93]. This not only leads to even stronger optical absorption at wavelength below the original direct band edge but also extend the spectral range of strong absorption to cover the entire C-band and most of the L-band [93–95]. This large strain is suspected to originate from the mismatch of thermal expansion coefficients between germanium and silicon and the high growth temperature. On the contrary, no strong strain

in the layer-transferred germanium film is expected since the bonding is initiated at room temperature and subsequently annealed at fairly low temperature ( $100^\circ \sim 250^\circ$ ) prior to the layer splitting. Therefore the band edge and optical absorption coefficient are expected to be close to those of crystalline bulk germanium. This is indeed experimentally confirmed with the spectral dependence of the detector responsivity which shows flat photocurrent response up to around 1540 nm and starts rolling-off at longer wavelengths (see the measurement results in this Chapter). The desirable tensile strain and band gap shrinkage can be also induced using other techniques such as silicidation of the back-side of the silicon substrate, and additional extension of 15 nm in wavelength has been reported [96].

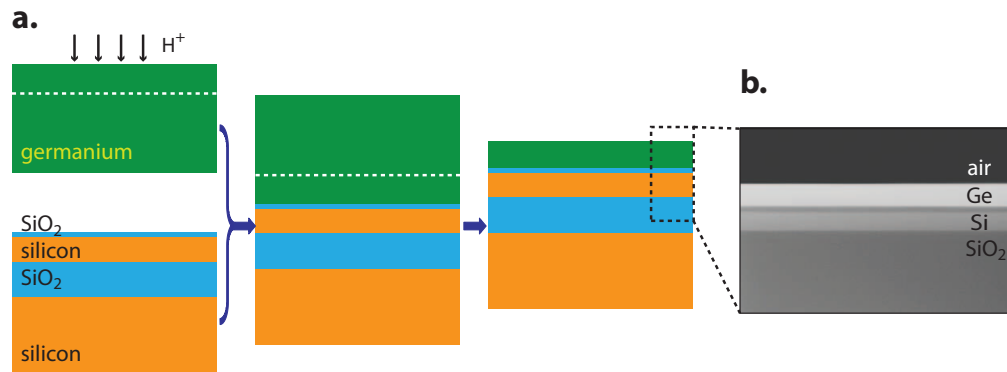


**Figure 3.5.** Integration of a thin layer of crystalline germanium onto silicon. **a.** Schematic of the wafer bonding and ion-assisted layer cutting technique. **b.** Cross-sectional SEM image of GeOI-SOI wafer, with the transferred crystalline germanium film on an insulating layer (SiO<sub>2</sub>) on a silicon-on-insulator (SOI) substrate.

## 3.2 Design of integrated detectors on GeOI-SOI

Based on such GeOI-SOI wafers, we design a waveguide-integrated detector with metal-semiconductor-metal (MSM) configuration. Figure 3.6 shows the schematic and cross-section of the design. In this particular case, the silicon layer is processed prior to bonding. The very thin layer of SiO<sub>2</sub> between the Ge layer and the silicon layer is used to electrically isolate them, preventing the photo-generated carriers in germanium from diffusing into silicon which slows down the response. At the same time, it still allows strong optical coupling from the silicon waveguide to the germanium region. Since the carrier transport takes place only in the Ge layer and thus imposes no electrical requirement on the waveguide layer, one can fabricate the photonic circuits using materials which can be deposited on top of a CMOS chip such as amorphous or poly-crystalline silicon [23, 24]. This is in contrast to detectors that require the use of single crystalline silicon for either Ge epitaxy growth or carrier transport [19, 35]. On top of the Ge pad two metal electrodes made of thin layers of titanium and gold are placed to form the planar MSM geometry. Here we chose Ti as the metal forming the metal-Ge schottky barrier, since it has been reported to give relatively lower dark current compared to other metals such as Cr and Ni [97]. And gold is used for the ease of electrical probing and its slightly weaker optical absorption [98].

We analyze the optical mode properties of the detector design. Figure 3.7.a shows the optical mode profiles of the first and second order quasi-TE (transverse electric) modes excited in the photodetector region along with the mode of the silicon waveguide. These modes are calculated using finite-difference mode solver with dimension as follows: the silicon waveguide is 500 nm by 230

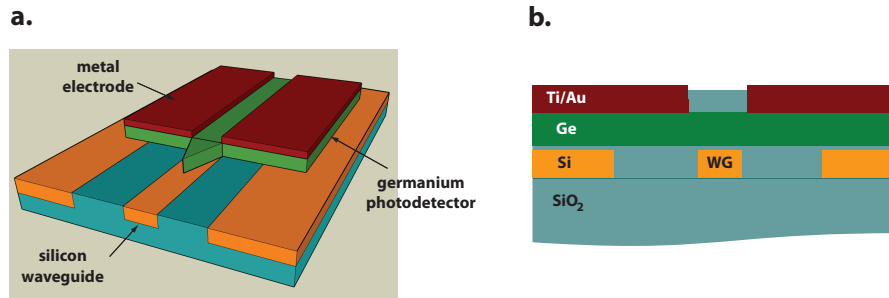


**Figure 3.6.** Design of integrated germanium photodetector on a silicon waveguide. **a.** 3D schematics. **b.** the device cross section.

nm, the Ge slab thickness is 250 nm, the SiO<sub>2</sub> isolation layer is 40 nm thick, and the gold electrodes are 100 nm thick with spacing of 750 nm. The refractive indices of Si, Ge and SiO<sub>2</sub> are 3.48, 4.36 and 1.46 respectively. One can see for the fundamental detector mode most of the light is tightly confined in germanium between the gap, while for the second order mode part of the light is in the germanium and the other part in the silicon waveguide underneath. Such strong confinement in the germanium provides efficient optical absorption. The origin of the strong horizontal confinement in germanium is not from the underlying silicon waveguide but from the planar electrodes, which push light away from the regions underneath them for quasi-TE polarized light<sup>†</sup>.

We use short tapers in germanium to reduce the back-reflection at the detector interfaces. From finite-difference time-domain (FDTD) simulations, the reflection back to the silicon waveguide from the abrupt waveguide-to-detector interface (without any taper) is calculated to be about -20 dB. The reflection level is so low because of the strong optical confinement of the input silicon waveguide (as shown in Figure 3.7.a). Therefore only a very small portion of light actually sees that interface. Further reduction in reflection, if desired, can be

<sup>†</sup>This can be easily understood since for quasi-TE light the electrical field is mostly aligned horizontally, which is tangential to the metal-germanium interface and thus vanishes.

achieved by slightly increasing the waveguide dimensions or the thickness of the isolation  $\text{SiO}_2$  layer. In the present case, we use short germanium tapers at the interfaces. With a quadratic taper of approximately  $4\ \mu\text{m}$  long and  $50\ \text{nm}$  wide at the tip, we reduce the reflection level to below  $-25\ \text{dB}$  based on FDTD simulations.

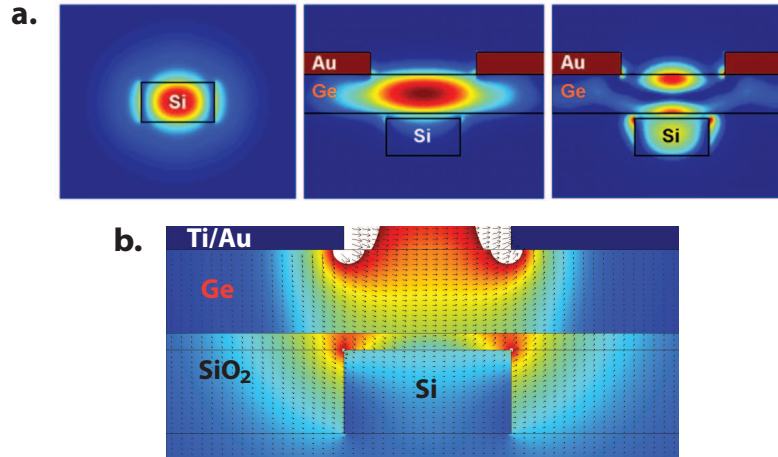


**Figure 3.7.** Optical and electrical modeling of the integrated germanium detector. **a.** Optical mode profiles for quasi-TE polarization of the input silicon waveguide and the two modes excited in the photodetector region. **b.** Distribution of the electrostatic field in the germanium region when an external bias is applied between the two electrodes. The field is intentionally saturated near the corners to reveal the details.

A detector of high efficiency requires efficient conversion of photons to electron-hole pairs. This can be decomposed to two factors. Firstly, the detector should be sufficiently long to ensure that the light is completely absorbed. Secondly, the amount of *useful* absorption by the germanium (which generates electron-hole pairs) should dominate compared with the *useless* absorption by the metal electrodes (which converts photons mostly to heat only). In our case, germanium exhibits very large absorption coefficient for wavelength less than

1540 nm as a result of direct inter-band transition. If the light is entirely in germanium, a length of less than 10  $\mu\text{m}$  is sufficient to absorb almost all the light [94, 95]. In the actual waveguide detector, light couples rapidly back and forth between the silicon region and the germanium region<sup>†</sup>. Therefore, a larger length is required. Here we use a length of 30  $\mu\text{m}$  to ensure full absorption of light. Also, as shown in the mode profiles in Figure 3.7.a, there is only a very small overlap of the optical field with the electrodes, therefore the detector efficiency is expected to be only slightly reduced by the metal absorption. For wavelength above 1540 nm, however, only indirect inter-band transition is allowed in germanium, and the optical absorption coefficient drops rapidly. Therefore the percentage of the electrode absorption becomes more and more significant, leading to decreasing detector efficiency. This problem can be partially resolved with optimized electrode design to move the electrodes further away from the optical field.

The photo-generated carriers are collected using electrostatic field provided by external bias across the two planar electrodes. Figure 3.7.b shows the distribution of the electrostatic field in the detector cross-section. Strong field is observed in the germanium region between the two electrodes, which coincides with the region where most of the light is confined. This electrostatic field separates the photo-generated electrons and holes and move them along opposite directions with Coulomb forces. This can also be illustrated in the band graph in Figure 3.8, which shows both the tilted valence and conduction bands inside the germanium and the Schottky barriers formed at the metal-germanium interfaces. The electrons in the conduction band move down the slope and reach

---

<sup>†</sup>This is similar to the usual phenomenon in directional couplers. The coupling length, because of the large difference in the mode indices, is as short as a couple of micrometers. Note that due to the phase mismatch, the energy transfer between the silicon and germanium regions is not complete.

the left electrode without any barrier. The holes in the valence band move up the slope and reach the right electrode through a small barrier. The profile of the Schottky barrier is highly dependent on the electronic properties of the germanium surfaces and the metal-germanium interfaces, and strongly affects the dark current will be discussed in a little more details in the discussion section.

The compact, integrated detector should exhibit very small capacitance and short drift time. Using simple parallel-plate model, the capacitance of our detector is estimated to be approximately 2 fF only. This comes from the use of very thin germanium layer ( $\sim 250$  nm) and a small length ( $30 \mu\text{m}$ ). As a result, the equivalent area in analogy to a parallel-plate capacitor is only  $7.5 \mu\text{m}^2$ . Also, the gap between the electrodes is only 750 nm. Recalling the saturated carrier velocities of  $6 \times 10^6$  cm/s for both electrons and holes, one can estimate that the average carrier drift time should be less than 10 ps. This thus allows very high speed operations.

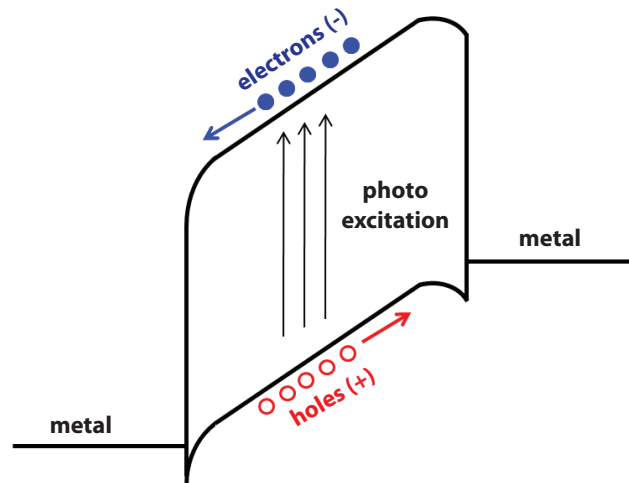


**Figure 3.8.** Energy band graph and carriers collection of the metal-germanium-metal detector under a bias.

### 3.3 Device fabrication

The integrated detector is fabricated by combining the smart-cut technique in obtaining GeOI-SOI wafers and other standard CMOS processes. The process flow is shown briefly in Figure 3.9. The fabrication is done with full 4-inch wafers and can be scaled to larger diameters. For compatibility with the CMOS back-end integration scheme, the processing temperature is maintained  $\leq 400^\circ\text{C}$ . In this particular case, the silicon wafer is patterned prior to bonding and germanium layer transfer while in later generations of devices all lithography processes are done after bonding.

**Prior processes on the Ge wafer (a-c).** First a 4-inch intrinsic germanium wafer (from Umicore, resistivity  $> 40 \Omega$ ) is capped with 100 nm  $\text{SiO}_2$  by PECVD at  $400^\circ\text{C}$ , and ion implanted with hydrogen ions with dose of  $4 \times 10^{16} \text{ cm}^{-2}$ , energy of 80 KeV, and  $7^\circ$  tilt. This corresponds to a projected implantation depth of 670 nm into the germanium crystal based on simulations of ion stopping kinetics (with the software SRIM, The Stopping and Range of Ions in Matter [99]). Due to the very high dose and the lack of active cooling during the implantation, the implantation is performed at two separate steps with a pause in between for cooling. The  $\text{SiO}_2$  capping layer is used to protect the germanium surface during the implantation and is subsequently removed with diluted hydrofluoric (HF) acid.

**Prior processes on the SOI wafer (d-f).** Silicon waveguides are first defined using electron-beam lithography and dry etching on a 4-inch SOI wafer (from SOITEC, with 230 nm silicon and 3  $\mu\text{m}$  of buried  $\text{SiO}_2$ ). First a thin layer of  $\text{SiO}_2$  is deposited as a hard mask, and a layer of positive electron-beam resist

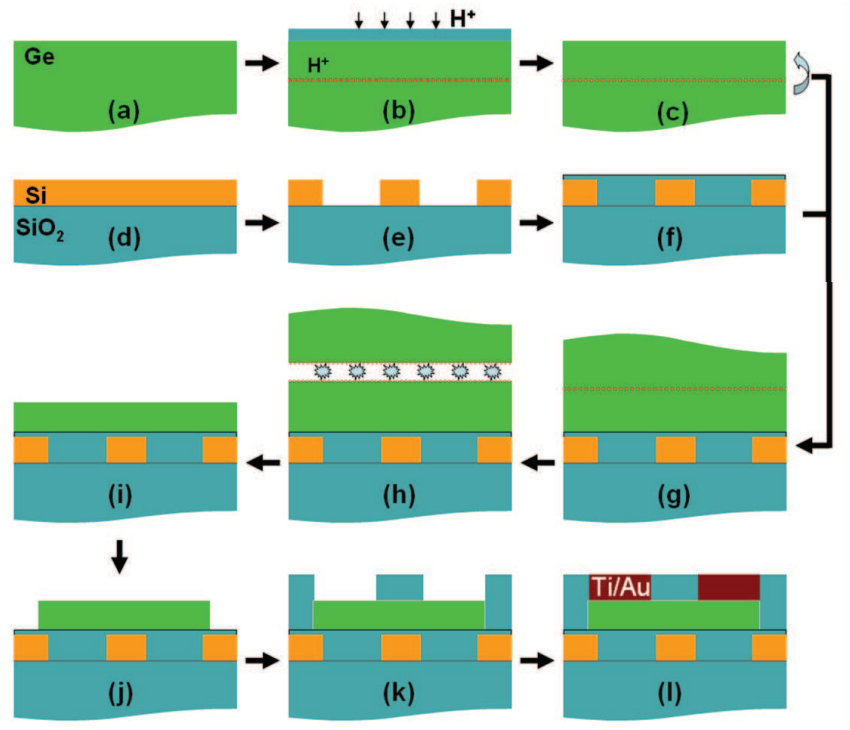


**Figure 3.9.** Fabrication process for the integrated Ge detector on silicon waveguides. **a-c.** Prior processes on the Ge wafer, including SiO<sub>2</sub> deposition, hydrogen implantation, and SiO<sub>2</sub> removal with HF. The red dotted line indicates implantation depth. **d-f.** Prior processes on the SOI wafer, including patterning of Si waveguides, SiO<sub>2</sub> deposition, and SiO<sub>2</sub> CMP planarization. **g-i.** Formation of GeOI-SOI, including wafer bonding, layer splitting, and Ge CMP planarization. **j-l.** Formation of the detectors, including patterning of the Ge layer, SiO<sub>2</sub> deposition, via etch and electrodes deposition.

(PMMA) is spin-coated. After exposure the resist is developed and the pattern is transferred sequentially to the SiO<sub>2</sub> mask layer and the silicon layer using dry etchings. The wafer is then coated with PECVD SiO<sub>2</sub> cladding layer of ~ 700 nm, and planarized with chemical mechanical polishing (CMP) down to a thickness of approximately 40 nm above the silicon surface. This SiO<sub>2</sub> layer acts as the bonding interface and the electrical isolation layer between the germanium

layer and the underneath silicon.

**Formation of GeOI-SOI (g-i).** After careful wafer clean and surface treatment, the processed germanium wafer and SOI wafer are bonded at room temperature using hydrophilic direct bonding. More details regarding the bonding and smart-cut process can be found in the Appendix. The SOI wafer is cleaned with heated base, acid, and base sequentially (base-  $\text{NH}_4\text{OH}:\text{H}_2\text{O}_2:\text{H}_2\text{O} = 1:1:6$ , acid-  $\text{HCl}:\text{H}_2\text{O}_2:\text{H}_2\text{O} = 1:1:6$ ,  $70^\circ\text{C}$ ). The germanium wafer is cleaned with another set of acid ( $\text{HF}:\text{H}_2\text{O} = 1:100$ ) and base ( $\text{NH}_4\text{OH}:\text{H}_2\text{O} = 1:3$ ). Note that the  $\text{H}_2\text{O}_2$  used in standard silicon MOS clean is a strong etchant for germanium. After spin dry, the two wafers are bonded together at room temperature and then annealed at  $100^\circ\text{C}$  to enhance the bonding strength. The temperature is then very slowly increased up to  $400^\circ\text{C}$  to initiate the layer splitting, which leaves the germanium film of approximately 670 nm thick on the SOI wafer. A second CMP process is then performed with a trace amount of  $\text{H}_2\text{O}_2$  added into the oxide slurry. This thins down the film thickness to approximately 250 nm and significantly reduces the surface roughness of the germanium film.

**Formation of the detectors (j-l).** The detector patterns are then patterned on the transferred germanium film. A negative-tone resist HSQ is exposed with electron-beam lithography, and germanium is removed everywhere except for the detector patterns using dry etching. Another PECVD  $\text{SiO}_2$  cladding layer of 700 nm is deposited to cover the silicon waveguides to ensure efficient coupling with optical fibers. Vias holes for electrodes are then defined using lithography and dry etch, and 15 nm Ti / 200 nm Au are evaporated to form the Schottky contacts. The electrodes are then connected to Au square pads of  $80\ \mu\text{m}$  located next to the detectors for electrical probing. After this step, the samples are diced

and the input and output facets are mechanically polished for testing.

Figure 3.10 shows several images of the device along with the fabrication process. Figure 3.10.a shows a top view SEM image of the silicon waveguide with a width of 500 nm. Figure 3.10.b shows a top view SEM image of one of the germanium pad with tapers on top of the silicon waveguide. The contrast between the silicon and the SiO<sub>2</sub> trenches is relatively low because the waveguide is planarized with 40 nm SiO<sub>2</sub> on top. Figure 3.10.c shows an optical image of the device after deposition of the via electrodes.

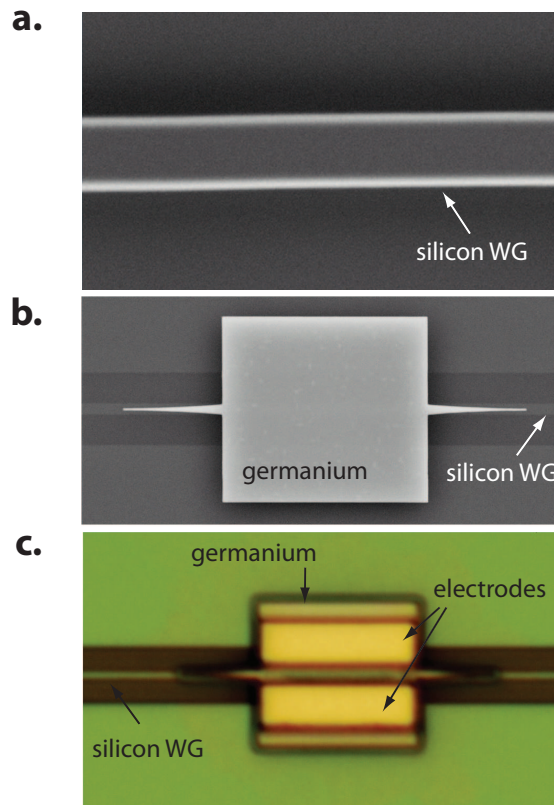


**Figure 3.10.** Device images during the fabrication processes. **a.** SEM top view image of the silicon waveguide without cladding. **b.** SEM top view image of the Ge pad with tapers on top of the silicon waveguide. **c.** Optical image of the fabricated Ge photodetector after deposition of via electrodes.

There are two notes regarding the fabrication process. Firstly, undesirable mechanical stress, when sufficiently large, can interfere successful bonding and layer transfer. The mechanical stress comes from initial wafer bowing of the wafers, subsequent layer depositions, and the very large mismatch in thermal expansion coefficients among germanium, silicon and SiO<sub>2</sub>. In the extreme case, it can even fracture the wafers into pieces during the layer splitting. Secondly, the SiO<sub>2</sub> CMP planarization step is very critical to successful layer transfer. Really flat topology is required to avoid cracks in the transferred germanium film. Also, uniformity in the layer thickness after CMP is difficult to control without a stop layer. In this case of SiO<sub>2</sub> planarization, for a targeted thickness of 50 nm, variation from approximately 40 nm to 70 nm is observed across the 4-inch wafer with an edge exclusion of 15 mm. Similar variation is observed in the polishing of germanium. Even though for the present case this does not adversely affect the detector efficiency since the detectors are sufficiently long to tolerate variation in the optical coupling, and it can be improved with optimized polishing parameters, it can become a problem for more complicated system integrations having tighter margins for variations. Therefore, in later generations of devices we modify the process flow and completely avoid the critical CMP planarization step. All patterning steps are done after the bonding step on a blank GeOI-SOI wafer, allowing monolithic integration of the detectors with other photonic components.

### **3.4 Measurement and results**

We characterize the performances of the integrated germanium detectors and measure a low dark current of  $\sim 100$  nA, a high fiber-accessed responsivity of

$> 0.4 \text{ A/W}$ , and an estimated quantum efficiency of above 90% in our devices.

The measurement setup is shown in Figure 3.11. We launch light from a continuous wave tunable laser to the silicon waveguide and measure the current response of the germanium detector integrated at the end of the waveguide. The polarization of the input signal is tuned to TE polarized through a fiber polarization controller. To increase the coupling efficiency between the fiber mode and the highly confined mode of silicon waveguide, we use a tapered tip at the end of fiber and a nano-taper at the input facet of the silicon waveguide. With this approach a coupling efficiency of approximately -3 dB can be achieved near 1550 nm. To record the current response of the detector, the contact pads of the detector are approached by a double-tipped RF probe, controlled by a three-axis positioning stage and monitored under a microscope and camera. The probe is connected to a Keithley 2400 sourcemeter to apply a bias voltage across the device and at the same time measure the current. To measure the dark current, we switch off the laser source. The sample is mounted on top of a thermoelectric cooling module to maintain a stable temperature around 25°C.

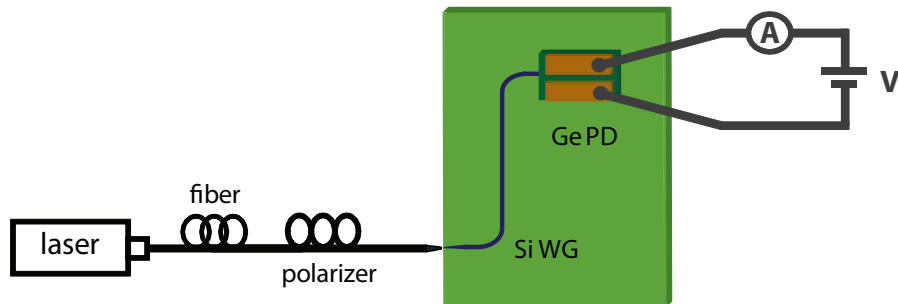


**Figure 3.11.** Setup for characterizing the DC response of the integrated germanium detector.

Figure 3.12 shows an example of the responses of dark current and photocurrent from an integrated detector. The dark current is measured as a function of

bias voltage, and a value of approximately 100 nA for a bias voltage up to 4 V is shown here. This is considerably lower than the previous reported germanium photodetectors using a similar MSM configuration but epitaxially grown germanium [97]. This is attributed to the higher crystal quality of the germanium film obtained from smart-cut compared with the epitaxial growth where the large lattice mismatch induces a large amount of dislocation defects. Figure 3.12 also shows the photocurrent under optical illumination for a wavelength near 1550 nm. The input optical power measured at the end of fiber is 0.95 mW. A photocurrent of approximately 300  $\mu$ A is measured, which corresponds to a large ratio of photocurrent to dark current of  $\sim 3000$  at this illumination level.

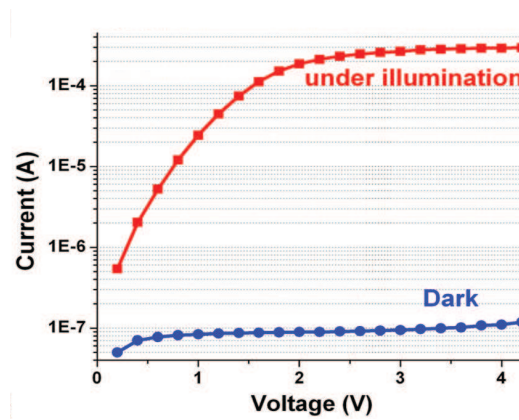


**Figure 3.12.** The dark current and photocurrent response of the detector as a function of bias voltage applied across the planar electrodes.

Figure 3.13 shows the spectrum of the measured fiber-accessed responsivity measured at 3 V bias. A value as high as 0.44 A/W is observed near 1527 nm. If corrected for the coupling loss from the fiber to the silicon waveguide (estimated to be  $\sim -3$  dB) and the propagation loss of the 0.3 cm long silicon waveguide before the photodetector (estimated to be 4-5 dB/cm), the quantum efficiency is estimated to be above 90%. The roll-off in responsivity at longer wavelength is mostly due to the decreasing optical absorption coefficient of germanium as

mentioned earlier, and also partly due to the change in the optical coupling efficiency at the waveguide input facet.

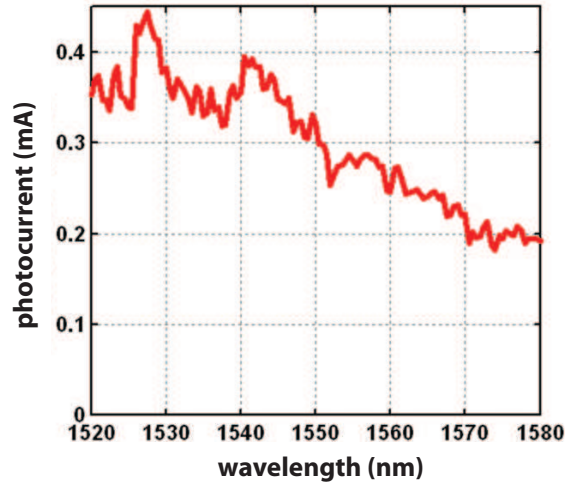


**Figure 3.13.** The spectrum of the detector photocurrent as a function of wavelength.

### 3.5 Discussion

We demonstrate the first integrated germanium photodetector using the wafer bonding and ion-assisted layer cutting technique. The high crystalline quality of the transferred film obtained from a low temperature process is a unique characteristic of this approach. Its lower cost than III-V hybrid structures, its capability for large wafer scale fabrication, and also very importantly the potential for monolithic integrations of the germanium detectors with other silicon photonic components are particularly appealing for on-chip optical interconnect applications.

With this technique, we demonstrate germanium detectors on sub-micrometer silicon waveguides with very low dark current ( $\sim 100$  nA), very

good efficiency  $> 90\%$ , very small capacitance  $\sim 2$  fF. These characteristics together should allow detecting low power optical signals with small electrical power consumption, which is crucial for on-chip applications.

Asides from these good performances, there are also aspects that further improvement can be achieved. Here we discuss two issues: one is further reduction in the dark current, and the other is the speed and bias requirement of the detectors.

### **3.5.1 Further reduction in dark current**

The dark current is particularly important for detecting very weak optical signals on-chip. This is because of the noise inherently associated with the dark current. From the intrinsic detector noise in Eqn. 3.2 we know that detectors with a larger dark current also exhibit stronger fluctuation (noise) in the current, therefore it becomes more difficult to distinguish the response from a weak optical signal from the random fluctuation.

The observed dark current is about 100 nA for up to 4 V bias voltage. This is much lower compared to other MSM detectors based on epitaxially grown germanium. This is expected since the germanium obtained in our smart-cut approach maintains the high crystalline quality of the original bulk germanium wafer. Also in this design the carriers transport occur only in the germanium region, unlike the other cases the transport goes through the germanium-silicon interfaces where a large density of defects exists.

However, the observed dark current is still higher than the best germanium

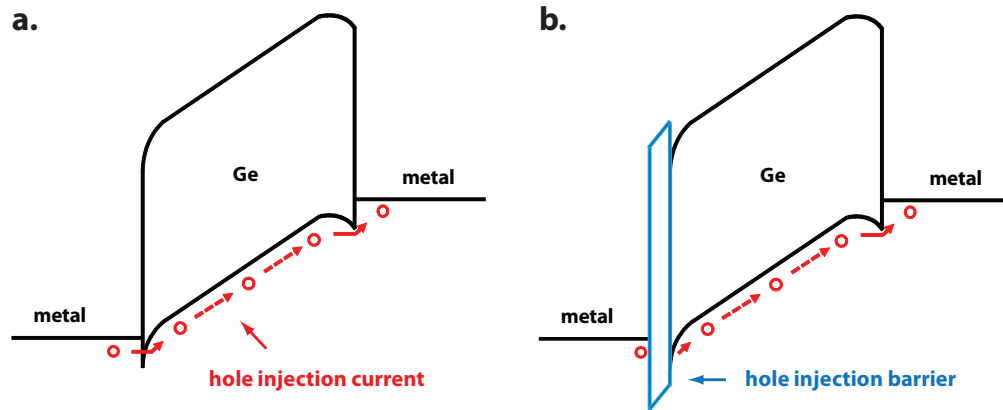


**Figure 3.14.** Origin of the dark current in germanium MSM detectors and approach for reduction. **a.** Schematic of the Fermi level pinning near the valence band edge due to surface states and the formation of hole injection current as a result of thermionic emissions. **b.** Application of a barrier enhancement layer to create a heterojunction with a large barrier for holes to block the hole injection current.

PIN detectors by about one order of magnitude. This is suspected to be primarily coming from thermionic emissions at the metal-germanium interfaces. Germanium presents a very large density of surface states which pins the position of the Fermi energy level near the interface<sup>†</sup>. The pinning has been reported to be at less than 0.1 eV above the valence band edge, which leads to a very low Schottky barrier for holes [100]. As illustrated in Figure 3.14.a, this low barrier leads to enhanced hole injection through the interface and is the predominant source of the relatively high dark current in germanium MSM photodetectors. Weak dependence of dark current on the choice of the contact metal has been reported. However, the amount of dark current is generally much higher than germanium PIN or Si MSM detectors.

<sup>†</sup>This is called Fermi level pinning, where the Fermi level is determined by the charge neutrality level of the surface states and becomes only weakly dependent of the metal work function.

Several techniques can be used to reduce the dark current by engineering the schottky barriers. One approach is introducing very high level n-doping to lift up the Fermi level on the cathode side. The anode interface can also be optionally p-doped, which of course converges to the case of a PIN detector. Another solution is to introduce an extra barrier enhancement layer. As shown in Figure 3.14.b, the principle is to create a heterojunction with a large negative offset in the valance band edge, forming a strong barrier for holes. At the same time, the barrier in the conduction band is small enough for photo-generated electrons accelerated under electrostatic field to pass through. One example of such a barrier enhancement layer is silicon-carbon (Si:C), which creates a barrier height of  $\sim 0.5$  eV and can considerably reduce the hole injection current [101]. Another example is to use a thin amorphous germanium layer as a barrier [102].

### 3.5.2 Speed and bias

The detector performances in both speed and bias do not meet the initial expectations. As pointed out previously, the narrow spacing between the electrodes in the MSM detectors should allow very high speed. The average carrier transit time for an electrode spacing of 750 nm, if assuming all carriers are generated between the two electrodes and are collected under drift process, should be less than 10 ps only. However, preliminary time-domain measurement indicates a much slower response on the order of 100 ps. Also, the detectors show an unexpectedly large bias requirement. As shown in Figure 3.12, the photocurrent does not saturate until with a bias voltage above 2.5 V. If all the carriers are indeed in the gap region between the electrodes, for such a narrow gap the required bias

voltage should be less than 1 V from electrostatic modeling<sup>†</sup>.

Careful simulations of the optical and electrostatic properties of the detector reveal that these deteriorations in the bias requirement and speed are caused by carrier diffusions in the present design. Indeed carriers are generated not only in the gap between the two electrodes, where the electrostatic field is strong and therefore generated carriers can be quickly removed, but also in the taper region and underneath the electrodes, where the electrostatic field is much weaker leading to stronger bias requirement and slower response. This is illustrated in Figure 3.15.a with an SEM image of the germanium pattern for the detector. The brown-shaded regions correspond to the placement of the planar electrodes. The regions with weak electrostatic field are labeled as ①-③. The taper region, labeled as ①, is used initially to reduce the interface reflection. However, as light couples to the taper, it is getting absorbed there as well. Since there are no electrodes covering the taper region, the carriers can not rely on drift process, but instead slow diffusion from the taper to the bulk region and then are collected there. The regions underneath the electrodes, labeled as ② and ③, experience similar problems. As shown in Figure 3.15.b, the electrostatic field there are very weak and mostly oriented vertically which can not drive the carriers for horizontal drift transport. Although from the previous analysis on the optical mode properties of the detector, there should not be any appreciable portion of light in these regions. However, a portion of light indeed enters these region as a result of strong optical diffraction at the electrode entrance (similar to the diffraction phenomenon at a slit aperture). Carriers generated in these regions also have to diffuse back to gap region and get collected. These

---

<sup>†</sup>With 1 V bias, the electrostatic field inside the gap should be strong enough to almost saturate the drift velocities of the carriers, and therefore should be sufficient to remove all the carriers.

un-depleted regions (regions with weak or no electrostatic field) slow down the detector speed and also require stronger bias. However, since the collection time of these carriers is still much faster than the carrier lifetime (a few hundred picosecond), high efficiency can still be achieved with strong enough bias.

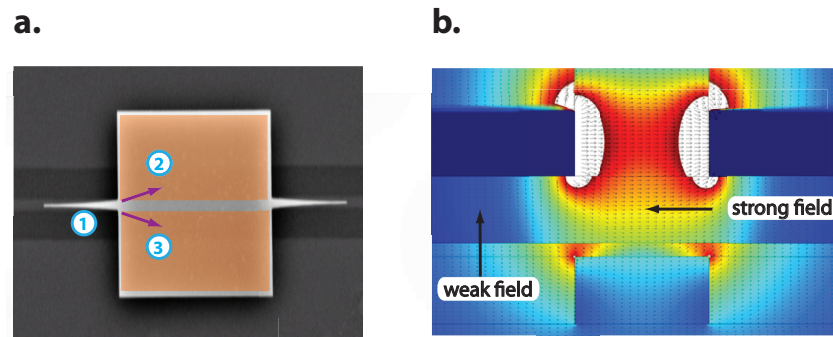


**Figure 3.15.** Problem of carrier diffusion in un-depleted regions in germanium. **a.** Regions with low electrostatic field labeled on a top view SEM image of the germanium pattern. The arrows illustrate optical diffraction at the electrode entrance. **b.** Distribution of electrostatic field in the detector cross-section showing the weak field region underneath the electrodes.

The deteriorations in bias and speed therefore can be resolved by avoiding these un-depleted regions using modified geometry. For example, the tapers can be eliminated, and one can instead increase the thickness of the intermediate  $\text{SiO}_2$  layer and waveguide width to reduce the back-reflection if better than -20 dB is desired. The width of the germanium can be reduced significantly to reduce the area underneath the electrodes. Also, the widths of the silicon waveguide and germanium can be rearranged to eliminate the diffraction effect. In fact, these modifications are adopted in the improved design shown in the next chapter. With these changes the required bias voltage for saturated efficiency is only  $\sim 0.5$  V and a response as short as 8.8 ps is measured.

## CHAPTER 4

### INTEGRATED SILICON WAVELENGTH DIVISION DEMULTIPLEXER WITH 40 GHZ GERMANIUM PHOTODETECTORS

Bandwidth is the primary motivation for resorting to optical interconnects for on-chip communications. To meet the demand of tera-bit per second (Tbps) bandwidth, however, photodetectors with very fast speed, and more importantly, their integration with the wavelength division multiplexing (WDM) technology are necessary. In the previous chapter we demonstrate a novel technique for integrating high quality germanium onto silicon photonic circuits from a low temperature process compatible with the back-end integration scheme. And we demonstrate waveguide integrated detectors with very good performances in efficiency and dark current. The performance in speed, however, does not meet the expectation and it is suspected to be caused by the slow carrier diffusion in that design. In this chapter, we present the improved detector design and demonstrate an impulse response as short as 8.8 ps, which is to the best of our knowledge the fastest integrated germanium detector. With these ultra-fast detectors, we also demonstrate a highly scalable, monolithically integrated WDM detection system that can potentially provide Tbps bandwidth with a very small footprint on-chip.

## 4.1 Design, fabrication, and characterizations of the ultrafast detectors

### 4.1.1 Improved detector design for high speed

As discussed in the previous chapter, the deterioration in the speed in the previous detector design is believed to come from slow carrier diffusion in the non-depleted regions (see Figure 3.15). The carriers generated in or diffused into these regions will take a relatively long time to be collected by the electrodes, as they rely on thermal motions driven the gradient of carrier concentration instead of directional motions driven by the Coulomb forces. The solution is to eliminate these non-depleted regions as much as possible.

In this new design, we first eliminate the tapers but adjust other dimensions to further reduce the interface back-reflection. We slightly increase the thickness of the SiO<sub>2</sub> intermediate layer between germanium and silicon from 40 nm to 80 nm. Since an even smaller portion of the optical mode in the silicon waveguide would see the interfaces with germanium, the back-reflection can be much lower than -20 dB. Although this increase in SiO<sub>2</sub> thickness also reduces the optical coupling between the germanium and silicon, the coupling length is still only a few micrometers and for a sufficiently long detector (30  $\mu\text{m}$ ), the light can be still completely absorbed and thus does not adversely affect the detector efficiency.

We also increase the width of the silicon waveguide underneath and considerably reduce the width of the germanium. The germanium width is changed from  $\sim 9 \mu\text{m}$  in the previous design to  $\sim 1.5 \mu\text{m}$  in the new design, and the

width of the electrodes is changed from  $\sim 4 \mu\text{m}$  to only 350 nm. This greatly reduces the area underneath the electrodes where the electrostatic field is weak. We also avoid the diffraction problem observed in the previous design by adjusting the silicon waveguide to be slightly wider than the germanium. As light now couples from a wider mode to a slightly narrower region (opposite to the previous case), diffraction is no longer induced. This is confirmed with FDTD simulations.

The improved design incorporating these changes is shown in the bottom panel in Figure 4.1, in comparison with the previous design in the top panel. Both designs are based on the vertical GeOI-SOI layered structure and the planar MSM configuration for transverse-electric (TE) polarization. From the cross-section schematics in Figure 4.1.a and b one can see the obvious changes in the width of silicon, germanium, and the electrodes. Also, the thickness of the thin  $\text{SiO}_2$  layer between germanium and silicon is increased from 40 nm to 80 nm. In the new design, the germanium cross-section is  $1.5 \mu\text{m} \times 0.26 \mu\text{m}$ , and the silicon waveguide is  $1.8 \mu\text{m} \times 0.26 \mu\text{m}$ . The planar electrodes are 0.35  $\mu\text{m}$  wide with a spacing of 0.6  $\mu\text{m}$ . Figure 4.1.c and d also compare SEM images of the detector interfaces for both designs. One can see that in the new design the germanium taper is eliminated. These changes, as discussed above, would avoid the slow carrier diffusion process that limits the detector speed.

We also analyzed the optical and electrical properties of the new detector design. Figure 4.2.a plots the optical energy distribution of the fundamental TE mode in the detector region. The mode profile is very similar to that of the previous design, confirming that the new design still offers the good optical confinement in the gap between the electrodes. Figure 4.2.b shows the electro-

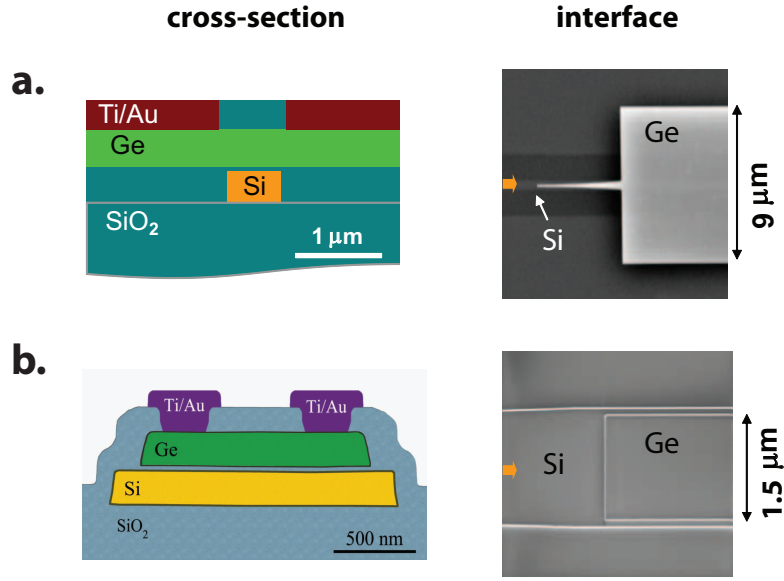


**Figure 4.1.** Comparison of the previous and the new detector design. **a-b.** Cross-sectional schematic of the old and the new designs. **c-d** Top view SEM images of the detector interfaces for the old and the new designs.

static field distribution of the detector with an external bias of 1 V applied. The strength of the field is shown in the color map which is intentionally saturated to the level of  $10^6$  V/m<sup>†</sup>, and the directions of the field is indicated by the cones. Strong electrostatic field with strength over  $10^6$  V/m is observed over almost the entire gap region where most of the light is confined (see Figure 4.2.a). Such good spatial overlap of optical mode and electrostatic field enables efficient and fast removal of carriers generated there. The electrostatic field partially extends to regions underneath the electrodes as well, with only the narrow edges being un-depleted. Based on drift process, the average transit time for both carriers can be as short as 7 ps for an electrode spacing of 600 nm. We calculate the detector capacitance using finite-element electrostatic modeling. For a 30 μm long

<sup>†</sup>The drift velocity of electrons in germanium saturates at  $\sim 6 \times 10^6$  cm/s with electrical field of  $5 \times 10^5$  V/m, and holes reach 90% of its saturated velocity of the same value at electrical field of  $1 \times 10^6$  V/m [103].

detector, the capacitance of the detector is calculated to be as low as 2.4 fF. As discussed before, this ultra-low capacitance allows a load resistance up to 1 k $\Omega$  for detector speed up to 60 GHz, which leads to a higher sensitivity and relaxed requirements on detector amplifiers and can reduce both optical and electrical power consumptions of the receiver [104].

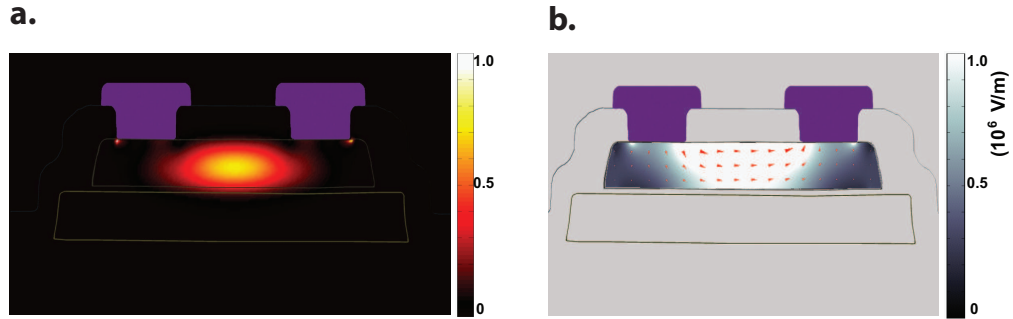


**Figure 4.2.** Optical and electrical properties of the new detector design. **a.** Optical energy distribution of the fundamental TE mode in the detector region. **b.** Distribution of the electrostatic field in the detector with an external bias of 1 V. The color map and cones correspond to the strength and directions of the field, respectively.

#### 4.1.2 Fabrication and DC test

We fabricate the new detectors with slightly modified processes. Similar wafer bonding and ion-assisted layer cutting technique is used to obtain high quality crystalline germanium on silicon. And this is performed with a virgin SOI wafer covered with a SiO<sub>2</sub> layer and an implanted germanium wafer, prior to any patterning. As discussed in the previous chapter, this avoids the critical CMP step used to planarize the patterned silicon layer, and enables fine control of the thickness and uniformity of the intermediate SiO<sub>2</sub> layer. Once we obtain the

GeOI-SOI wafer, standard monolithic CMOS processes are used to define the detectors and the silicon layer.

The process flow can be simply described as follows. We first prepare a standard 4-inch SOI wafer (with 260 nm silicon and 3  $\mu\text{m}$  buried oxide) covered with 80 nm  $\text{SiO}_2$ , and a 4-inch germanium wafer implanted with  $\text{H}^+$  ions (dose  $4 \times 10^{16} \text{ cm}^{-2}$  at 80 KeV). After wafer bonding and layer splitting, the transferred germanium film is chemical mechanical polished down to 260 nm, resulting a 4-inch GeOI-SOI wafer free of any pattern. Electron-beam lithography and reactive ion etching are then used repeatedly to define the germanium detectors, silicon waveguides, and detector vias, followed by evaporation and lift-off of the Ti/Au electrodes. Details regarding the bonding and lithography processes can be found in the Appendix and the previous chapter, respectively.

The dark current was expected to be even lower than the previous design ( $\sim 100 \text{ nA}$  at up to 4 V) due to the reduction in the contact area and correspondingly the interfaces through which thermionic emission occur. However, as a result of the accidental plasma damage of the germanium surface during the via etch step, the fabricated detectors show a dark current of  $\sim 500 \text{ nA}$  under 1V bias, which is a few times larger instead. With improved process control, a much lower dark current on the order of few tens of nano-amperes under 1V bias should be achievable.

We first measure the bias dependence of the photocurrent in the new design and compare it with that of the previous one. The results are plotted in Figure 4.3. The photocurrent in the new detector saturates with a bias voltage as little as 0.5 V, and shows a flat response with higher voltage. This is in sharp contrast to the response of the previous detector, which requires a bias voltage of almost

3 V to saturate the photocurrent. As discussed in the previous chapter, the large bias requirement is attributed to the non-depleted regions in the old design. The result in Figure 4.3 thus strongly suggests the successful elimination of these non-depleted regions.

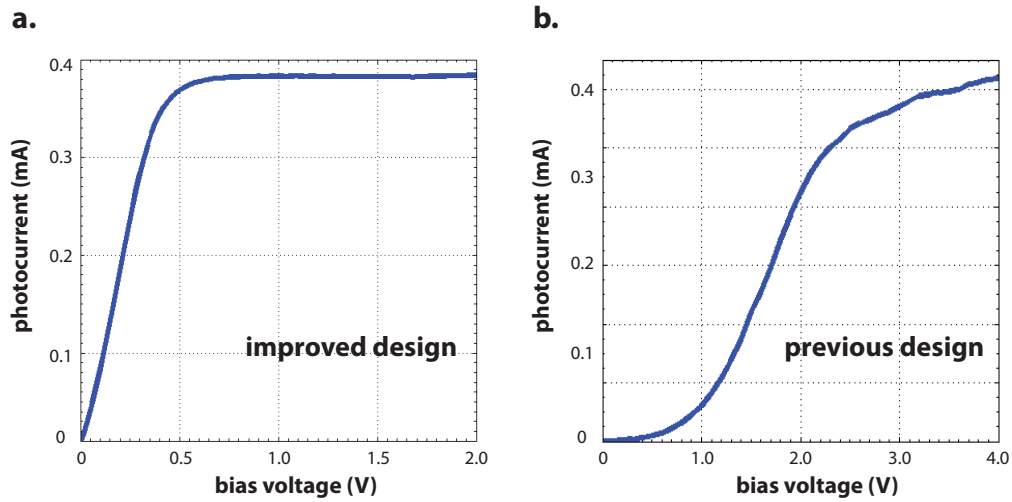


**Figure 4.3.** Comparison of the bias dependence of the photocurrent in both devices. **a.** The improved design **b.** The previous design.

### 4.1.3 Characterization of impulse response

With the confidence that the slow carrier diffusion problem is resolved in the new device, we now measure its temporal response to a short optical pulse (impulse response). The experiment setup is shown in Figure 4.4. A mode-locked fiber laser with center wavelength at 1550 nm is used to generate the short pulse with approximately 1 ps duration at a repetition rate of 25 MHz. The signal is first sent through a fiber polarization controller to obtain the TE polarization, and then injected to the silicon waveguide through a tapered lens fiber and a silicon nano-taper to increase the coupling efficiency [73]. The germanium de-

detector at the end of the waveguide is approached with a dual-tip RF probe. A bias tee is used to supply the detector with a DC bias voltage from a sourcemeter and the AC electrical signal from the detector is then sent to a fast sampling oscilloscope. The mode-locking signal from the mode locked laser is sent to the oscilloscope as a trigger. For this measurement, the measurement apparatus has a minimal bandwidth above 60 GHz. The specified rise time of the bias tee and the electrical sampler are  $\leq 3$  ps and 3.4 ps, respectively. On the oscilloscope, the response is averaged 25 times to reduce the sampler noise due to the lack of any amplifiers for the detector output. Other than that, the responses are all directly recorded on the oscilloscope and no deconvolution is performed to factor out the response due to the measurement apparatus.

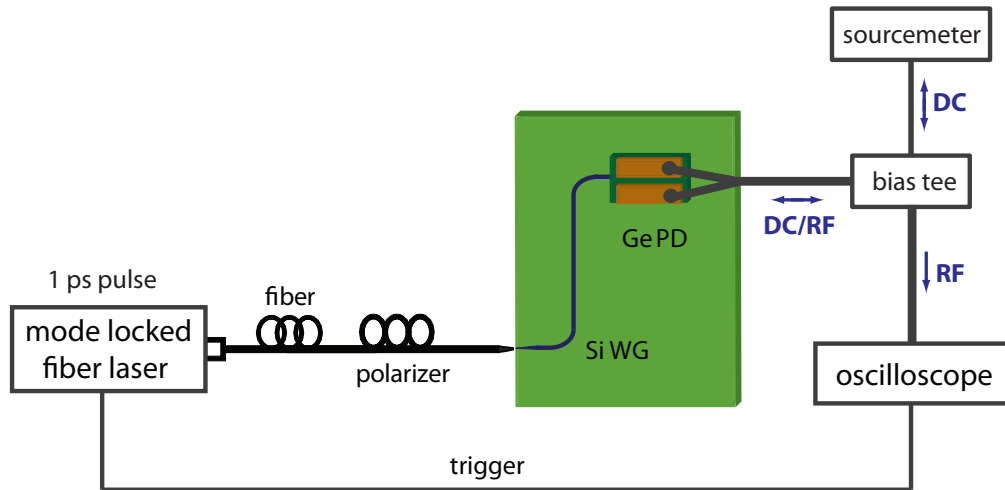


**Figure 4.4.** Measurement setup for characterizing the impulse response of the integrated germanium detector.

We measure an impulse response as short as 8.8 ps, which to the best of our knowledge is the fastest integrated germanium detector reported. The result is shown in Figure 4.5 for a bias voltage of 5 V. Note that no deconvolution is performed to factor out the response due to the measurement apparatus, suggesting that the intrinsic response of the detector should be slightly faster than

the value value directly measured. The observed fast response is a direct result of the three factors in the detector design: the very short carrier drift time across the narrow gap between the electrodes, the avoidance of the slower carrier diffusion process, and the very small RC delay time associated with the ultra-small detector capacitance. This pulse width ideally corresponds to a bandwidth of about 51 GHz, based on the relation of  $f_{3dB} = 0.45/\tau_{FWHM}$ , where  $\tau_{FWHM}$  is the full-width at half-maximum (FWHM) response time [105].

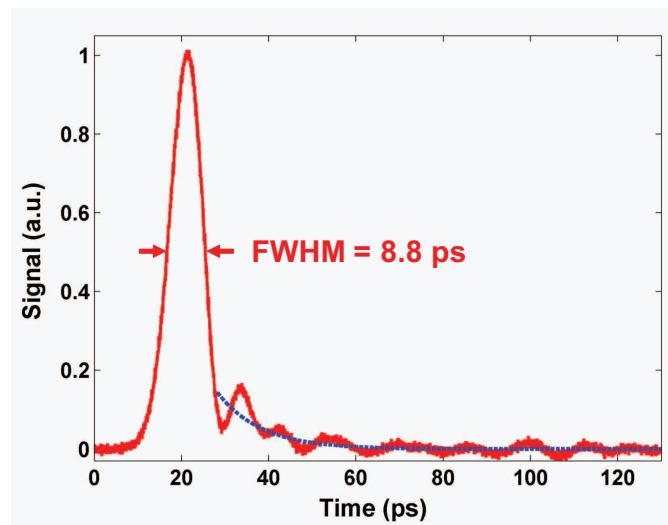


**Figure 4.5.** Directly recorded temporal response of the germanium detector to a picosecond optical pulse.

We analyze the frequency response of the detector through Fourier transform of the impulse response. Figure 4.6 shows the result obtained from fast Fourier transform (FFT) of the impulse response with a recording time of 250 ps. A 3-dB bandwidth of approximately 40 GHz is indicated here by the dashed line. This is lower than the bandwidth estimated from the pulse width (51 GHz) due to the presence of a small tail after the primary pulse in the temporal response. This tail, as indicated by the blue dashed line in Figure 4.5, is modulated by electrical reflections due to impedance mismatch and has a decaying time of

$\sim 10$  ps and roughly 15% of the total pulse energy. We believe this is caused by the fact that the germanium in the improved design is still not completely depleted. As shown in Figure 4.2, the electrostatic field near the edges of the detector and underneath the electrodes is still very weak. So a small amount of carriers generated or diffused there rely partly on slower diffusion to be collected. Between the electrodes where most of the light is confined, the carriers can be removed very quickly because of acceleration in strong electrostatic field. In fact, the primary pulse width is already less than 10 ps with a bias of only 1 V. The tail, however, has a strong dependence on the bias voltage, indicating that it is originating from regions with much weaker field. For example, the decaying time of the tail drops from 42 ps under 1 V bias to 17 ps under 3 V bias. Since the width of these non-depleted regions is very small in the improved design, a very large bandwidth is still achieved.

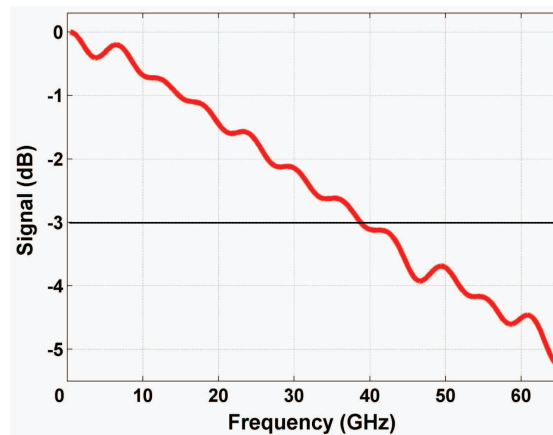


**Figure 4.6.** Frequency response of the detector from fast Fourier transform of its impulse response.

#### 4.1.4 Characterization of 40 Gbps data detection

To confirm its capability of detecting optical signals carrying large bandwidth data, we also measured the detector response to an intensity modulated non-return-to-zero (NRZ) signal at data rate of up to 40 Gbps. The setup is similar to the one used for impulse response characterization (Figure 4.4), except that the mode-locked fiber laser that generates the short pulses now is replaced by a setup to generate the 40 Gbps data. That part is shown in Figure 4.7. The NRZ optical signals are generated by externally modulating a continuous wave laser with a LiNbO<sub>3</sub> optical intensity modulator. The electrical signals driving the modulator, however, due to the lack of instrument for generating digital patterns at such high data rate, are obtained by time-multiplexing lower data rate signals. As shown in Figure 4.7, we use a digital pattern generator with four channel outputs at a data rate of 10 Gbps per channel. The four outputs are fine tuned and sent to a time domain four-channel multiplexer. One of the two clock outputs from the pattern generator (10 GHz) is frequency doubled to 20 GHz, and then amplified and feeded into the multiplexer as a clock signal. Using this clock signal, the multiplexer multiplexes the four channel data in the time domain and generates an output signal at an effective data rate of 40 Gbps. This signal is then amplified again to drive the LiNbO<sub>3</sub> optical intensity modulator. The other clock signal from the pattern generator (10 GHz) is sent to the oscilloscope that records the detector response as a trigger. Different than the previous impulse response characterization, the bias tee used in this particular measurement has a specified rise time of 7 ps and bandwidth of 50 GHz.

Careful tuning of the parameters to each of these instruments are performed to obtain clean optical input signal at 40 Gbps. First, tuning of the four-channel

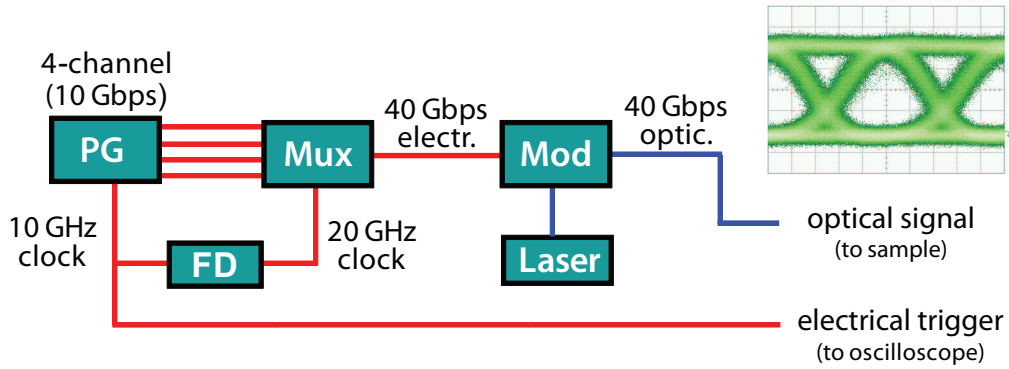


**Figure 4.7.** Setup for generating 40 Gbps NRZ optical signal to characterize the detector response at high data rate. PG - pattern generator; FD - frequency doubler; Mux - time-domain multiplexer; Mod - optical intensity modulator. The right inset shows an eye diagram of the generated 40 Gbps signal measured with a commercial ultrafast detector.

pattern generator and the multiplexer is done to obtain clean electrical signal at 40 Gbps. This includes adjustment to the voltage, offset, delay of four signal channels and the clock delay of the multiplexer. Second, parameters for the LiNbO<sub>3</sub> modulator, such as the polarization of the optical input, the DC voltage offset and the amplitude of the amplified 40 Gbps electrical input are adjusted to obtain clean optical signal with optimized extinction ratio. An example of the generated 40 Gbps optical signal measured with a commercial ultrafast detector is shown in the inset of Figure 4.7.

The recorded temporal response of the detector to the 40 Gbps optical NRZ data under a 4 V bias is shown in Figure 4.8. Despite some small pattern dependence between isolated "0" and consecutive "0", clean detection of the digit pattern is observed here. This confirms that this detector can indeed serve in 40 Gbps interconnect systems. As the detector electrical signal is very weak due to the lack of amplifiers, we are unable to obtain a clean eye diagram. The tempo-

ral response is averaged five times using pattern lock feature of the oscilloscope to reduce the noise of the electrical sampler.

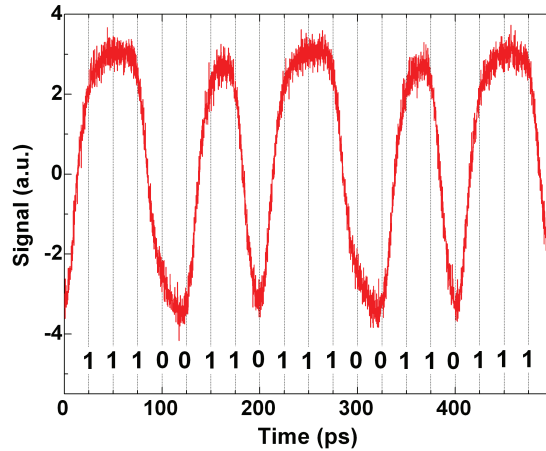


**Figure 4.8.** Detector response to an intensity-modulated NRZ optical signal at 40 Gbps.

#### 4.1.5 Discussion

The detector with the new design demonstrate dramatic performance enhancement compared to that of the previous design. Based on the findings from the previous detector, we realize the problems in speed and strong bias requirement and identify their source as the slow carrier diffusion in the non-depleted regions in that design. We revise the design accordingly with the assist of both optical and electrical modeling. We also redesign the fabrication process to improve allow better control and more importantly, eventual monolithic integration of detectors with other photonic components. With the new device, we demonstrate a directly recorded impulse response of 8.8 ps (without any deconvolution to factor out the response due to the measurement apparatus), which is the fastest integrated germanium detector reported up to the best of our knowl-

edge. We also demonstrate clean operation of the detector with NRZ optical signal at data rate as high as 40 Gbps.

The impulse response pulse width indicates a bandwidth of 51 GHz should be obtained, while the frequency response based on the Fourier transform of the impulse response is limited to approximately 40 GHz because of the small tail. The tail is believed to come from the very small non-depleted region near the edges of the detector. The problem is in fact very general to detectors based on MSM configuration, where the electrostatic field is often not homogeneously distributed and there are regions with only weak field. For example, even within the gap between the electrodes, as one can see from Figure 4.2, there is an obvious dependence of the electrostatic field on the thickness of germanium.

Several techniques can be used to achieve that goal. One solution is to introduce heavy doping near the narrow edges of the germanium, effectively forming a PIN-based detector. As illustrated in Figure 4.9.a, This will create a homogeneous field over the entire intrinsic region in the center. Also, the built-in potential can be utilized to further reduce the required bias voltage. The doped region can be kept very narrow to avoid degrading the detector efficiency. Another option is to introduce electrical contacts on the side edges of germanium (see Figure 4.9.b). This again creates very uniform electrostatic field inside the germanium, similar to the field in a parallel-plate capacitor. The calculated distribution is shown in Figure 4.9.c. One can see the field uniformity is greatly improved compared to Figure 4.2. Out of these two options the first PIN-based approach is more advantageous in two aspects. Firstly, it has smaller optical mode overlap with the metal electrodes, which implies slightly higher efficiency. Secondly, its metal-germanium contact interfaces form at the smooth top surface

of germanium, while in the other case they form at the etched sidewalls which might lead to larger dark current. However, either approach should lead to the complete elimination of the non-depleted regions and remove the tail signal, enabling bandwidth as high as 50 GHz with a bias voltage as low as 1 V only.

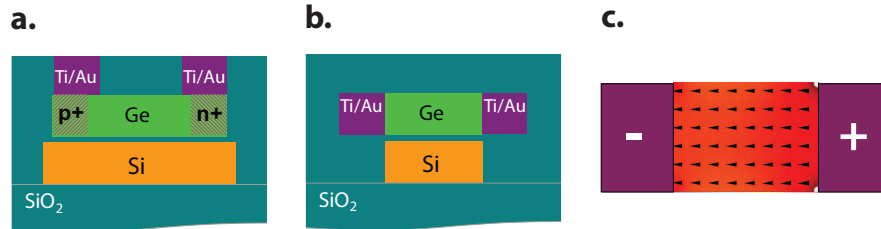


**Figure 4.9.** Designs of detectors to completely eliminate any non-depleted regions in germanium. **a.** A PIN-based detector with heavy doping near the narrow edges of germanium. **b.** A MSM-based detector with electrodes forming at the sidewalls of germanium. **c.** The distribution of electrostatic field in germanium for the design shown in **b.**

## 4.2 Design and characterizations of integrated WDM detection systems

### 4.2.1 Basics of WDM detection systems

As discussed in chapter 1, optical interconnects with WDM technology greatly expand the bandwidth density and are crucial in meeting the bandwidth demand for on-chip communications. Figure 4.10 illustrates a schematic of a simplified WDM detection system. Here the incoming light contains multiple signals each centered at different wavelengths. After passing through the demultiplexed, all signals are separated according to their wavelengths, and are sent

to an array of photodetectors where the signals are retrieved. In telecommunications, the demultiplexers and detector arrays are typically separate chips packaged together. For on-chip optical interconnects, however, these functionalities have to be integrated together with other optical components on the same chip.

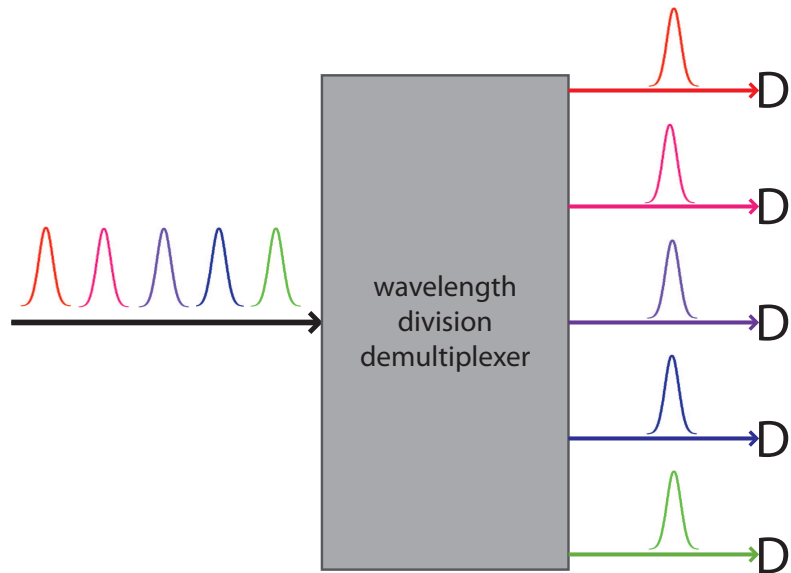


**Figure 4.10.** Schematic of a simplified WDM detection system.

There are two primary configurations of demultiplexer architectures. The first one is parallel signal processing, where signals of several different wavelengths are separated simultaneously within a single device. Examples include free-space diffraction gratings and integrated planar devices such as planar concave gratings and arrayed waveguide gratings (AWG) that utilize the same principle, i.e., spatial interference of optical waves coming through many different optical paths [106, 107]. The second one is series signal processing, where signals are separated individually using cascaded filtering devices. Examples include demultiplexers based on thin-film filters or fiber Bragg grating filters and circulators [108, 109]. In planar photonic circuits this can be achieved simply

with cascaded resonators [110]. Unlike the grating-based parallel scheme, this approach allows control of individual channels, such as their wavelengths and bandwidths. For photonic circuits based on high index contrast platforms such as silicon, this is an important advantage since any deviation from designed targets induced by unavoidable fabrication variations can be easily compensated. In the parallel scheme, in contrary, these properties are linked to the entire devices and the complexity of compensation grows rapidly as the number of channels increases.

#### **4.2.2 WDM demultiplexer based on cascaded ring resonators**

We design an integrated WDM detection system using cascaded silicon ring resonators [111] and the ultrafast germanium detectors. Figure 4.11 shows a schematic of such a system. A group of optical signals at various wavelength channels propagates along a silicon bus waveguide, which couples to a series of ring resonators in the typical add-drop configuration. Each resonator picks up one wavelength channel that matches its resonance condition and delivers that channel to the detector at its drop port, while leaving all other wavelength channels intact on the bus waveguide. As a result of the individual processing of each channel, their properties can be independently adjusted without interfering any other channels.

The optical response of a single ring resonator – as a unit cell of the demultiplexer – can be controlled with the dimensions of the resonator and the amount of coupling. The resonant wavelength of each resonator can be adjusted with its radius to match a specific signal channel. The resonance wavelength ( $\lambda_r$ ), de-

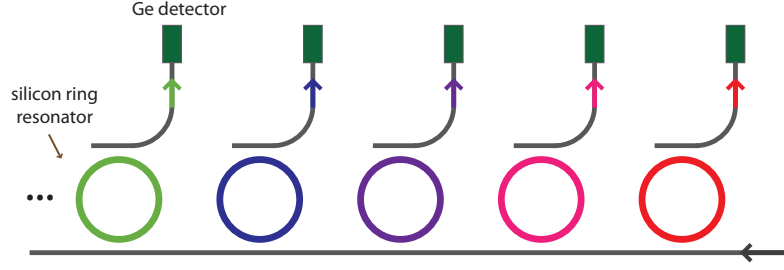


**Figure 4.11.** Schematic of an integrated WDM detection system based on cascaded silicon ring resonators and germanium photodetectors.

terminated by the round-trip phase accumulation, can be approximately written as<sup>†</sup>

$$\lambda_r \approx \frac{n_e(\lambda)2\pi R}{m}, \quad (4.1)$$

where  $n_e(\lambda)$  is the effective index in the ring resonator as a function of wavelength,  $R$  is the radius of the ring,  $m$  is the resonance order. For another wavelength different by the channel spacing  $\Delta\lambda$ , the corresponding change in radius  $\Delta R$  is determined by

$$\lambda_r + \Delta\lambda \approx \frac{n_e(\lambda_r + \Delta\lambda)2\pi(R + \Delta R)}{m}. \quad (4.2)$$

After simple algebra and first-order approximation, one can get

$$\frac{\Delta R}{R} \approx \frac{n_g(\lambda_r)}{n_e(\lambda_r)} \cdot \frac{\Delta\lambda}{\lambda_r}. \quad (4.3)$$

where  $n_g(\lambda)$  is the group index of the optical mode in the ring, defined as  $n_g(\lambda) = n_e(\lambda) - \lambda \frac{dn_e(\lambda)}{d\lambda}$ . Assuming the parameters typical for silicon ring resonators near 1550 nm:  $n_e \approx 2.5$ ,  $n_g \approx 4.2$ ,  $R \approx 10 \mu\text{m}$ , one can calculate that for a channel spacing of  $\Delta\lambda \sim 1 \text{ nm}$ , the required change in radius is  $\Delta R \sim 11 \text{ nm}$ .

Another important parameter in using resonators in demultiplexers is its free spectral range (FSR,  $\lambda_{FSR}$ ). This is defined as the spacing between two

<sup>†</sup>This neglects any phase perturbation induced by the coupling waveguides, which in practical case does cause phase change and shift in the resonance wavelength.

neighboring resonances of the same resonator, and therefore limits the spectral range one can use if only one level of demultiplexer is deployed. Similarly,

$$\lambda_r + \lambda_{FSR} \approx \frac{n_g(\lambda_r + \lambda_{FSR})2\pi R}{m - 1}. \quad (4.4)$$

From this one can get

$$\lambda_{FSR} \approx \frac{\lambda_r^2}{n_g(\lambda_r)2\pi R}. \quad (4.5)$$

For the parameters used above, a FSR of  $\sim 9$  nm is expected. This thus can accommodate up to 8 channels with a channel spacing of 1 nm.

The optical bandwidth of the resonator affects the amount of signal bandwidth the resonator can process and the cross-talk between neighboring wavelength channels. As shown in chapter 2, the bandwidth can be simply written as

$$\delta\lambda \approx \frac{\lambda_r^2}{4\pi^2 n_g(\lambda_r)R}(\alpha + \kappa_1 + \kappa_2), \quad (4.6)$$

where the  $\kappa_1$  and  $\kappa_2$  are the power coupling from the ring to the input and output waveguides, and  $\alpha$  is the power loss per round-trip. To estimate the amount of cross-talk, we assume that the signal bandwidth is the same as the optical resonance bandwidth and that the drop port transmission is a Lorentz function centered at  $\lambda_r$  (see Figure 4.12.a):

$$f(\lambda) = \frac{1}{1 + \left(\frac{\lambda - \lambda_r}{\delta\lambda/2}\right)^2}. \quad (4.7)$$

Therefore, the cross-talk – the signal it picks up from the next channel centered at  $\lambda_r + \Delta\lambda$  – can be simply written as

$$f(\lambda_r + \Delta\lambda - \delta\lambda/2) = \frac{1}{1 + \left(\frac{\Delta\lambda - \delta\lambda/2}{\delta\lambda/2}\right)^2}. \quad (4.8)$$

Assuming a tolerable cross-talk level of less than -10 dB for example, one requires  $\delta\lambda \leq 0.5 \Delta\lambda$ . For a channel spacing  $\Delta\lambda = 1$  nm, the maximum allow-

able resonance bandwidth is therefore 0.5 nm, which corresponds to a bandwidth over 60 GHz in frequency. For a requirement of -20 dB, this changes to  $\delta\lambda \leq 0.18 \Delta\lambda$ , and a channel spacing of 1 nm requires the resonance bandwidth to be less than 0.18 nm or 22 GHz.

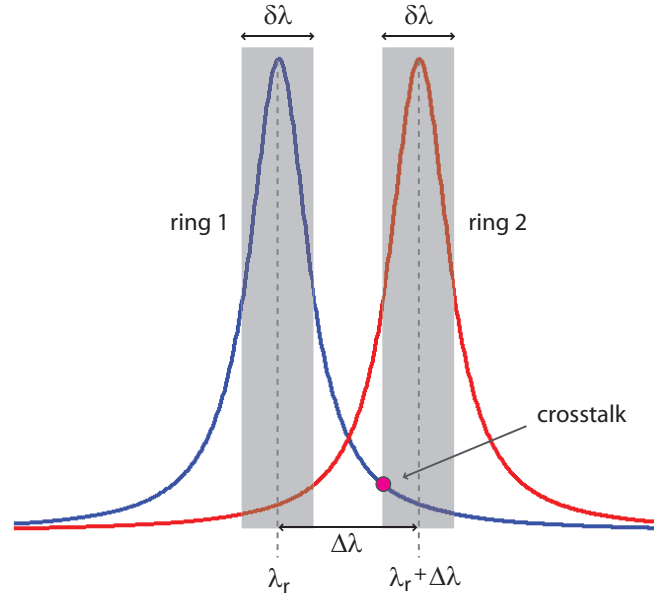


**Figure 4.12.** Illustration of optical crosstalk between neighboring channels in cascaded ring resonators.

Another important characterization of the resonator is its drop efficiency, i.e., the efficiency of transferring the desired signal channel from the bus waveguide to the drop waveguide. At the resonant condition, the transmission of the through port and the drop port can be simply written as

$$T_t(\lambda_r) \approx \left| \frac{\kappa_1 - \kappa_2 - \alpha}{\kappa_1 + \kappa_2 + \alpha} \right|^2 \quad (4.9)$$

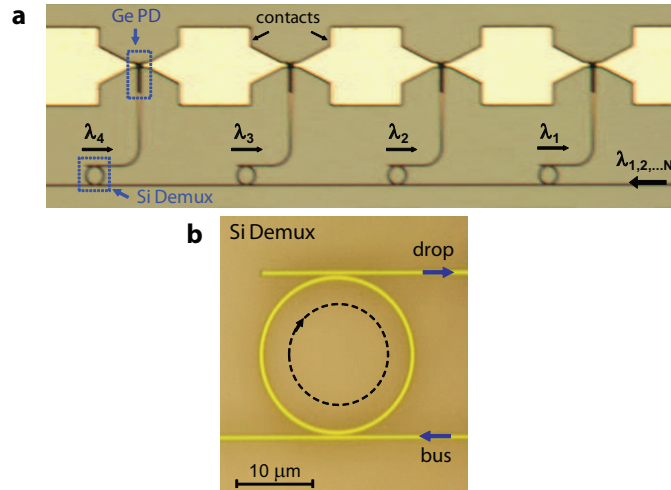
$$T_d(\lambda_r) \approx \frac{4\kappa_1\kappa_2}{|\kappa_1 + \kappa_2 + \alpha|^2} \quad (4.10)$$

Under critical coupling, i.e.  $\kappa_1 - \kappa_2 - \alpha = 0$ , the signal at  $\lambda_r$  can be completely removed from the bus waveguide, part of which goes to the drop port and the rest of which is lost inside the ring. The drop efficiency depends on the relative

strength of the coupling compared with the loss. With strong coupling and small optical loss,  $\kappa_1 \approx \kappa_2 \gg \alpha$ , drop efficiency close to unity can be achieved. However, improving the drop efficiency with too strong coupling leads to larger resonator bandwidth, which can potentially limit the channel spacing and thus the number of channels attainable.

### 4.2.3 Fabrication and measurements

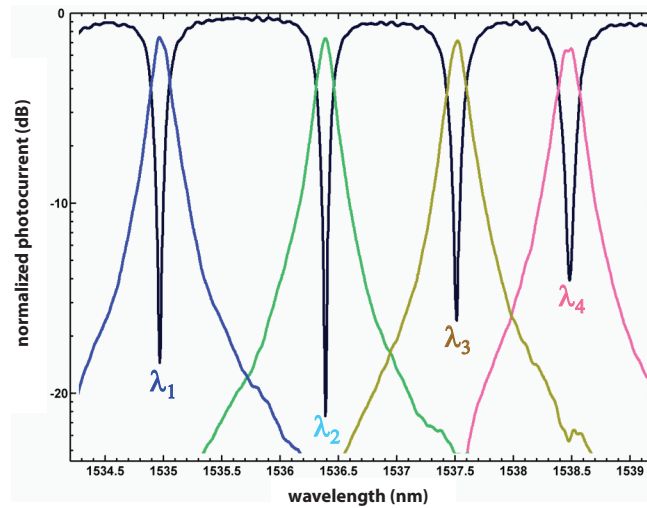
Following the analysis above, we design and fabricate an integrated WDM detection system with four cascaded silicon ring resonators and the ultrafast germanium detectors. The device is fabricated on the GeOI-SOI wafer with the same monolithic processes as the integrated detectors shown in the first section of this chapter. Figure 4.13.a shows optical microscope image of the fabricated device. Note that the contact pads for probing are shared between neighboring detectors simply to reduce lithography time. The silicon ring resonators, as shown in Figure 4.13.b, have radii ( $R$ ) of approximately 10  $\mu\text{m}$ , which is slightly adjusted with a step size of 10 nm ( $\Delta R$ ). From Eqn.4.3 this corresponds to a step in the resonance wavelength ( $\Delta\lambda$ ) of approximately 1 nm. As mentioned above, the FSR ( $\lambda_{FSR}$ ) is approximately 9 nm. The cross-sectional dimensions of the ring resonators are 450 nm  $\times$  260 nm, and that of the bus and drop waveguides are both 400 nm  $\times$  260 nm. The coupling gaps between the ring resonator and the bus and drop waveguides are 100 nm and 110 nm, respectively. The optical bandwidth of the resonators is estimated to be approximately 20 GHz. The cross-talk between neighboring channels therefore should be below -20 dB based on previous estimations. The detectors used are of similar parameters as discussed in the first section of this chapter.



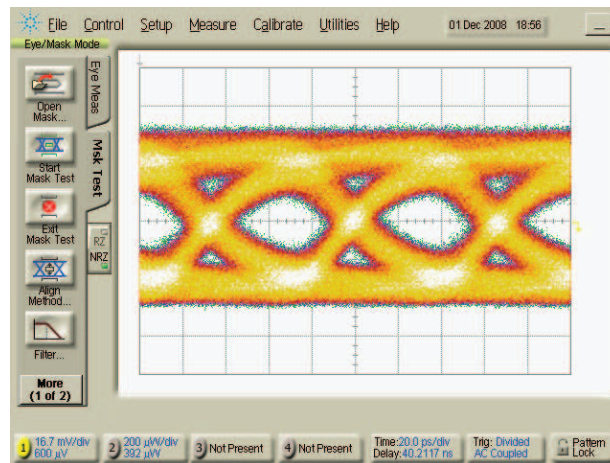
**Figure 4.13.** Integrated detection system composed of silicon microring resonator-based wavelength division demultiplexer and the germanium detectors. **a.** Optical image of the device. **b.** Zoom-in of one microring resonator.

Figure 4.14 shows the measured DC response of the integrated WDM detection system. All the spectra are recorded with the detectors at the end of the bus waveguide (through port) and the four drop-ports. At the through port spectrum, one can see four clean resonances, each coming from one of the ring resonators and having an extinction ratio over 15 dB. From the drop port spectra, clean separation of the four wavelengths is observed here with a crosstalk between adjacent channels as low as -25 dB. Each channel has an optical bandwidth of approximately 0.15 nm (19 GHz) with a channel spacing of roughly 1 nm. The spacing between the first and second channel is larger due to fabrication imperfection. The drop efficiency is around -1 to -2 dB, which can be improved by reducing the propagation loss in the resonators and slightly increasing the optical couplings.

We also test the capability of demultiplexing optical data with such system. Similar to the technique used in characterizing the detector response, we in-



**Figure 4.14.** DC Spectra of the WDM detection system at the through port and the four drop ports measured with integrated detectors.



**Figure 4.15.** Eye diagram of demultiplexed NRZ data at the 4th channel at 15 Gbps.

jected intensity-modulated NRZ optical signal centered at one of the channels into the bus waveguide and measured the response at corresponding drop-port detectors. The electrical signal driving the optical intensity modulator is generated by time-domain multiplexing two signals at lower data rate. Figure 4.15 shows an example of the recorded eye diagram for the 4th channel (1538.5

nm) at 15 Gbps. As there is no amplifier for the detector output signal, only a weak signal level is recorded on the oscilloscope. The slight closing of the eye observed here is due to signal distortion from the resonator due to the non-uniform transmission and dispersion within the passband, and the data rate is limited only by the resonance bandwidth.

#### 4.2.4 Discussion

The 4-channel  $\times$  19 GHz integrated WDM detection system demonstrated here presents an important progress towards on-chip optical interconnect applications in providing sufficient bandwidth for the rapidly growing data communications. The system consists of silicon photonic circuit and fast germanium detectors, and is built with monolithic and standard CMOS process on GeOI-SOI wafers, which are obtained using a low temperature wafer bonding and ion-assisted layer cutting technique.

The demonstrated demultiplexer is highly scalable and can potentially provide Tbps bandwidth as required for optical interconnects. Firstly, the bandwidth of each channel can be considerably increased. The germanium detector should be capable of running at 50 Gbps data rate, as indicated by the directly measured impulse response of 8.8 ps only. The optical bandwidth corresponding to such a data rate is approximately 0.4 nm, which can be obtained by increasing the optical coupling as in Eqn. 4.6. From previous analysis, this still allows a channel spacing of 1 nm with less than -10 dB crosstalk. Higher-order ring resonators [112] can also be used to create resonances with a flat passband, faster roll-off, and low group delay dispersion within the passband, which re-

duce the cross-talk and the signal distortion induced by the resonator in both amplitude and phase.

Secondly, the number of wavelength channels can be greatly increased with a larger FSR. One solution is to use smaller resonators. The resonators we use have a radius of approximately  $10\ \mu\text{m}$  and a FSR of  $\sim 9\ \text{nm}$ , allowing up to 8 channels with  $1\ \text{nm}$  channel spacing. Because of the strong confinement offered by the silicon waveguide, high quality resonators with radius as small as  $1.5\ \mu\text{m}$  have been experimentally demonstrated, which corresponds to a FSR of as large as  $\sim 60\ \text{nm}$  and allow more than 50 channels with  $1\ \text{nm}$  channel spacing [15]. In this case the step size in  $\Delta R$  is calculated to be only  $1.5\ \text{nm}$ , which is within the state of the art fabrication variations. Therefore for accurate control of the resonance wavelength one need to rely on active tuning of the effective index  $n_e(\lambda)$  (see Eqn. 4.1). For example, integrated microheaters similar to the one in chapter 2 can be used.

Another solution is to use the optical Vernier effect with two coupled ring resonators of different sizes [113]. In this scheme, resonances appear only when the resonance wavelengths of both rings coincide, which can give rise to an effective FSR much larger than either of the individual resonators. Figure 4.16 shows an example of two coupled rings of radii of approximately  $3\ \mu\text{m}$  and  $5\ \mu\text{m}$ , respectively, calculated for quasi-TM polarization. The spectra in Figure 4.16.b show a FSR as large as  $90\ \text{nm}$  is obtained. As shown in the inset, the resonance also exhibit a very wide and flat passband, which greatly reduces the distortion induced by the resonator. Some small features are still observed at other resonances of the two rings that do not coincide, but they are very small in the drop port response (less than  $-15\ \text{dB}$ ) and can be further reduced with

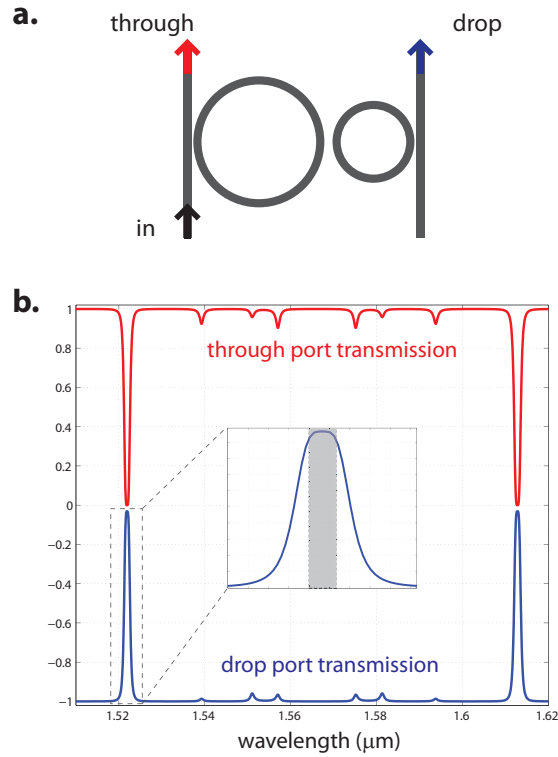


**Figure 4.16.** Optical vernier effect to expand the free spectral range. **a.** Schematic of two coupled ring resonators. **b.** Transmission spectra of the coupled resonators at the through port and drop port. Inset: wide and flat passband of the resonance.

optimized design.

Combining the approaches discussed above to increase both the bandwidth per channel and the number of channels, we can potentially demonstrate a WDM detection system with an aggregated bandwidth up to 2.5 Tbps ( $50 \times 50$  Gbps). The monolithic, CMOS compatible integration approach, combined with the expected low power consumption of the detectors, and the very compact size (a few  $\text{mm}^2$  footprint), should mark a significant progress for building on-chip optical interconnects with over Tbps bandwidth.

## BIBLIOGRAPHY

- [1] D. A. B. Miller and H. M. Ozaktas, "Limit to the bit-rate capacity of electrical interconnects from the aspect ratio of the system architecture," Special Issue on Parallel Computing with Optical Interconnects, *J. Parallel and Distributed Computing* **41**, 42-52 (1997).
- [2] A. Masaki, "Electrical resistance as a limiting factor for high-performance computer packaging," *IEEE Circuits and Devices Magazine* **5**, 22-26 (1989).
- [3] D. A. B. Miller, "Physical reasons for optical interconnection, *Int. J. Optoelectronics* **11**, 155-168 (1997).
- [4] D. A. B. Miller, "Rationale and challenges for optical interconnects to electronic chips," *Proc. IEEE* **88**, 728-749 (2000).
- [5] M. Haurylau, G. Chen, H. Chen, J. Zhang, N. A. Nelson, D. H. Albonesei, E. G. Friedman, and P. M. Fauchet, "On-chip optical interconnect roadmap: challenges and critical directions," *IEEE J. Sel. Top. Quantum Electron.* **12**, 1699-1705 (2006).
- [6] J. A. Kash, "Internal optical interconnects in next generation high-performance servers," invited presentation in Cornell Nanofab Symposium, Cornell University (2006).
- [7] J. A. Kash, F. Doany, D. Kuchta, P. Pepeljugoski, L. Schares, J. Schaub, C. Schow, J. Trehwella, C. Baks, Y. Kwark, C. Schuster, L. Shan, C. Patel, C. Tsang, J. Rosner, F. Libsch, R. Budd, P. Chiniwalla, D. Guckenberger, D. Kucharski, R. Dangel, B. Offrein, M. Tan, G. Trott, D. Lin, A. Tandon,

- and M. Nystrom, "Terabus: A Waveguide-Based Parallel Optical Interconnect," IEEE Lasers and Electro-Optics Society (LEOS) 18th Annual Meeting, 363-364 (2005).
- [8] F. E. Doany, C. L. Schow, C. Baks, R. Budd, Y. J. Chang, P. Pepeljugoski, L. Schares, D. Kuchta, R. John, J. A. Kash, and F. Libsch, "160 Gb/s bidirectional parallel optical transceiver module for board-level interconnects using single-chip CMOS IC," IEEE Proc. Electronic Components and Technology Conference, 1256-1261 (2007).
- [9] R. T. Chen, L. Lin, C. Choi, Y. J. Liu, B. Bihari, L. Wu, S. Tang, R. Wickman, B. Picor, M. K. Hibb-Brenner, J. Bristow, and Y. S. Liu, "Fully embedded board-level guided-wave optoelectronic interconnects," Proc. IEEE **88**, 780-793 (2000).
- [10] G. Chena, H. Chen, M. Haurylaua, N. A. Nelsona, D. H. Albonesic, P. M. Faucheta, and E. G. Friedman, "Predictions of CMOS compatible on-chip optical interconnect," VLSI J. Integration **40**, 434-446 (2007).
- [11] J. D. Jackson, "Classical Electrodynamics," 3rd Edition, Jhon Willey & Sons, New York (1999).
- [12] H. B. G. Casimir and J. Ubbink, "The Skin Effect: II. The Skin Effect at High Frequencies," Philips Technical Review **28**, 300-315 (1967).
- [13] R. J. Essiambre, Capacity limits of fiber-optic communication systems, in Proc. Optical Fiber Communication Conference (OFC) (2009).
- [14] B. G. Lee, X. Chen, A. Biberman, X. Liu, I. Hsieh, C. Chou, J. I. Dadap, F. Xia, W. M. J. Green, L. Sekaric, Y. A. Vlasov, R. M. Osgood, and K.

- Bergman, "Ultra-high-bandwidth silicon photonic nanowire waveguides for on-chip networks," *IEEE Photon. Technol. Lett.* **20**, 398-400 (2008).
- [15] Q. Xu, D. Fattal, and R. G. Beausoleil, "Silicon microring resonators with 1.5  $\mu\text{m}$  radius," *Opt. Express* **16**, 4309-4315 (2008).
- [16] Q. Xu, B. Schmidt, S. Pradhan, and M. Lipson, "Micrometre-scale silicon electro-optic modulator," *Nature* **435**, 325 (2005).
- [17] W. M. J. Green, M. J. Rooks, L. Sekaric, and Y. A. Vlasov, "Ultra-compact, low RF power, 10 Gb/s silicon Mach-Zehnder modulator," *Opt. Express* **15**, 17106-17113 (2007).
- [18] Y. Vlasov, W.M.J. Green, and F. Xia, "High-throughput silicon nanophotonic wavelength-insensitive switch for on-chip optical networks," *Nature Photonics* **2**, 242-246 (2008).
- [19] T. Yin, R. Cohen, M. Morse<sup>1</sup>, G. Sarid, Y. Chetrit, D. Rubin, and M. J. Paniccia, "31 GHz Ge n-i-p waveguide photodetectors on Silicon-on-Insulator substrate," *Opt. Express* **15**, 13965-13971 (2007).
- [20] Q. Lai, W. Hunziker, and H. Melchior, "Low-power compact 22 thermo-optic silica-on-silicon waveguideswitch with fast response," *IEEE Photon. Technol. Lett.* **10**, 681-683 (1998).
- [21] M. W. Geis, S. J. Spector, R. C. Williamson, and T. M. Lyszczarz, "Submicrosecond Submilliwatt Silicon-on-Insulator Thermo-optic Switch," *IEEE Photon. Technol. Lett.* **16**, 2514-2516 (2004).
- [22] S. Pozder, R. Chatterjee, A. Jain, Z. Huang, R. E. Jones, and E. Acosta, "Progress of 3D Integration Technologies and 3D Interconnects," *IEEE International Interconnect Technology Conference*, 213-215 (2007).

- [23] A. Harke, M. Krause, and J. Mueller, "Low-loss singlemode amorphous silicon waveguides," *Electronics Letters* **41**, 1377- 1379 (2005).
- [24] K. Preston, S. Manipatruni, A. Gondarenko, C. B. Poitras, and M. Lipson, "Deposited silicon high-speed integrated electro-optic modulator," *Opt. Express* **17**, 5118-5124 (2009).
- [25] <http://www.luxtera.com>.
- [26] A. Fang, H. Park, O. Cohen, R. Jones, M. Paniccia, and J. Bowers, "Electrically pumped hybrid AlGaInAs-silicon evanescent laser," *Opt. Express* **14**, 9203-9210 (2006).
- [27] L. Pavesi, S. Gaponenko, and L. D. Negro, "Towards the first silicon laser," Springer (2002).
- [28] Q. Xu, S. Manipatruni, B. Schmidt, J. Shakya, and M. Lipson, "12.5 Gbit/s carrier-injection-based silicon micro-ring silicon modulators," *Opt. Express* **15**, 430-436 (2007).
- [29] A. Liu, R. Jones, L. Liao, D. Samara-Rubio, D. Rubin, O. Cohen, R. Nicolaescu, and M. Paniccia, "A high-speed silicon optical modulator based on a metal-oxide-semiconductor capacitor," *Nature* **427**, 615-618 (2004).
- [30] A. Liu, L. Liao, D. Rubin, H. Nguyen, B. Ciftcioglu, Y. Chetrit, N. Izhaky, and M. Paniccia, "High-speed optical modulation based on carrier depletion in a silicon waveguide," *Opt. Express* **15**, 660-668 (2007).
- [31] <http://download.intel.com/pressroom/kits/research>.
- [32] J. Liu, M. Beals, A. Pomerene, S. Bernardis, R. Sun, J. Cheng, L. C. Kimer-

- ling, and J. Michel, "Waveguide-integrated, ultralow-energy GeSi electro-absorption modulators," *Nature Photonics* **2**, 433-437 (2008).
- [33] L. Liu, J. V. Campenhout, G. Roelkens, R. A. Soref, D. V. Thourhout, P. Rojo-Romeo, P. Regreny, C. Seassal, J. Fdli, and R. Baets, "Carrier-injection-based electro-optic modulator on silicon-on-insulator with a heterogeneously integrated III-V microdisk cavity," *Opt. Lett.* **33**, 2518-2520 (2008).
- [34] H. Park, A. W. Fang, R. Jones, O. Cohen, O. Raday, M. Sysak, M. Paniccia, and J. Bowers, "A hybrid AlGaInAs-silicon evanescent waveguide photodetector," *Opt. Express* **15**, 6044-6052 (2007).
- [35] L. Vivien, M. Rouvire, J. Fdli, D. Marris-Morini, J. Damlencourt, J. Mangeney, P. Crozat, L. Melhaoui, E. Cassan, X. Roux, D. Pascal, and S. Laval, "High speed and high responsivity germanium photodetector integrated in a Silicon-On-Insulator microwaveguide," *Opt. Express* **15**, 9843-9848 (2007).
- [36] L. Chen, P. Dong, and M. Lipson, "High performance germanium photodetectors integrated on submicron silicon waveguides by low temperature wafer bonding," *Opt. Express* **16**, 11513-11518 (2008).
- [37] S. Zhu, M. B. Yu, G. Q. Lo, and D. L. Kwong, "Near-infrared waveguide-based nickel silicide Schottky-barrier photodetector for optical communications," *Appl. Phys. Lett.* **92**, 081103 (2008).
- [38] M. W. Geis, S. J. Spector, M. E. Grein, R.T. Schulein, J. U. Yoon, D. M. Lennon, S. Denault, F. Gan, F. X. Kartner, and T. M. Lyszczarz, "CMOS-compatible all-Si high-speed waveguide photodiodes with high respon-

- sivity in near-infrared communication band," *IEEE Photon. Technol. Lett.* **19**, 152-154 (2007).
- [39] M. W. Geis, S. J. Spector, M. E. Grein, J. U. Yoon, D. M. Lennon, and T. M. Lyszczarz, "Silicon waveguide infrared photodiodes with >35 GHz bandwidth and phototransistors with 50 AW<sup>-1</sup> response," *Opt. Express* **17**, 5193-5204 (2009).
- [40] P. Dong, S. F. Preble, and M. Lipson, "All-optical compact silicon comb switch," *Opt. Express* **15**, 9600-9605 (2007).
- [41] N. Sherwood-Droz, H. Wang, L. Chen, B. G. Lee, A. Biberman, K. Bergman, and M. Lipson, "Optical 4x4 hitless silicon router for optical networks-on-chip (NoC)," *Opt. Express* **16**, 15915-15922 (2008).
- [42] N. Han-Yong, R. W. Michael, L. Daqun, W. Xuan, M. Jose, R. P. Roberto, and P. Kachesh, "4 x 4 wavelength-reconfigurable photonic switch based on thermally tuned silicon microring resonators," *Opt. Eng.* **47**, 044601 (2008).
- [43] F. Xia, L. Sekaric, and Y. Vlasov, "Ultracompact optical buffers on a silicon chip," *Nature Photonics* **1**, 65-71 (2006).
- [44] Q. Xu, P. Dong, and M. Lipson, "Breaking the delay-bandwidth limit in a photonic structure," *Nature Physics* **3**, 406-410 (2007).
- [45] T. Barwicz, M. R. Watts, M. A. Popovic, P. T. Rakich, L. Socci, F. X. Kartner, E. P. Ippen and H. I. Smith, "Polarization-transparent microphotonic devices in the strong confinement limit," *Nature Photonics* **1**, 57-60 (2006).
- [46] K. K. Lee, D. R. Lim, L. C. Kimerling, J. Shin, and F. Cerrina, "Fabrication

- of ultralow-loss Si/SiO<sub>2</sub> waveguides by roughness reduction," *Opt. Lett.* **26**, 1888-1890 (2001).
- [47] Y. Vlasov and S. McNab, "Losses in single-mode silicon-on-insulator strip waveguides and bends," *Opt. Express* **12**, 1622-1631 (2004).
- [48] J. Cardenas, C. B. Poitras, J. T. Robinson, K. Preston, L. Chen, and M. Lipson, "Low loss etchless silicon photonic waveguides," *Opt. Express* **17**, 4752-4757 (2009).
- [49] L. Chen, N. Sherwood-Droz, and M. Lipson, "Compact bandwidth-tunable microring resonators," *Opt. Lett.* **32**, 3361-3363 (2007).
- [50] L. Chen and M. Lipson, "Ultra-low capacitance and high speed germanium photodetectors on silicon," *Opt. Express* **17**, 7901-7906 (2009).
- [51] K. J. Vahala, "Optical microcavities," *Nature* **424**, 839 (2003).
- [52] M. Pelton, C. Santori, J. Vuckovic, B. Zhang, G. S. Solomon, J. Plant, and Y. Yamamoto, "Efficient source of single photons: a single quantum dot in a micropost microcavity," *Phys. Rev. Lett.* **89**, 233602 (2002)
- [53] S. Reitzenstein, A. Bazhenov, A. Gorbunov, C. Hofmann, S. Mnch, A. Lof-  
fler, M. Kamp, J. P. Reithmaier, V. D. Kulakovskii, and A. Forchel, "Lasing  
in high-Q quantum-dot micropillar cavities," *Appl. Phys. Lett.* **89**, 051107  
(2006).
- [54] A. M. Armani and K. J. Vahala, "Heavy water detection using ultra-high-  
Q microcavities," *Opt. Lett.* **31**, 1896 (2006).
- [55] A. Srinivasan, S. Murtaza, J. C. Campbell, and B. G. Streetman, "High

- quantum efficiency dual wavelength resonant-cavity photodetector," *Appl. Phys. Lett.* **66**, 535 (1995).
- [56] K. Djordjev, S. J. Choi, and P. D. Dapkus, "Microdisk tunable resonant filters and switches," *IEEE Phot. Technol. Lett.* **14**, 828-830 (2002).
- [57] C. K. Madsen, G. Lenz, A. J. Bruce, M. A. Capuzzo, L. T. Gomez, T. N. Nielsen, and I. Brener, "Multistage dispersion compensator using ring resonators," *Opt. Lett.* **24**, 1555-1557 (1999).
- [58] V. R. Almeida, C. A. Barrios, R. R. Panepucci, and M. Lipson, "All-optical control of light on a silicon chip," *Nature* **431**, 1081-1084 (2004).
- [59] E. Pawlowski, K. Takiguchi, M. Okuno, K. Sasayama, A. Himeno, K. Okamoto, and Y. Ohmori, "Variable bandwidth and tunable centre frequency filter using transversal-form programmable optical filter," *Electron. Lett.* **32**, 113-114 (1996).
- [60] D. W. Vernooy, V. S. Ilchenko, H. Mabuchi, E. W. Streed, and H. J. Kimble, "High-Q measurements of fused-silica microspheres in the near infrared," *Opt. Lett.* **23**, 247-249 (1998).
- [61] B. Gayral, J. M. Gerard, A. Lemaitre, C. Dupuis, L. Manin, and J. L. Pelouard, "High-Q wet-etched GaAs microdisks containing InAs quantum boxes," *Appl. Phys. Lett.* **75**, 1908-1910 (1999).
- [62] B. E. Little, J. Foresi, G. Steinmeyer, E. R. Thoen, S. T. Chu, H. Haus, E. Ippen, L. C. Kimberling, and W. Greene, "Ultra-compact Si-SiO<sub>2</sub> microring resonator optical channel dropping filters," *IEEE Phot. Technol. Lett.* **10**, 549-551 (1998).

- [63] G. Rempe, R. J. Thompson, H. J. Kimble, and R. Lalezari, "Measurement of ultralow losses in an optical interferometer," *Opt. Lett.* **17**, 363-365 (1992).
- [64] B. S. Song, S. Noda, T. Asano, and Y. Akahane, "Ultra-high-Q photonic double-heterostructure nanocavity," *Nature Materials* **4**, 207-210 (2005).
- [65] A. Yariv, "Critical coupling and its control in optical waveguide-ring resonator systems," *IEEE Phot. Technol. Lett.* **14**, 483-485 (2002).
- [66] J. Yao, D. Leuenberger, M. M. Lee, and M. C. Wu, "Silicon microtoroidal resonators with integrated MEMS tunable coupler," *IEEE J. Sel. Topics Quantum Electron.* **13**, 202-208 (2007).
- [67] M. A. Popovic, T. Barwicz, F. Gan, M. S. Dahlem, C. W. Holzwarth, P. T. Rakich, H. I. Smith, E. P. Ippen, and F. X. Kartner, "Transparent wavelength switching of resonator filters," *Conference on Lasers and Electro-Optics (CLEO), CPDA2* (2007).
- [68] L. Zhou and A. W. Poon, "Electrically reconfigurable silicon microring resonator-based filter with waveguide-coupled feedback," *Opt. Express* **15**, 9194 (2007).
- [69] G. Cocorullo, F. G. Della Corte, and I. Rendina, "Temperature dependence of the thermo-optic coefficient in crystalline silicon between room temperature and 550 K at the wavelength of 1523 nm," *Appl. Phys. Lett.* **74**, 3338-3340 (1999).
- [70] R. A. Soref and B.R. Bennett, "Kramers-Kronig analysis of the electrooptical switching in silicon," in *Proc. SPIE* **704**, 32-37, Cambridge, MA (1987).
- [71] R. A. Soref, "Electrooptical effects in silicon," *IEEE J. Quantum Electron.* **23**, 123-129, (1987).

- [72] P. R. N. Childs, "Practical temperature measurement," Butterworth-Heinemann (2001).
- [73] V. R. Almeida, R. R. Panepucci, and M. Lipson, "Nanotaper for compact mode conversion," *Opt. Lett.* **28**, 1302-1304 (2003).
- [74] W. Bogaerts, D. Taillaert, B. Luyssaert, P. Dumon, J. Van Campenhout, P. Bienstman, D. Van Thourhout, R. Baets, V. Wiaux, and S. Beckx, "Basic structures for photonic integrated circuits in Silicon-on-insulator," *Opt. Express* **12**, 1583-1591 (2004).
- [75] J. Niehusmann, A. Vorckel, P. H. Bolivar, T. Wahlbrink, W. Henschel, and H. Kurz, "Ultrahigh-quality-factor silicon-on-insulator microring resonator," *Opt. Lett.* **29**, 2861-2863 (2004).
- [76] F. Xia, L. Sekaric, and Y. A. Vlasov, "Mode conversion losses in silicon-on-insulator photonic wire based racetrack resonators," *Opt. Express* **14**, 3872-3886 (2006).
- [77] S. Donati, "Photodetectors: devices, circuits, and applications," Prentice Hall PTR (2000).
- [78] S. M. Sze, "Physics of Semiconductor Devices," Wiley-Interscience (1981).
- [79] T. P. Pearsall, "Photonics essentials: an introduction with experiments," McGraw-Hill Professional (2002).
- [80] P. J. Hambleton, S. A. Plimmer, and G. J. Rees, "Limitations of the saturated drift velocity approximation for time domain modelling," *Semiconductor Science and Technology* **17**, 124-128 (2002).
- [81] <http://www.ioffe.ru/SVA/NSM/Semicond/Ge/electric.html>.

- [82] L. Schares, C. L. Schow, S. J. Koester, G. Dehlinger, R. John, and F. E. Doany, "A 17-Gb/s low-power optical receiver using a Ge-on-SOI photodiode with a 0.13  $\mu\text{m}$  CMOS IC," Optical Fiber Communication Conference (OFC), 1-3 (2006).
- [83] G. Dehlinger, S. J. Koester, J. D. Schaub, J. O. Chu, Q. C. Ouyang, and A. Grill, "High-speed Germanium-on-SOI lateral PIN photodiodes," IEEE Photon. Technol. Lett. **16**, 2547-2549 (2004).
- [84] D. Ahn, C. Hong, J. Liu, W. Giziewicz, M. Beals, L. C. Kimerling, J. Michel, J. Chen, and F. X. Kartner, "High performance, waveguide integrated Ge photodetectors," Opt. Express **15**, 3916-3921 (2007).
- [85] R. Doering and Y. Nishi, "Handbook of semiconductor manufacturing technology," CRC Press (2007).
- [86] M. Henini and M. Razeghi, "Handbook of infrared detection technologies," Elsevier (2002).
- [87] H. Luan, D. R. Lim, K. K. Lee, K. M. Chen, J. G. Sandland, K. Wada, and L. C. Kimerling, "High-quality Ge epilayers on Si with low threading-dislocation densities," Appl. Phys. Lett. **75**, 2909-2911 (1999).
- [88] L. Colace, G. Masini A. Altieri, and G. Assanto, "Waveguide photodetectors for the near-infrared in polycrystalline germanium on silicon," IEEE Photon. Technol. Lett. **18**, 1094-1096 (2006).
- [89] S. Sedky, J. Schroeder, T. Sands, R. Howe, and T. King, "Pulsed laser annealing of silicon-germanium films," Materials Research Society Symposium Proceedings, J4.2 (2003).

- [90] S. S. Iyer and A. J. Auberton-Herve, "Silicon wafer bonding technology: for VLSI and MEMS applications," Institution of Electrical Engineers (2002).
- [91] Q. Tong, L. Huang, and U. Gosele, "Transfer of semiconductor and oxide films by wafer bonding and layer cutting," *J. of Electron. Materials* **29**, 928-932 (2000).
- [92] Y. Ishikawa , K. Wada , D. D. Cannon , J. F. Liu , H. C. Luan, and L. C. Kimerling, "Strain-induced band gap shrinkage in Ge grown on Si substrate," *Appl. Phys. Lett.* **82**, 2044-2046 (2003).
- [93] J. F. Liu , D. D. Cannon , K. Wada , Y. Ishikawa , S. Jongthammanurak , D. T. Danielson , J. Michel, and L. C. Kimerling, "Tensile strained Ge p-i-n photodetectors on Si platform for C and L band telecommunications," *Appl. Phys. Lett.* **87**, 011110-0111102 (2005).
- [94] M. Rouviere, M. Halbwx, J. Cercus, E. Cassan, L. Vivien, D. Pascal, M. Heitzmann, and J. Hartmann, "Integration of germanium waveguide photodetectors for intrachip optical interconnects," *Opt. Eng.* **44**, 075402-075406 (2005).
- [95] W. C. Dash and R. Newman, "Intrinsic optical absorption in single crystal germanium and silicon at 77 K and 300 K," *Phys. Rev.* **99**, 1151-1155 (1955).
- [96] J. F. Liu, D. D. Cannon, K. Wada, Y. Ishikawa, S. Jongthammanurak, D. T. Danielson, J. Michel, and L. C. Kimerling, "Silicidation-induced band gap shrinkage in Ge epitaxial films on Si," *Appl. Phys. Lett.* **84**, 660-662 (2004).
- [97] A. K. Okyay, A. M. Nayfeh, K. C. Saraswat, T. Yonehara, A. Marshall, and

- P. C. McIntyre, "High-efficiency metal-semiconductor-metal photodetectors on heteroepitaxially grown Ge on Si," *Opt. Lett.* **31**, 2565-2567 (2006).
- [98] E. D. Palik, "Handbook of Optical Constants of Solids," Academic Press (1985).
- [99] The Stopping and Range of Ions in Matter, developed by J. F. Ziegler, M. D. Ziegler, J. P. Biersack, available at <http://www.research.ibm.com/ionbeams/SRIM/SRIMLEGL.HTM>.
- [100] A. Dimoulas, P. Tsipas, and A. Sotiropoulos, and E. K. Evangelou, "Fermi-level pinning and charge neutrality level in germanium," *Appl. Phys. Lett.* **89**, 252110-252112 (2006).
- [101] K. Ang, S. Zhu, M. Yu, G. Lo, and D. Kwong, "High-performance waveguided ge-on-soi metal-semiconductor-metal photodetectors with novel silicon-carbon (Si:C) Schottky barrier enhancement layer," *IEEE Photon. Technol. Lett.* **20**, 754-756 (2008).
- [102] J. Oh, S. K. Baanerjee, and J. C. Campbell, "Metal-germanium-metal photodetectors on heteroepitaxial Ge-on-Si with amorphous Ge Schottky barrier enhancement layers," *IEEE Photon. Technol. Lett.* **16**, 581-583 (2004).
- [103] M. Levinshtein, and G. S. Simin, "Getting to Know Semiconductors," World Scientific (1992).
- [104] L. Tang, S. E. Kocabas, S. Latif, A. K. Okyay, D. Ly-Gagnon, K. C. Saraswat, and D. A. B. Miller, "Nanometre-scale germanium photodetector enhanced by a near-infrared dipole antenna," *Nature Photonics* **2**, 226-229 (2008).

- [105] S. Y. Chou, W. Khalil, T. Y. Hsiang, and S. Alexandrou, "Ultrafast nanoscale metal-semiconductor-metal photodetectors on bulk and low-temperature grown GaAs," *Appl. Phys. Lett.* **61**, 819-821 (1992).
- [106] C. R. Doerr and K. Okamoto, "Advances in Silica Planar Lightwave Circuits," *J. Lightwave Technol.* **24**, 4763-4789 (2006).
- [107] K. Okamoto, K. Takiguchi, and Y. Ohmori, "16-channel optical add/drop multiplexer using silica-based arrayed-waveguide gratings," *Electron. Lett.* **31**, 723-724 (1995).
- [108] J. Minowa and Y. Fujii, "Dielectric multilayer thin-film filters for WDM transmission systems," *J. Lightwave Technol.* **1**, 116-121 (1983).
- [109] C. R. Giles, "Lightwave applications of fiber Bragg gratings," *J. Lightwave Technol.* **15**, 1391-1404 (1997).
- [110] B. E. Little, S. T. Chu, W. Pan, and Y. Kokubun, "Microring resonator arrays for VLSI photonics," *IEEE Photon. Technol. Lett.* **12**, 323-325 (2000).
- [111] Q. Xu, B. Schmidt, J. Shakya, and M. Lipson, "Cascaded silicon micro-ring modulators for WDM optical interconnection," *Opt. Express* **14**, 9430-9435 (2006).
- [112] S. Xiao, M. H. Khan, H. Shen, and M. Qi, "A highly compact third-order silicon microring add-drop filter with a very large free spectral range, a flat passband and a low delay dispersion," *Opt. Express* **15**, 14765-14771 (2007).
- [113] G. Griffel, "Vernier effect in asymmetrical ring resonator arrays," *IEEE Photon. Technol. Lett.* **12**, 1642-1644 (2000).